# Scaling Methods for the Production of Tungsten Fiber-Reinforced Composites via Chemical Vapor Deposition

Alexander Lau

Energie & Umwelt / Energy & Environment
Band / Volume 675
ISBN 978-3-95806-851-3

Mitglied der Helmholtz-Gemeinschaft

JÜLICH
Forschungszentrum

Schriften des Forschungszentrums Jülich
Reihe Energie & Umwelt / Energy & Environment Band / Volume 675

Forschungszentrum Jülich GmbH
Institute of Fusion Energy and Nuclear Waste Management (IFN)
Plasma Physics (IFN-1)

# Scaling Methods for the Production of Tungsten Fiber-Reinforced Composites via Chemical Vapor Deposition

Alexander Lau

Schriften des Forschungszentrums Jülich
Reihe Energie & Umwelt / Energy & Environment Band / Volume 675

ISSN 1866-1793 ISBN 978-3-95806-851-3

Bibliografische Information der Deutschen Nationalbibliothek.
Die Deutsche Nationalbibliothek verzeichnet diese Publikation in der
Deutschen Nationalbibliografie; detaillierte Bibliografische Daten
sind im Internet über http://dnb.d-nb.de abrufbar.

| | |
|---|---|
| Herausgeber und Vertrieb: | Forschungszentrum Jülich GmbH<br>Zentralbibliothek, Verlag<br>52425 Jülich<br>Tel.: +49 2461 61-5368<br>Fax: +49 2461 61-6103<br>zb-publikation@fz-juelich.de<br>www.fz-juelich.de/zb |
| Umschlaggestaltung: | Grafische Medien, Forschungszentrum Jülich GmbH |
| Druck: | Grafische Medien, Forschungszentrum Jülich GmbH |
| Copyright: | Forschungszentrum Jülich 2025 |

Schriften des Forschungszentrums Jülich
Reihe Energie & Umwelt / Energy & Environment, Band / Volume 675

D 82 (Diss. RWTH Aachen University, 2025)

ISSN 1866-1793
ISBN 978-3-95806-851-3

Vollständig frei verfügbar über das Publikationsportal des Forschungszentrums Jülich (JuSER)
unter www.fz-juelich.de/zb/openaccess.

# List of Publications

## As Corresponding Author

[1] **A. Lau** et al. “Bulk Tungsten Fiber-Reinforced Tungsten ($W_f$/W) Composites Using Yarn-Based Textile Preforms”. In Journal of Nuclear Engineering 2023 Vol. 4 Issue 2 Pages 375-390, https://doi.org/10.3390/jne4020027

[2] **A. Lau** et al. ”Combining Chemical Vapor Deposition and Spark Plasma Sintering for the Production of Tungsten Fiber-Reinforced Tungsten (Hybrid – $W_f$/W)”. In Advanced Engineering Materials (2024), https://doi.org/10.1002/adem.202301929

## As Co-author

[3] J. W. Coenen, P. Huber, **A. Lau**, L. Raumann, D. Schwalenberg, Y. Mao, et al.
”Tungsten Fiber-Reinforced tungsten ($W_f$/W) using yarn-based textile preforms”. In Physica Scripta 2021 Vol. 96 Issue 12, https://doi.org/10.1088/1402-4896/ac37cf

[4] D. Schwalenberg, J. W. Coenen, J. Riesch, T. Hoeschen, Y. Mao, **A. Lau**, et al.
”Large-Scale Tungsten Fibre-Reinforced Tungsten and Its Mechanical Properties”. In Journal of Nuclear Engineering 2022 Vol. 3 Issue 4 Pages 306-320, https://doi.org/10.3390/jne3040018

[5] J. Riesch, A. von Müller, Y. Mao, J.W. Coenen, B. Böswirth, S. Elgeti, M. Fuhr, H. Greuner, T. Höschen, K. Hunger, P. Junghanns, **A. Lau**, S. Roccella, L. Vanlitsenburgh, J.-H. You, Ch. Linsmeier, R. Neu.
“Progress in the development of industrial scale tungsten fibre-reinforced composite materials”, In Nuclear Materials and Energy 2024 Vol. 38, https://doi.org/10.1016/j.nme.2024.101591

[6] R. Shu, Y. R. Mao, **A. Lau**, J. W. Coenen, A. Terra, C. Liu, et al.
”Effect of the heating rate and Y2O3 coating on the microstructure of Wf/ Y2O3/W composites via field assisted sintering technology”. In Nuclear Materials and Energy 2024 Vol. 38, https://doi.org/10.1016/j.nme.2024.101602

## In Preparation

[7] **A. Lau** et al. “Exceptionally pseudo-ductile tungsten-fiber-reinforced tungsten manufactured via chemical vapor infiltration”

# Abstract

The transition toward a sustainable and resource-efficient energy ecosystem has revealed the limitations of existing materials. Emerging technologies, including concentrated solar power (CSP) systems and nuclear fusion reactors, call for significant advancements in material science to achieve mechanical stability, thermal resistance, and even radiation tolerance at exceptional levels. This necessity becomes particularly apparent under the extreme conditions encountered by plasma-facing components (PFCs) in nuclear fusion devices.

Tungsten fiber-reinforced composites (WFRCs), such as tungsten fiber-reinforced tungsten ($W_f$/W), have emerged as promising candidates to meet these stringent requirements and could play a key role in the future advancement of these cutting-edge technologies.

This dissertation addresses the persistent challenges of scaling the production of these composite materials from laboratory research to industrial applications. The primary objective is to transform the chemical vapor deposition (CVD) technique, which is traditionally used for thin-film systems in the semiconductor industry, into a scalable process for WFRC production.

To achieve this goal, this thesis primarily focuses on the further development of the existing WILMA chemical processing facility at Forschungszentrum Jülich in Germany. The findings are detailed in two previously published articles, which constitute integral parts of this thesis, and are further supplemented by content intended for a forthcoming third publication.

The first publication [1] addresses the brittle fracture behavior of pure tungsten at room temperature and aims to ensure consistent material properties of $W_f$/W composites. For the first time, the fatigue behavior of such composite materials under cyclic mechanical loading conditions was successfully extrapolated, thereby establishing a new reproducibility benchmark and demonstrating that these composites are capable of meeting the strict quality standards of industrial applications.

The second publication [2] examines the combination of established consolidation methods and introduces a novel approach to enhance the resilience of critical ceramic interfaces and tungsten fibers in the context of elevated stresses typically faced during sintering processes. The proposed strategy provides new perspectives for the integration of tungsten fibers into a range of matrix materials, thereby potentially broadening the prospective scope of applications for WFRCs.

The forthcoming third publication focuses on the chemical vapor infiltration (CVI) technique for the production of $W_f$/W composites. Extensive modifications to the WILMA chemical processing facility enabled the first successful implementation of CVI at a process-relevant scale, resulting in reduced production time and costs, enhanced material design flexibility, and expanded opportunities for joining tungsten with other materials.

The initial prototype sample demonstrated substantial advancements in fiber volume fraction and fracture energy, achieving values that exceeded those of currently used materials by more than two orders of magnitude. Building on these promising results, an optimized design was developed to further increase the production capacity and permit recycling. The advanced setup has already been successfully implemented and is scheduled for comprehensive testing in the near future.

In conclusion, this work lays a robust foundation for the potential commercialization of WFRCs while underscoring the necessity for further material characterization and process optimization.

# Zusammenfassung

Die Transformation zu einer nachhaltigen und ressourceneffizienten Energieversorgung hat die Grenzen bestehender Materialien aufgezeigt. Zukunftsweisende Technologien wie konzentrierte Solarkraftwerke oder Kernfusionsreaktoren erfordern innovative Werkstoffe, die mechanische Stabilität, thermische Beständigkeit und sogar Strahlungstoleranz auf hohem Niveau vereinen. Dies wird besonders anhand der extremen Belastungen plasmaexponierter Komponenten (PFCs) in Kernfusionsreaktoren ersichtlich.

Wolframfaserverstärkte Verbundwerkstoffe (WFRCs), insbesondere wolframfaserverstärktes Wolfram ($W_f$/W), haben sich als vielversprechende Kandidaten zur Erfüllung dieser Anforderungen etabliert und könnten eine Schlüsselrolle in der Weiterentwicklung dieser Technologien spielen. Die vorliegende Dissertation adressiert bislang ungelöste Herausforderungen bei der Skalierung dieser Werkstoffe vom Labor- in den industriellen Maßstab. Das primäre Ziel besteht darin, die chemische Gasphasenabscheidung (CVD), die üblicherweise für die Applikation von Dünnschichtsystemen in der Halbleiterindustrie eingesetzt wird, in ein skalierbares Verfahren für die WFRC-Produktion umzuwandeln.

Um dieses Ziel zu erreichen, wurde im Rahmen dieser Arbeit die bestehende Prozessanlage WILMA am Forschungszentrum Jülich weiterentwickelt. Die Resultate sind bereits in zwei veröffentlichten Artikeln beschrieben, die einen integralen Bestandteil dieser Dissertation ausmachen. Darüber hinaus werden Inhalte präsentiert, die für eine geplante dritte Veröffentlichung vorgesehen sind.

Die erste Publikation [1] befasst sich mit dem Sprödbruchverhalten von $W_f$/W-Verbundwerkstoffen bei Raumtemperatur. Erstmals konnte das Ermüdungsverhalten solcher Werkstoffe unter zyklischer mechanischer Belastung extrapoliert werden, wodurch ein neuer Reproduzierbarkeitsmaßstab gesetzt wurde. Die Ergebnisse belegen, dass diese Verbundwerkstoffe grundsätzlich die strengen Qualitätsstandards industrieller Anwendungen erfüllen können.

Die zweite Publikation [2] untersucht die Kombination etablierter Konsolidierungsmethoden und beschreibt einen neuen Ansatz zur Erhöhung der Stabilität kritischer keramischer Grenzflächen sowie der Wolframfasern im Verbunddesign. Die vorgestellte Strategie eröffnet neue Perspektiven für die Integration von Wolframfasern in verschiedene Matrixmaterialien und erweitert damit den potenziellen Anwendungsbereich von WFRCs.

Die bevorstehende dritte Veröffentlichung thematisiert die chemische Gasphaseninfiltration (CVI) zur Fertigung von $W_f$/W-Verbundwerkstoffen. Durch umfangreiche Modifikationen der WILMA-Prozessanlage konnte das CVI-Verfahren erstmals erfolgreich im prozessrelevanten Maßstab umgesetzt werden. Dies führte zu einer signifikanten Reduktion der Produktionszeiten und -kosten, einer erhöhten Flexibilität im Verbunddesign sowie einer potenziellen Lösung der Fügeproblematik von Wolfram mit anderen Werkstoffen. Der erste Prototyp zeigte bereits signifikante Steigerungen des erreichbaren Faservolumenanteils und der Bruchenergie, die mehr als zwei Größenordnungen über den Werten der derzeit verwendeten Materialien liegen. Basierend auf diesen Ergebnissen wurde ein optimiertes Design entwickelt, das sowohl die Produktionskapazität steigern als auch Recyclingstrategien integrieren soll. Die optimierte Konfiguration wurde bereits in die Prozessanlage WILMA implementiert und wird in naher Zukunft getestet. Zusammenfassend bildet diese Arbeit eine solide Grundlage für eine potenzielle Kommerzialisierung von WFRCs und unterstreicht zugleich die Notwendigkeit zusätzlicher Materialcharakterisierung und Prozessoptimierung.

# Table of Content

# 1 Introduction

Materials science has always been a fundamental driver of technological and socio-economic progress [8]. Entire historical eras, such as the Stone, Bronze, and Iron Ages, were defined by the dominant materials that catalysed transformative technological advancements [8-11]. In modern times, materials science remains indispensable across a broad range of industries, including aerospace [12], electronics [13], solar energy [14, 15], medicine [16, 17], and nuclear applications [18-21].

One of the most challenging frontiers in materials innovation is nuclear fusion, which has the potential to be a primary energy source capable of radically transforming the global energy landscape [22]. Once successfully commercialized, nuclear fusion could offer numerous advantages over nuclear fission, including an abundant fuel supply, an exceptionally high energy output with minimal fuel requirements, significantly reduced radioactive waste disposal times, and the complete elimination of the risk of nuclear meltdowns [23, 24].

Despite these benefits, the path to commercializing nuclear fusion extends well beyond improving reactor designs [25, 26]. A critical bottleneck is the requirement for advanced materials that can endure the extreme operational conditions within a nuclear fusion reactor, which is characterized by high heat fluxes, intense radiation, and substantial mechanical stress [27]. These harsh environments necessitate materials that not only withstand these conditions but also maintain their reliability and integrity over extended periods of operation [28, 29].

However, even the most advanced materials can only realize their full potential when they are successfully transferred from laboratory prototypes to industrial-scale production. It is not sufficient to merely increase production volumes; ensuring uniform material properties across larger scales is crucial to guarantee the performance and reliability of real-world applications [14, 30, 31]. Economic considerations are equally significant, as processes that are efficient on a small scale may become prohibitively expensive and complex when scaled up [14]. This underscores the necessity for advanced process control and optimization strategies to achieve both technical feasibility and economic sustainability [8, 32].

A pertinent example of these scaling challenges is provided by tungsten fiber-reinforced composites (WFRCs). At the laboratory scale, WFRCs have demonstrated significant potential for applications in high-temperature and nuclear environments, particularly in extending the operational lifetime of critical components in nuclear fusion reactors [33-37]. However, scaling up the production of these materials to meet industrial demands continues to pose substantial technical and economic challenges, especially in ensuring reproducibility and increasing production throughput [38-40].

This work addresses these challenges by enhancing the scalability of the chemical vapor deposition (CVD) technique, one of the two available consolidation methods for these materials. The main objective is to optimize the existing manufacturing processes for WFRCs, with a particular focus on tungsten fiber-reinforced tungsten ($W_f$/W) composites. This thesis aims to enhance the reproducibility, material performance, and production throughput of WFRCs, while simultaneously reducing manufacturing complexity and costs. To accomplish these objectives, a range of methodologies will be subjected to rigorous examination, with the associated results presented and subjected to critical analysis in the context of broader industrial applications. Furthermore, the essential factors for the successful commercialization of WFRCs will be outlined.

# 2 Theoretical Background

This chapter provides a comprehensive framework for understanding the material requirements of advanced technologies, with a particular focus on the extreme conditions encountered in nuclear fusion reactors. It critically examines the limitations of the materials currently in use and explores potential alternatives that promise enhanced performance but require specialized raw materials and sophisticated processing techniques. In this context, the chapter highlights the potential relevance of WFRCs as a promising solution to these challenges, thereby establishing a foundation for a more thorough examination of their manufacturing processes in the subsequent chapter.

## 2.1 Nuclear Fusion

### 2.1.1 Fundamentals

Nuclear fusion is a process whereby light atomic nuclei merge to form a heavier nucleus. In this reaction, the total mass of the resulting elements is slightly less than the combined mass of the original nuclei. The mass difference is converted into energy, as postulated by Einstein's famous equation $E = mc^2$ [41]. The energy released manifests as either kinetic energy or electromagnetic radiation, such as γ-radiation [22, 42, 43].

To harness this energy for potential commercial applications, most strategies aim to utilize a mixture of two heavy hydrogen isotopes, deuterium (D) and tritium (T). These isotopes fuse to form a stable helium-4 (He-4) nucleus and a high-energy neutron [22, 42, 43], as shown in the reaction below:

$$\boldsymbol{D + T \rightarrow {}^{4}_{2}He\ (3.517\ MeV) + {}^{1}n\ (14.069\ MeV)} \qquad (1)$$

D-T fusion provides a relatively high energy yield and requires lower initiation temperatures compared to other fusion fuels [44-46]. However, achieving controlled D-T fusion still requires extremely high temperatures, above $10^8$ – $10^9$ Kelvin, to provide sufficient kinetic energy for the nuclei to overcome their electrostatic repulsion, known as the Coulomb barrier [43].

A major challenge for the utilization of D-T fusion is the abundance of natural tritium resources [47]. The fuel must therefore be produced in the reactor itself using so-called breeding blankets, primarily by utilizing the reaction between lithium-6 and the neutrons released during the D-T fusion [43]:

$$\boldsymbol{{}^{6}_{3}Li + {}^{1}n \rightarrow {}^{4}_{2}He + {}^{3}_{1}H + 4.8\ MeV} \qquad (2)$$

The in-situ production of tritium is of great importance for ensuring the sustainability and operational efficiency of nuclear fusion reactors that aim to utilize D-T fusion [48].

In order to maintain a self-sufficient fuel cycle, the incorporation of supplementary components such as neutron multipliers, including lead or beryllium, is essential to compensate for neutron losses that occur, for instance, through the absorption of the reactor walls. Further insights into this critical topic are provided in references [49-53]. Based on these considerations, the following section provides a brief introduction to the two primary reactor concepts that employ magnetic confinement principles.

### 2.1.2 Reactor Concepts via Magnetic Confinement

The majority of nuclear fusion reactor designs rely on the magnetic confinement of a plasma to sustain the extreme conditions required for fusion reactions. The application of powerful magnetic fields serves to prevent direct contact between the hot plasma and the reactor walls, thereby minimizing energy losses and protecting the reactor structure from damage [54]. During the fusion process, high-energy neutrons are produced. As electrically neutral particles, these neutrons are unaffected by magnetic fields, allowing them to transfer their kinetic energy directly to the reactor walls. The absorbed heat is then extracted by a coolant and can be harnessed directly or converted to electricity through turbines and generators [22, 42, 48].

The most prominent technologies in this domain are tokamaks and stellarators, both of which are designed to enhance plasma confinement and stability [55, 56]. Figure 1 provides a schematic comparison of these diverse confinement systems [57].

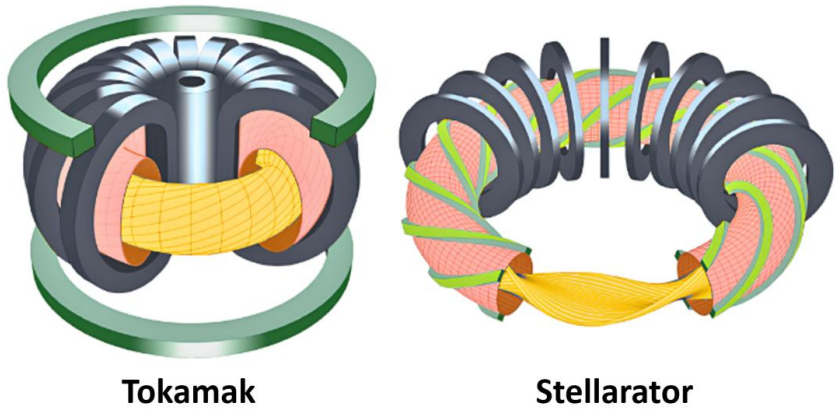


*Figure 1: Comparison of tokamak and stellarator plasma confinement systems, adapted from [57].*

Tokamaks employ a combination of toroidal and poloidal magnetic fields to create a doughnut-shaped plasma confinement. This configuration represents the most extensively researched and developed approach to fusion energy, supported by a substantial body of research and operational experience [55, 56, 58-61].

In contrast, stellarators use a more complex arrangement of twisted magnetic field coils. This design allows for plasma confinement without relying on strong induced currents, potentially offering greater inherent stability and the capability for continuous, disruption-free operation. Despite the promising advantages of stellarators in terms of stability and operational continuity, they are significantly more difficult to design and construct compared to tokamaks [55, 56, 62, 63].

Achieving a net positive energy output from nuclear fusion requires maintaining optimal conditions, including extremely high temperatures and effective plasma confinement. However, plasma instabilities still represent a significant challenge for both confinement systems [64-66]. Managing these fluctuations is fundamental to ensuring the sustained and reliable operation of fusion reactors [58, 59, 61, 62, 66]. Although plasma stability represents a critical obstacle, it is not the sole impediment to the commercialization of fusion energy. Material-related challenges are equally significant and will be examined in greater detail in the next section.

### 2.1.3 Challenges for Fusion Reactor Material Designs

The operational lifetime of a nuclear fusion device is fundamentally dictated by the resilience and performance of its materials, which must withstand the extreme conditions in the reactor over prolonged periods [67]. The development of materials that can reliably meet these rigorous demands represents a critical and ongoing challenge in advancing fusion technology [68-72].

One of the most significant concerns is the damage caused by **neutron irradiation**. During reactor operation, materials are continuously bombarded by high-energy neutrons, which displace atoms from their lattice positions and induce gradual structural degradation. This degradation occurs through complex processes, such as material migration, swelling, phase changes, mixing, and embrittlement, all of which can severely affect the properties and performance of plasma-facing components (PFCs). As material performance degrades, maintaining reactor operation becomes increasingly challenging, necessitating frequent repairs or replacement of vital components. This, in turn, raises maintenance costs and could result in significant reactor downtime [72-75].

The interaction of PFCs with **hydrogen**, particularly with isotopes such as **tritium**, represents an additional obstacle. The absorption of hydrogen into reactor materials can result in embrittlement, thereby compromising the structural integrity of critical components. This issue is of particular concern in the context of reactors that are designed to operate on a self-sustaining tritium fuel cycle. In order to guarantee the performance and safety of nuclear fusion reactors over extended periods, it is essential to possess a comprehensive understanding of the behavior of PFCs in the presence of hydrogen and its isotopes, coupled with an implementation of effective monitoring strategies [21, 59, 72, 76].

The durability of PFCs is further challenged by various **erosion** mechanisms. Radiation-enhanced sublimation, photon-induced desorption, and physical sputtering collectively contribute to the slow erosion of material surfaces exposed to intense radiation. Furthermore, chemical erosion occurs when reactive plasma species interact with the reactor walls, forming volatile compounds that can compromise the structural integrity of materials. Together, these effects result in material thinning, reduced performance, and the necessity for regular maintenance, with the service intervals being largely dependent on the specific materials used [61, 77, 78].

**Thermal stress** represents another critical factor contributing to material degradation. Continuous exposure to extreme heat fluxes and rapid temperature fluctuations, especially in pulsed devices like tokamaks, can lead in thermal fatigue. Repeated cycles of thermal stress over time can initiate and propagate cracks, thereby compromising the structural integrity and durability of critical reactor components [79-82].

**Localized overheating**, potentially induced by plasma instabilities, has the potential to result in the melting or spattering of materials. This phenomenon introduces impurities into the plasma, which may severely degrade the fusion power output. Should the performance fall below the critical threshold required to sustain plasma conditions, the reactor may fail to achieve a net energy gain, ultimately jeopardizing its operational efficiency [18, 27, 29, 66, 73, 74, 82, 83].

Addressing all these multifaceted challenges is paramount for the development of robust fusion reactors capable of sustained, long-term operation. The next subchapter examines the current component designs and material choices aimed at maximizing reactor longevity and ensuring reliable performance under the extreme conditions in such devices.

### 2.1.4 Thermal Management and Protection Systems in Fusion Reactors

A critical component engineered to withstand the extreme operational conditions of a magnetic confinement fusion device is the divertor [29]. This component plays a key role in shielding other vital reactor structures from the intense heat and particle fluxes generated by the plasma [60, 83-86].

ITER, one of the most ambitious nuclear fusion projects currently under construction in France, incorporates an advanced monoblock design for its divertor, as depicted in Figure 2.

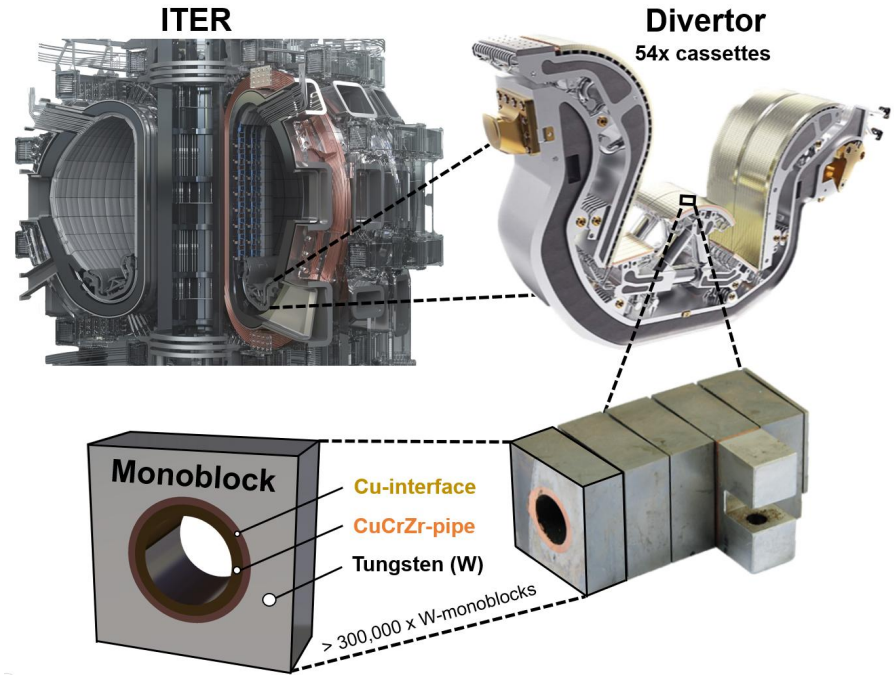


*Figure 2: Monoblock design of the ITER divertor, illustrating the ITER structure, one of the 54 divertor cassettes, and one of the over 300,000 tungsten (W) monoblocks [87]. Each monoblock has a W shield surrounding a CuCrZr cooling pipe with a copper (Cu) interface. Adapted from [88] and [89].*

The 54 divertor cassettes in ITER feature a CuCrZr cooling structure connected to approximately 300,000 tungsten (W) monoblocks through a copper (Cu) interface [87]. This design enhances the structural bond between the W armor and CuCrZr pipe, ensuring durability, effective heat management, and preventing armor detachment. Small gaps between the W-monoblocks are carefully engineered to alleviate thermal stresses induced by temperature fluctuations, thus maintaining the structural integrity and thermal performance of the system [85].

Engineered to withstand extreme heat loads exceeding 20 $MW/m^2$ [90], the divertor utilizes pressurized water as a coolant, circulating through internal channels within the CuCrZr structure to ensure an efficient heat transfer [91-93]. For future reactors like DEMO or commercial fusion power plants (FPPs) [94-97], alternative coolants such as helium or liquid metals are still under consideration [98-100]. However, the adoption of alternative coolants would necessitate a comprehensive redesign of the existing divertor configuration [101-103]. In general, significant material limitations are currently the main constraint for any progress in component design.

Even existing configurations, such as the monoblock design illustrated in Figure 2, were already developed as a compromise solution to address the significant differences in coefficients of thermal expansion (CTE) and the associated bonding challenges between W and CuCrZr alloys [104, 105]. Nevertheless, ongoing research efforts seek to identify more effective solutions. For instance, the adoption of advanced materials or innovative joining techniques, as proposed by Müller et al. [106, 107] and Neu et al. in reference [108], could facilitate the development of entirely novel divertor designs with increased efficiency and reduced manufacturing complexity. To gain a deeper understanding of these and related optimization potentials, the following section provides a more detailed analysis of the challenges and solutions associated with current material options, with a particular focus on W as the primary armor material.

## 2.2 Tungsten (W) in Nuclear Fusion: Challenges and Emerging Solutions

Among all elements in the periodic table, W is generally considered a prime candidate for nuclear reactor designs, specifically as a PFC in nuclear fusion reactors [109, 110]. W possesses several critical qualities, including the highest melting point of any metal (3,422°C), excellent thermal conductivity (~170 W/mK at 20°C), outstanding resistance to sputtering, minimal reactivity with hydrogen, and a moderate formation of radioactive isotopes [111-113]. These attributes render W indispensable for enduring the extreme conditions in nuclear fusion environments.

Despite its impressive properties, pure W has notable limitations. Particularly in commercial fusion applications, where operational durations and stress levels are anticipated to surpass even those in ITER, the limitations of this material become increasingly apparent [114-116]. Figure 3 (a) provides an overview of the key performance factors, comparing the properties of pure W with ideal target specifications, with insights based on [111-113], and references therein. This comparison demonstrates that pure W alone is not sufficient to meet the stringent requirements of a potential nuclear fusion industry. Consequently, material optimization strategies are essential to enhance its performance for these applications. Figure 3 (b) outlines the most prominent optimization strategies, along with the anticipated outcomes based on successful implementation and upscaling [111-113].

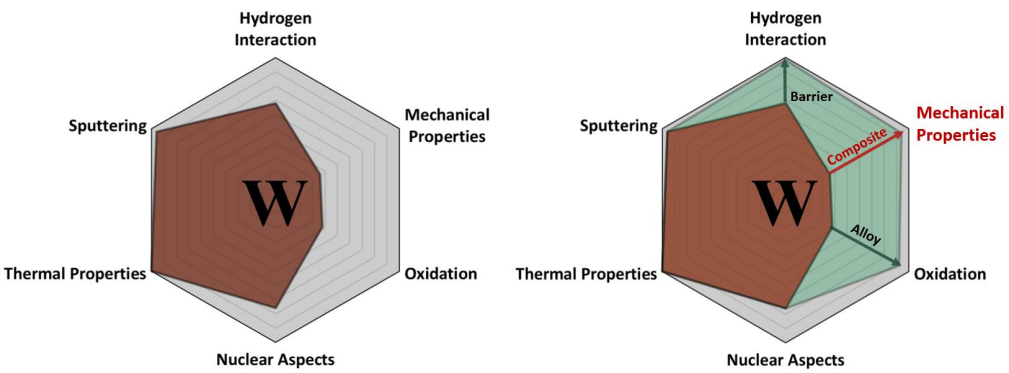


*Figure 3: Radar charts comparing nuclear fusion reactor requirements with pure W (a) and optimization approaches (b), highlighting mechanical properties and composite solutions in red as the main challenge of this study. Chart is based on [111-113], and references therein.*

The following subsections provide a more detailed examination of the primary material challenges and optimization strategies outlined in Figure 3, with a particular focus on tungsten's oxidation resistance, interactions with hydrogen isotopes, and mechanical limitations. Special emphasis is placed on its mechanical limitations, as these are considered crucial for the long-term stability of PFCs in fusion environments, as further discussed in references [34, 117, 118].

### 2.2.1 Oxidation resistance and SMART alloys

A major objective in optimizing W-based materials is to enhance their oxidation resistance, particularly at temperatures exceeding 500°C in the absence of an inert atmosphere [74, 119]. Under such conditions, tungsten oxides, predominantly tungsten trioxide ($WO_3$), are formed. At temperatures exceeding 800°C, $WO_3$ can partially sublimate in a vacuum, releasing volatile and potentially radioactive compounds that present significant safety concerns, as evidenced in references [120, 121]. The employment of "Self-passivating Metal Alloys with Reduced Thermo-oxidation" (SMART alloys), has demonstrated significant promise in mitigating these risks [122-124]. These alloys incorporate elements such as chromium and yttrium, which allow for the formation of protective oxide layers that prevent further oxidation of the W-surface [18, 74, 119]. More comprehensive insights into these advancements can be found in references [125-128].

### 2.2.2 Hydrogen Interaction and Tritium Permeation Barriers

A further significant challenge for W-based armor materials is their interaction with hydrogen isotopes, particularly tritium. The ability of W to retain and permeate tritium raises substantial safety and operational concerns, as outlined by Engels et al. in reference [129]. It is of paramount importance to address these hazards in order to guarantee the safe and reliable operation of commercial fusion reactors [130, 131]. One of the most effective strategies for mitigating these risks is the implementation of tritium permeation barriers (TPBs). These barriers are specifically engineered to limit the diffusion and accumulation of tritium in key reactor components, such as the first wall and breeding blankets [132]. The primary function of TPBs is to allow for the regulation of tritium permeation, thereby reducing the risks of environmental contamination and operational hazards [133, 134]. The efficacy of TPBs in enhancing reactor safety has been well documented in numerous studies [135-137], underscoring their indispensable role for fusion technology. Further insights into TPBs and their applications are provided in references [138-140].

### 2.2.3 Mechanical Constraints: Structural Strategies and Persistent Challenges

A key remaining challenge with W is its tendency to fracture in a brittle manner below the ductile-brittle transition temperature (DBTT). At this threshold, the material loses its ability to absorb further deformation energy, leading to rapid crack propagation and abrupt failure upon initial fracture [141]. This risk is particularly high in nuclear fusion environments, where neutron and hydrogen interactions can both increase DBTT, as previously discussed in chapter 2.1.3. Such behavior represents a significant concern for the structural integrity of W-based components, such as the monoblocks in the ITER divertor region. Figure 4 illustrates the considerable operational disparity between W and CuCrZr in a nuclear fusion reactor and underscores the inherent brittleness of W by demonstrating the risk of coolant leakage from the system [40, 113, 142].

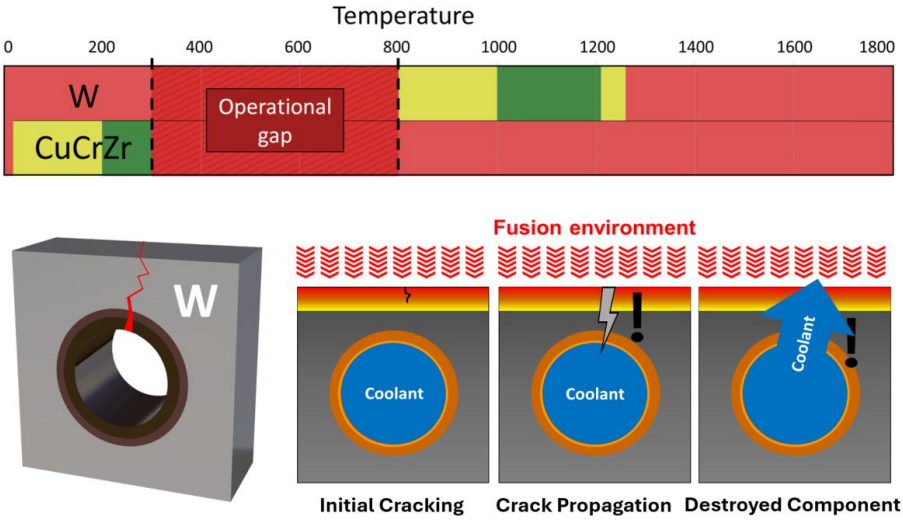


*Figure 4: Operational windows of W and CuCrZr and schematic representation of a worst-case scenario of crack propagation through the W-monoblocks, based on [40, 113, 142].*

Current engineering approaches to address these challenges focus on reducing stresses within the monoblocks by optimizing their size, geometry, and arrangement [69, 85, 143, 144]. While these measures effectively lower stress levels and delay crack formation, they significantly complicate the manufacturing process and thus increase production costs. For instance, the production and assembly of several hundred thousand monoblocks is expected to be economically unfeasible for commercial nuclear fusion reactors, as evidenced by references [90, 145-148]. Moreover, even with these measures, the intrinsic risk of brittle fracture still remains, as demonstrated by Pintsuk et al. [149] and Hirai et al. in reference [150]. To meet the demands of commercial applications, it is necessary to develop materials that not only possess improved mechanical properties but also allow for simplified component fabrication, as further discussed in references [26, 29, 33, 35, 151-153].

The primary objective is to extend the operational temperature range of W by reducing its DBTT, ideally to or below ambient temperature, which would substantially enhance its expected performance and application potential. In parallel, it is crucial to stabilize the microstructure of W under irradiation to prevent recrystallization and ensure long-term performance. Despite extensive research efforts, a definitive solution to this challenge has yet to be identified, as outlined in references [154, 155].

Alloying W with elements such as rhenium has demonstrated significant improvements in both ductility and resistance to recrystallization [154, 156, 157]. However, the activation of rhenium under neutron irradiation, coupled with its scarcity and high cost, renders it unsuitable for large-scale and particularly nuclear environments [156-160]. Attempts to substitute rhenium with alternative elements, including tantalum, titanium or vanadium, have not yielded comparable outcomes thus far, as noted in references [161-164].

Thermomechanical processing techniques, including rolling and forging with the addition of alloying elements [165-167], have shown the potential to reduce the DBTT of W even to ambient temperatures by creating ultrafine-grained microstructures through severe plastic deformation [168, 169]. However, these approaches have demonstrated limited efficiency when such materials are subjected to high-temperature annealing or irradiation, as reported in references [154, 170, 171].

Given the inherent limitations of intrinsic microstructural modifications or alloying of bulk W, the development of advanced composite solutions has emerged as a central area of research, which will be further elaborated in the following chapter.

## 2.3 Advanced Composite Solutions for Tungsten

Various composite solutions for W have been investigated, incorporating different reinforcing agents such as oxide-dispersion-strengthened (ODS) particles [172-175], foils / laminates [170, 176-180] and fibers [181-183]. To evaluate the effectiveness of these reinforcements under neutron-irradiated conditions, this work refers to the study of Terentyev et al. [184], which compares the effects of W particles, foils, and fibers as reinforcements in CuCrZr alloys under both irradiated and non-irradiated conditions at varying temperatures. Although this research is primarily concerned with CuCrZr matrices, the evaluated reinforcing agents are also applicable to W, thus providing a valuable foundation for preliminary investigations into W-based composite materials.

Figure 5 presents the corresponding stress-strain curves from mechanical fracture tests, adapted from reference [184]. The violet and green curves represent alloys that, as previously discussed, will not be further considered in this study.

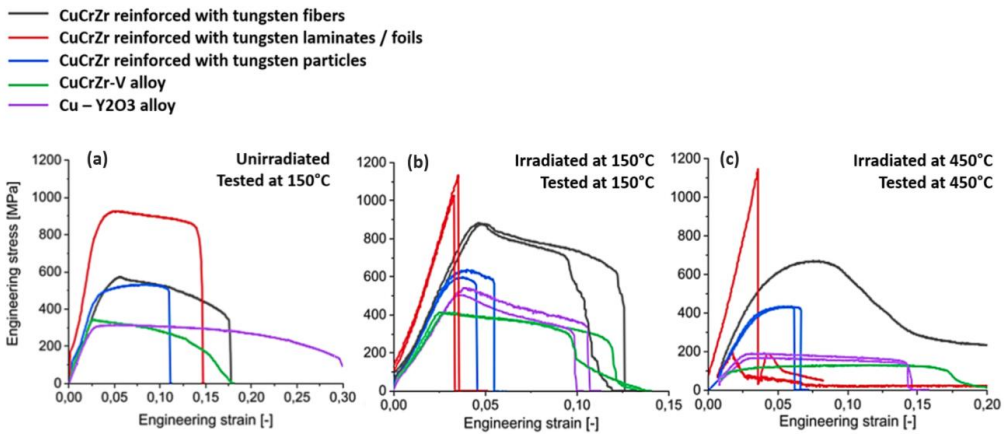


*Figure 5: Engineering stress-strain curves for advanced CuCrZr alloys and reinforced CuCrZr under three different conditions: (a) in the non-irradiated state, tested at 150°C; (b) irradiated and tested at 150°C; and (c) irradiated and tested at 450°C. Data adapted from [184].*

The results presented in panel (a) demonstrate that, among the various curves, W-foil reinforced CuCrZr (red) exhibits the highest fracture energy under non-irradiated conditions, as indicated by the largest area beneath the curve [185]. This superior performance demonstrates the material's capacity to absorb deformation energy prior to fracture, thereby underscoring its enhanced toughness and resilience [186]. However, when subjected to irradiation and elevated temperatures, a significant decline in performance is observed. This is evidenced by the sharp decline in the red curves following the peak stress in panels (b) and (c). This decline suggests that radiation exposure leads to a substantial loss of ductility in W-foil reinforced CuCrZr alloys, promoting a transition toward brittle fracture behavior. These findings are consistent with those reported by Garrison et al. in reference [187], thereby providing further validation of their observations.

Particle reinforcement (blue curve) also demonstrates only moderate effectiveness. In all panels, a clear trend toward abrupt material failure is evident. The application of this method to W matrices is generally considered as ineffective, since its limitations align with the challenges discussed in Chapter 2.2.3 concerning alloys and microstructural modifications. This conclusion is supported by the fundamental literature on composite materials [185, 188, 189]. Consequently, particle reinforcement is not further considered in this work.

W-fiber reinforcement (black curve), while not reaching the performance level of W-foil under non-irradiated conditions as shown in panel (a), demonstrates superior consistency across a wide range of environmental conditions. As evidenced by the stable stress-strain curves in panels (b) and (c), W-fiber reinforced CuCrZr retains its strength and fracture behavior under irradiation and elevated temperatures. This stability positions W-fiber reinforcement as a promising strategy for applications requiring reliable performance in neutron-irradiated environments.

However, directly applying these results to W matrices is not feasible due to the significant differences in material properties between CuCrZr and W. Consequently, a tailored approach is required to adapt these findings effectively to W-based matrices.

A study by Höschen et al. [190], presented at the 20th International Conference on Fusion Reactor Materials (ICFRM-20) in 2021, provides valuable insights into this adaptation. Their study examines the fracture behavior of tungsten fiber-reinforced tungsten ($W_f$/W) composites under both unirradiated and neutron-irradiated conditions across various temperatures.

Figure 6, adapted from Höschen et al. [190], illustrates that the fracture behavior of $W_f$/W composites remains consistent under neutron irradiation at 600°C with displacement levels of 0.7–0.8 displacements per atom (dpa). This consistency represents a notable enhancement in comparison to pure W and any other reinforcing strategy documented in the existing literature [191-195].

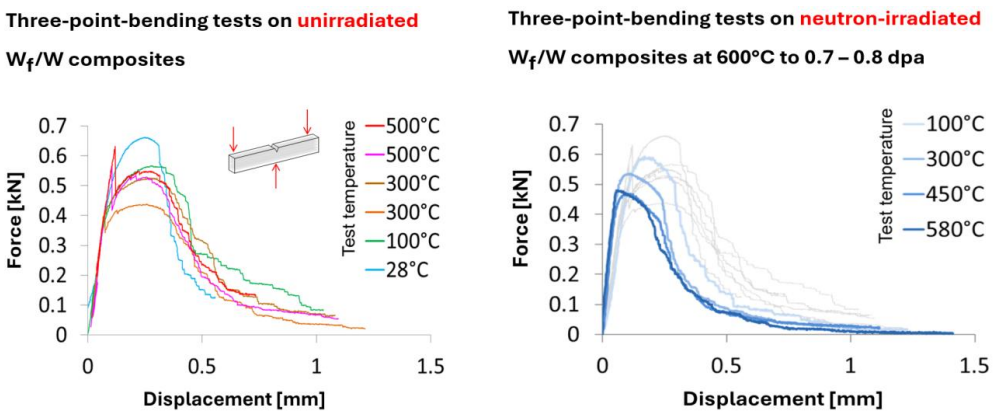


*Figure 6: Fracture behavior of neutron-irradiated and unirradiated $W_f$/W samples, based on [190].*

In summary, while W-foil and W-particle reinforcements exhibit limited potential, W-fiber reinforcement demonstrates stable and reliable performance across a variety of environments, establishing it as the most promising reinforcement strategy for W matrices. This conclusion lays a solid foundation for further exploration of the fundamental mechanisms underlying W-fiber reinforcement, which will be addressed in greater detail in the subsequent chapter.

## 2.4 WFRCs: Mechanisms and Performance

As previously outlined, WFRCs, including $W_f$/W, demonstrate remarkable pseudo-ductile fracture behavior, maintaining their durability even in neutron-irradiated environments. This exceptional performance stems from their ability to activate multiple extrinsic toughening mechanisms that allow for effective energy dissipation and stress redistribution within the material [196-200]. These mechanisms closely correspond to those reported in the literature for reinforced ceramics [188, 189, 201-207]. Figure 7 (left) visually depicts these mechanisms, based on insights from references [36, 185]. These include fiber sliding, pull-out, ductile deformation, crack bridging, and crack deflection, which collectively contribute to the composite's enhanced toughness and resilience [198, 208]. Additional technical details concerning these mechanisms are available in references [209, 210].

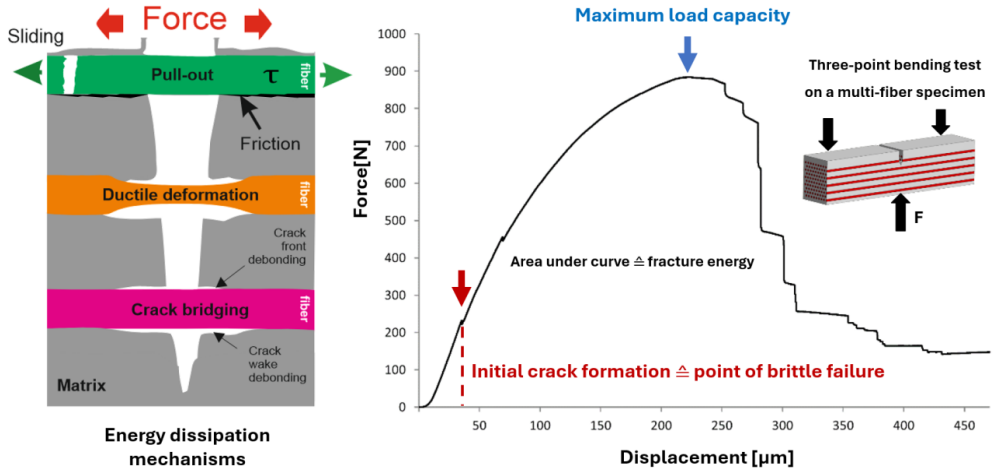


*Figure 7: Left: Energy dissipation mechanisms in fiber-reinforced composites, Right: typical fracture behavior of a brittle and a pseudo-ductile material on three-point bending test specimen, based on [36, 185].*

The right side of Figure 7 illustrates a representative pseudo-ductile fracture curve, obtained from a three-point bending test. In contrast to brittle materials, which fail abruptly after initial crack formation, WFRCs continue to dissipate energy post-cracking, thereby absorbing additional fracture energy within the composite matrix. This sustained energy dissipation significantly enhances the toughness of the material and mitigates the risk of sudden failure [196, 211].

The effectiveness of these extrinsic toughening mechanisms is largely attributed to a thin ceramic interface, typically a few micrometers thick, that separates the fibers from the matrix [206]. This interface is essential for transferring mechanical loads to the fibers and regulating grain growth in both the W-fibers and matrix during high-temperature exposure [205]. By suppressing grain coarsening, the interface also preserves the elongated grain structures, which are essential for maintaining fiber ductility and mechanical integrity at elevated temperatures [212]. This stability is particularly relevant for nuclear fusion applications, which require long-term thermal stability [213-216].

Yttria ($Y_2O_3$) has emerged as the preferred material for this interface due to its exceptional chemical and thermal stability, as well as its ability to withstand high radiation environments with minimal activation [217, 218]. Furthermore, yttria inhibits undesired interactions between the fibers and the matrix, thereby ensuring the long-term performance of the composite [6, 214].

A more detailed examination of these interface mechanisms and the rationale for the selection of yttria are referenced within the relevant literature [219-224].

One significant remaining aspect of WFRC performance that warrants further investigation is the underlying mechanism through which W-fibers achieve their remarkable ductility. W-fibers feature elongated grain structures, which are stabilized through potassium doping, typically in the parts-per-million (ppm) range [212, 225, 226]. This doping process plays a fundamental role in enhancing and stabilizing the mechanical properties of the fibers, particularly after exposure to elevated temperatures and irradiation levels exceeding even 10 dpa, as demonstrated by Riesch et al. and Lürbke et al. in references [227, 228]. The introduction of potassium serves as a crucial factor in controlling the recrystallization behavior of W-fibers, which effectively inhibits excessive grain growth that would otherwise lead to embrittlement and a severe degradation in mechanical performance [213, 229]. The influence of potassium doping is clearly demonstrated in Figure 8, which displays Electron Backscatter Diffraction (EBSD) orientation maps of potassium-doped and undoped W-fibers after undergoing isochronal annealing at temperatures as high as 1600 °C. These findings are adapted from the work of Nikolic et al. [229] and Riesch et al. in reference [33].

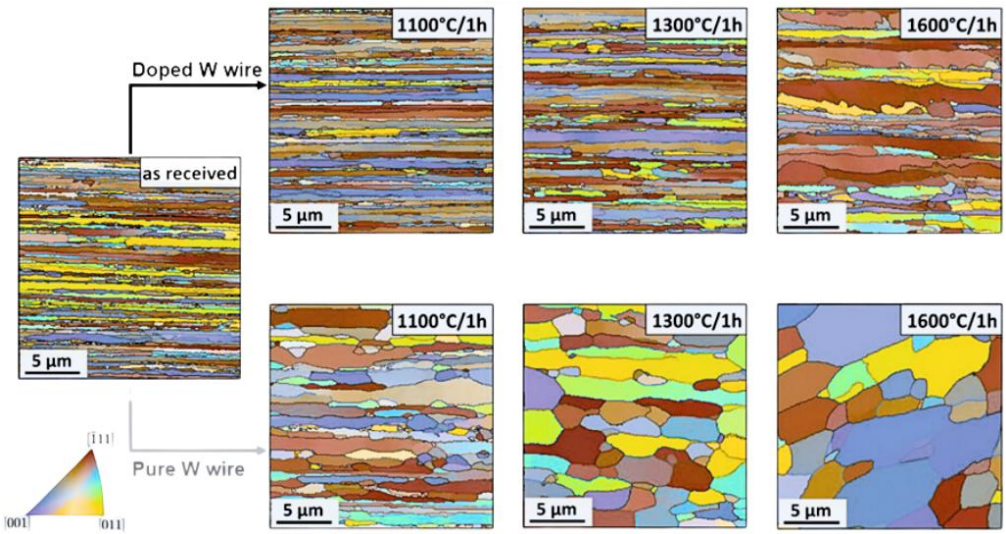


*Figure 8: Electron Backscatter Diffraction (EBSD) orientation maps comparing longitudinal cross-sections of doped (top row) and undoped (bottom row) W-fibers after isochronal annealing treatments at temperatures up to 1600 °C. Each sample was annealed for one hour. All wires, with a diameter of 150 µm, were produced by OSRAM GmbH, Schwabmünchen, Germany. Adapted with permission from [229], © 2018 Elsevier.*

These EBSD results highlight that potassium-doped W-fibers exhibit significantly reduced grain growth compared to their undoped counterparts, a crucial factor in maintaining structural integrity at high temperatures. This enhanced stability contributes directly to the long-term performance and reliability of W-fibers in demanding environments such as those found in nuclear fusion reactors.

Building on the established understanding of the fundamental properties of WFRCs, particularly $W_f$/W composites, the next chapter will provide a comprehensive examination of their current production chain.

# 3 Established Production Chain

This section outlines the key stages for WFRC production, with a particular focus on $W_f$/W composites. These stages include fiber and yarn production, their conversion into textile fabrics, interfacial engineering, and final densification via CVD. Although powder metallurgy can also be used for consolidation, it offers limited control over the microstructure and typically results in composites with lower densities [230, 231]. Therefore, this technique will not be further explored in this chapter.

## 3.1 Production of Fibers and Yarns

The current production chain for both WFRCs and $W_f$/W begins with the fabrication of commercially available potassium-doped W-fibers. These are created by drawing sintered, rolled, swagged, and doped W rods, initially measuring 2 to 4 mm in diameter, into finer filaments [232]. This process reduces the diameter to a typical range between 16 to 150 µm [33], significantly enhancing their tensile strength and flexibility. For comparison, 16 µm fibers achieve tensile strengths of up to 4500 MPa, while typical tensile strengths of 150 µm fibers reach approximately 2500 MPa [232].

In order to enhance both manual handling and structural integrity, thin W-fibers with diameters below 25 µm can be twisted or braided into yarns, forming more robust and cohesive bundles. A study by Treitz in reference [233] compares the mechanical performance of various yarn types before and after CVD processing, providing valuable guidance on selecting the most suitable base material depending on the specific performance criteria. These fibers and yarns are then transformed into textile fabrics, the topic of the next section, which serve as the structural foundation for WFRCs.

## 3.2 Production of Textile Fabrics

The density and final performance of the composite is primarily contingent upon the intrinsic properties and distribution of the reinforcing fibers, as discussed by Gietl et al. in reference [234]. Figure 9 illustrates that precise alignment of warp and weft threads along the x- and y-axes, prior to densification, is essential for achieving optimal structural integrity and reproducible properties.

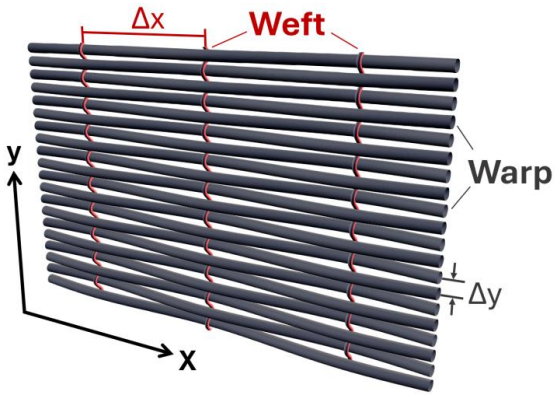


*Figure 9: A typical W-textile fabric made of warp and weft threads with adjustable diameters, and x and y spacing, generated by TexGen v3.13.1 (a), spacing and correlated densities in (b).*

Specialized weaving machinery is utilized to produce such textile fabrics with uniform thread distribution. Figure 10 demonstrates both a schematic and an operational image of a loom, highlighting several key components that are essential for the production of W-textiles.

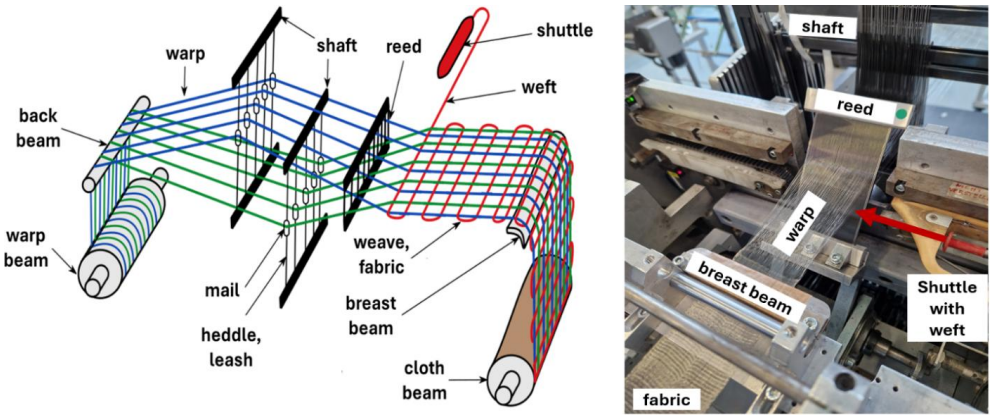


*Figure 10: Schematic of a loom, based on [235], alongside a photograph of a Mageba shuttle loom (type SL 1/80) during operation, highlighting key components.*

The weaving process consists of three primary stages: shedding, picking, and beating, as illustrated in Figure 11.

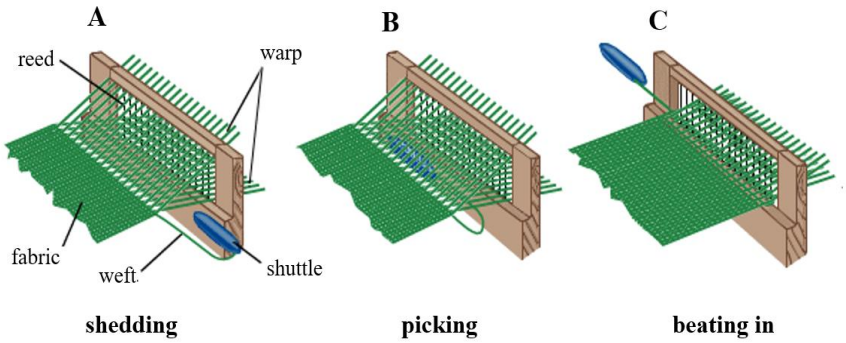


*Figure 11: The three basic motions of weaving, adapted from [236].*

In the shedding phase, the warp threads are alternately raised and lowered, creating a pathway for the shuttle carrying the weft thread to pass through. During the picking phase, the weft thread is inserted. In the final beating phase, the reed secures the weft thread, ensuring consistent spacing. These steps are repeated multiple times until the final textile fabric is formed. The processability of the base materials must be carefully managed, as metal fibers can retain considerable stiffness, as further discussed in references [237-239]. It is therefore essential to achieve an optimal balance between fiber diameter and spacing of the warp and weft materials in order to allow for successful and reproducible textile processing. Once the W-textile fabric has been fabricated, the next critical step is the application of the ceramic interface. This stage must be performed subsequent to the production of the W-textile fabric, as a ceramic surface is inherently brittle and would otherwise detach from the filaments during the complex handling required in the weaving process.

## 3.3 Interface application

As previously discussed in Chapter 2.4, the incorporation of a ceramic interface, particularly yttria ($Y_2O_3$), is essential to achieve the pseudo-ductile characteristics of WFRCs. A variety of advanced coating techniques have been employed to apply this interface to textile fabrics, including both physical [215, 240, 241] and chemical [216] deposition methods. Park et al. [242] provide a comprehensive overview of diverse application methods, each offering variations in material quality, composition, adhesion, and processing complexity. Despite considerable progress in this field, none of the applied techniques has shown adequate effectiveness for complex structures, such as textile fabrics based on yarns [216]. Nevertheless, certain methods, such as magnetron sputtering, have demonstrated the potential to deposit high-quality yttria films on simpler geometries, such as single-fiber-based fabrics, as those illustrated in Figure 9. This physical deposition technique yields high-quality and uniform coatings with thicknesses typically ranging between 1 to 5 micrometers [243]. A schematic overview of a typical magnetron sputtering device is provided in Figure 12 [240, 244].

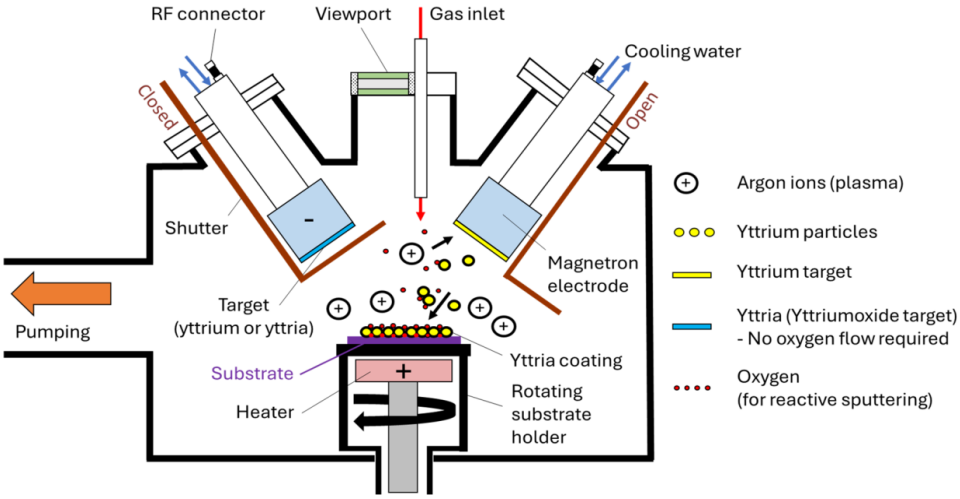


*Figure 12: Schematic illustration of a magnetron sputtering system, showcasing the principle of reactive physical sputtering of yttria, based on insights from references [240, 244].*

The sputtering process is initiated by the generation of an argon plasma in a vacuum environment. The target material is bombarded by fast-moving argon ions, which erode particles from the target and subsequently transport them along magnetic field lines to the desired substrate. This method provides efficient particle transport, facilitates uniform deposition and results in significantly higher deposition rates compared to conventional sputtering techniques [240, 245]. The system can be configured with either a yttria target sputtered directly onto the substrate, or a pure metallic yttrium target combined with a reactive gas such as oxygen. In the reactive process, as shown in the configuration in Figure 12, yttrium atoms, which are ejected from the target, react with oxygen to form yttria, which is then deposited on the substrate – in this case, the W-textile fabric or preform.

The in-situ formation of this oxide film allows for precise control of the chemical composition and stoichiometry, which can be essential for applications that require high quality deposits. However, careful control of the oxygen flow is important to prevent so-called target poisoning, which can significantly reduce the sputtering efficiency and slow the overall deposition process [246-248].

Following yttria deposition, the coated W-textile fabrics can ultimately be integrated into a solid W matrix to form a $W_f$/W composite. The methodological focus is on the CVD technique, which is considered as the key technology for the densification step in this work.

## 3.4 Chemical Vapor Deposition (CVD) of Tungsten

Chemical Vapor Deposition (CVD) is a highly versatile technique widely employed to produce high-purity, high-performance coatings, which are essential in industries such as microelectronics, aerospace, and energy [249-251]. One of the major advantages of CVD is its ability to achieve uniform deposition of thin films on a diverse range of substrates, including those with intricate geometries, by regulating the reaction or decomposition of gaseous precursors [252, 253]. Furthermore, CVD provides precise control over critical material properties, such as particle size, chemical composition, and film thickness, thereby ensuring compliance with strict quality standards [254].

For pure W deposition, various precursors are available, including halides like tungsten hexafluoride ($WF_6$) and tungsten hexachloride ($WCl_6$), as well as carbonyl compounds such as tungsten hexacarbonyl ($W(CO)_6$). These precursors can be thermally decomposed or chemically reduced using agents like hydrogen ($H_2$), silane ($SiH_4$), disilane ($Si_2H_6$), or diborane ($B_2H_6$) [255-259]. This thesis specifically investigates the reduction of $WF_6$ with $H_2$, which proceeds according to the following reaction:

$$WF_{6(g)} + 3\,H_{2(g)} \rightarrow W_{(s)} + 6\,HF_{(g)} \qquad (3)$$

Figure 13 illustrates the sequential steps of CVD utilizing this reaction, highlighting the essential roles of mass transport, adsorption, and chemical reactions in forming high quality W coatings, as well as the desorption and removal of undesirable byproducts such as hydrofluoric acid (HF).

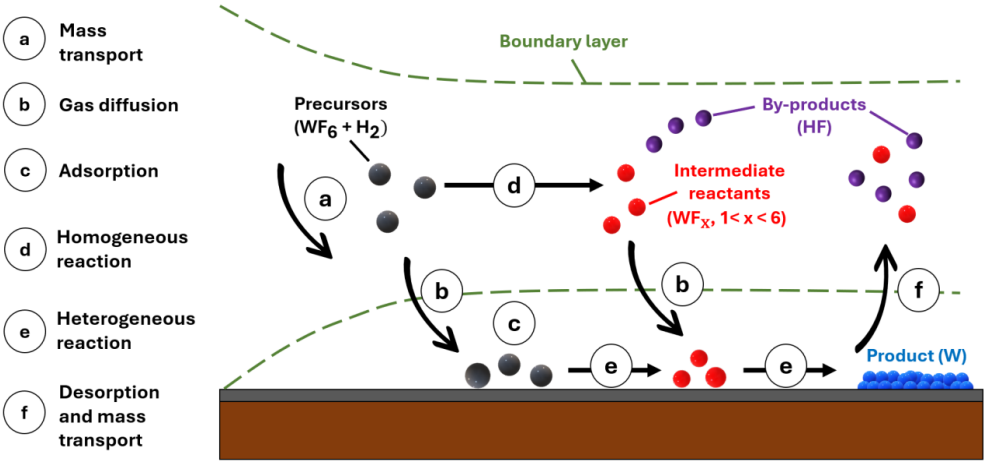


*Figure 13: Schematic of a typical CVD process using $WF_6$ and $H_2$ as precursors. The precursors (black) undergo mass transport (a), diffuse through the boundary layer (b), and either directly adsorb onto the substrate (c) to form the product (W), or first undergo homogeneous reactions in the gas phase (d), forming intermediates (red). These intermediates may subsequently adsorb onto the substrate and further react or decompose, resulting in W deposition (blue). By-products such as hydrofluoric acid (HF, purple), are removed via desorption and mass transport mechanisms (f). Based on insights from [260].*

CVD encompasses several process variants, each tailored to specific material systems and operational conditions. Prominent techniques within this spectrum include Atmospheric Pressure CVD (APCVD), Low-Pressure CVD (LPCVD), Plasma-Enhanced CVD (PECVD), Metal-Organic CVD (MOCVD), and Atomic Layer Deposition (ALD). These processes differ fundamentally in factors such as applied pressure, temperature, precursor chemistry, reactor design, and energy input methods [261-276].

The selection of an appropriate CVD process is primarily guided by the chemical properties and reactivity of the precursor materials, as well as the desired characteristics of the resulting layers and surface structures [277]. LPCVD is particularly well-suited to manage the specific interaction between the two selected precursors $H_2$ and $WF_6$, as evidenced by references [257, 278].

In LPCVD, the low-pressure environment primarily promotes surface-driven heterogeneous reactions across a broad temperature range of 300-800 °C [120]. This facilitates the direct deposition of W atoms onto the target substrate, sealing the W-textile fabrics in the process to form a dense $W_f$/W composite. Concurrently, maintaining a low-pressure regime suppresses undesirable homogeneous gas-phase reactions, thereby ensuring high film quality and reducing equipment wear [279-281].

Optimizing the deposition conditions necessitates a comprehensive understanding of reaction kinetics, as they govern the reaction type, deposition rate, film quality, process efficiency, and scalability. In particular, understanding the influence of key parameters such as temperature, total pressure, and precursor partial pressures on deposition rates is crucial, as these factors play a decisive role in scalability and set the fundamental limitations of the process [282, 283].

In references [284, 285], Raumann et al. proposed an advanced kinetic model to address inconsistencies in the literature regarding the reaction order of $WF_6$, which are noted in references [286-292]. Their enhanced model delineates distinct regimes in which the reaction order and the W-deposition rate $R_W$ is either dependent or independent of the $WF_6$ partial pressure. Each regime is characterized by separate rate equations, adapted here in equations (4) and (5):

$$R_{WF_6,indep} = k_0 \exp\left(\frac{-E_{A,1}}{RT}\right)[p_{WF_6}]^0[p_{H_2}]^{1/2} \quad (4)\ [284]$$

**Where:**

$R_{WF_6,indep}$ = Deposition rate of W independent of $p_{WF_6}$ [$ms^{-1}$]

$k_0$ = constant = $(38.22 \pm 4.85) \times 10^{-6}\ ms^{-1}\ Pa^{-\frac{1}{2}}$

$E_{A,1}$ = Activation energy for $p_{WF_6}$ − independent rate equation = $73.7 \pm 0.9\ \frac{kJ}{mol}$

$R$ = Gas constant [$8.314\ Jmol^{-1}K^{-1}$]

$T$ = Temperature [K]

$p_{WF_6}$ = partial pressure of $WF_6$

$p_{H_2}$ = partial pressure of $H_2$

n = reaction order (here: 0 for $WF_6$ and ½ for $H_2$)

$$R_{WF_6,dep} = \left( \frac{1}{k_1 p_{WF_6}} + \frac{1}{k_2 \exp\left(\frac{-E_{A,2}}{RT}\right) [p_{H_2}]^{1/2} [p_{WF_6}]^{1/6}} \right)^{-1} \quad (5)\ [293]$$

**With:**

$R_{WF_6,dep}$ = Deposition rate of W dependent of $p_{WF_6}$ [$ms^{-1}$]

$k_1$ = constant = (32.63 ± 2.88) $\times 10^{-9}$ $ms^{-1}Pa^{-1}$

$k_2$ = constant = (45.79 ± 1.28) $\times 10^{-7}$ $ms^{-1}$ $Pa^{-\frac{2}{3}}$

$E_{A,2}$ = Activation energy for $p_{WF_6}$ − dependent rate equation = 64 $\frac{kJ}{mol}$

For precursor ratios greater than 3, equations (4) and (5) can be summarized into equation (6), which selects the minimum between the $WF_6$-dependent and $WF_6$-independent rates. This formulation effectively captures the transition between the two different reaction regimes, thereby providing a framework for understanding and improving the process conditions.

$$R_W = \min\left(R_{WF_6,dep}, R_{WF_6,indep}\right) \quad (6)\ [285]$$

**With:**

$R_W$ = General Deposition rate of W [$ms^{-1}$]

To further illustrate the behavior of W deposition rates $R_W$ under varying conditions, Figure 14 through Figure 16 present the calculated values of $R_W$ based on equation (6) as functions of temperature, pressure, and precursor ratios. These values are derived under the assumption that all other parameters remain constant.

- Figure 14 demonstrates that an increase in temperature results in an exponential growth in deposition rates, spanning several orders of magnitude between 300°C to 800°C. However, excessively high temperatures may trigger undesired side reactions that compromise deposit quality. Thus, striking a balance between deposition rate and film quality is considered crucial.
- Figure 15 demonstrates that $R_W$ also increases with pressure, although the rate of increase decelerates at higher pressures. Similar to elevated temperatures, excessively high pressure may shift the reaction mechanism from surface-driven processes to gas-phase nucleation, adversely impacting the film uniformity and quality. Therefore, it is essential to establish and maintain a suitable pressure range to ensure high-quality depositions within reasonable processing times.
- Figure 16 examines the relationship between $R_W$ and the precursor ratios, which have been plotted into two segments (a) and (b). At ratios below 7.5, the limited availability of $H_2$ significantly restricts surface reactions, leading to lower deposition rates and thus rendering this regime inefficient. At ratios exceeding 15, the growth rate plateaus, as the surplus hydrogen does not significantly enhance the deposition rates. Accordingly, a ratio of 12.5:1 has been assumed in the remaining figures, representing a reasonable compromise between hydrogen availability and W deposition rates, thereby maximizing growth efficiency without unnecessary excess.

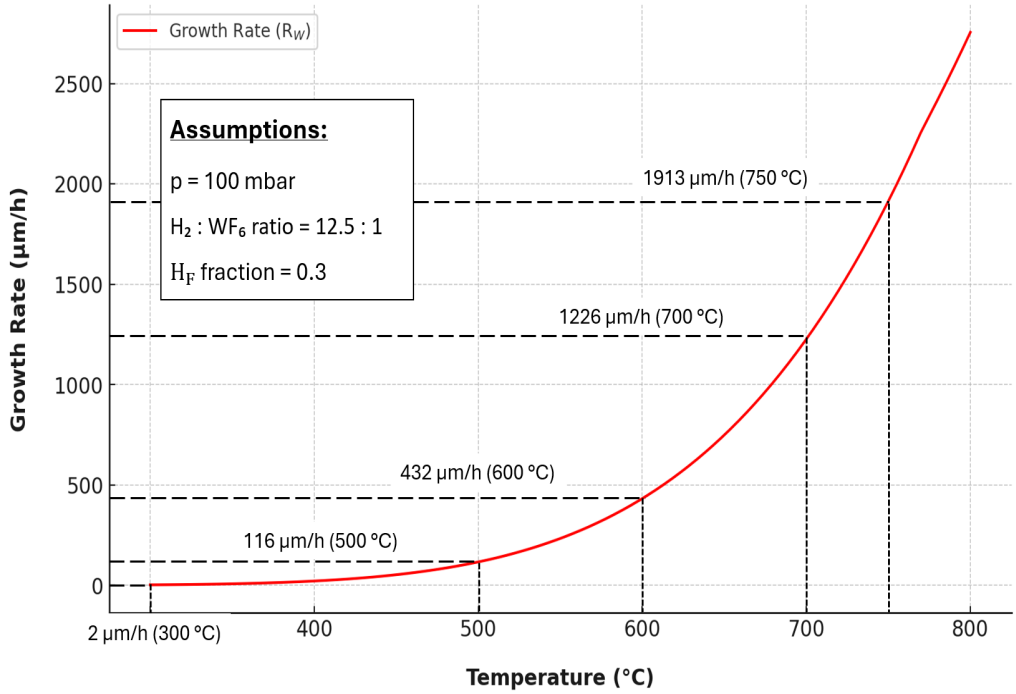


*Figure 14: W growth rate Rw as a function of temperature, varying from 300 °C to 800 °C. Calculation is based on equation (6), assuming constant conditions of 100 mbar, a $H_2$:$WF_6$ ratio of 1:12.5 and an HF-fraction of 0.3.*

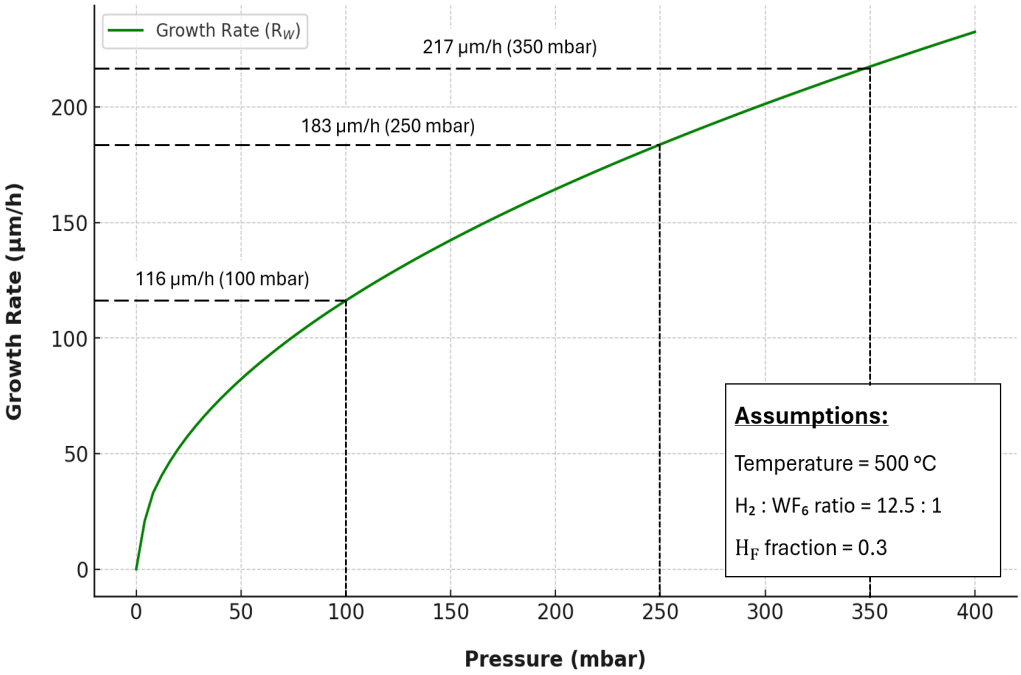


*Figure 15: W growth rate Rw as a function of pressure, varying from 0 to 400 mbar. Calculation is based on equation (6), assuming constant conditions of 500 °C, a $H_2$:$WF_6$ ratio of 1:12.5 and an HF-fraction of 0.3.*

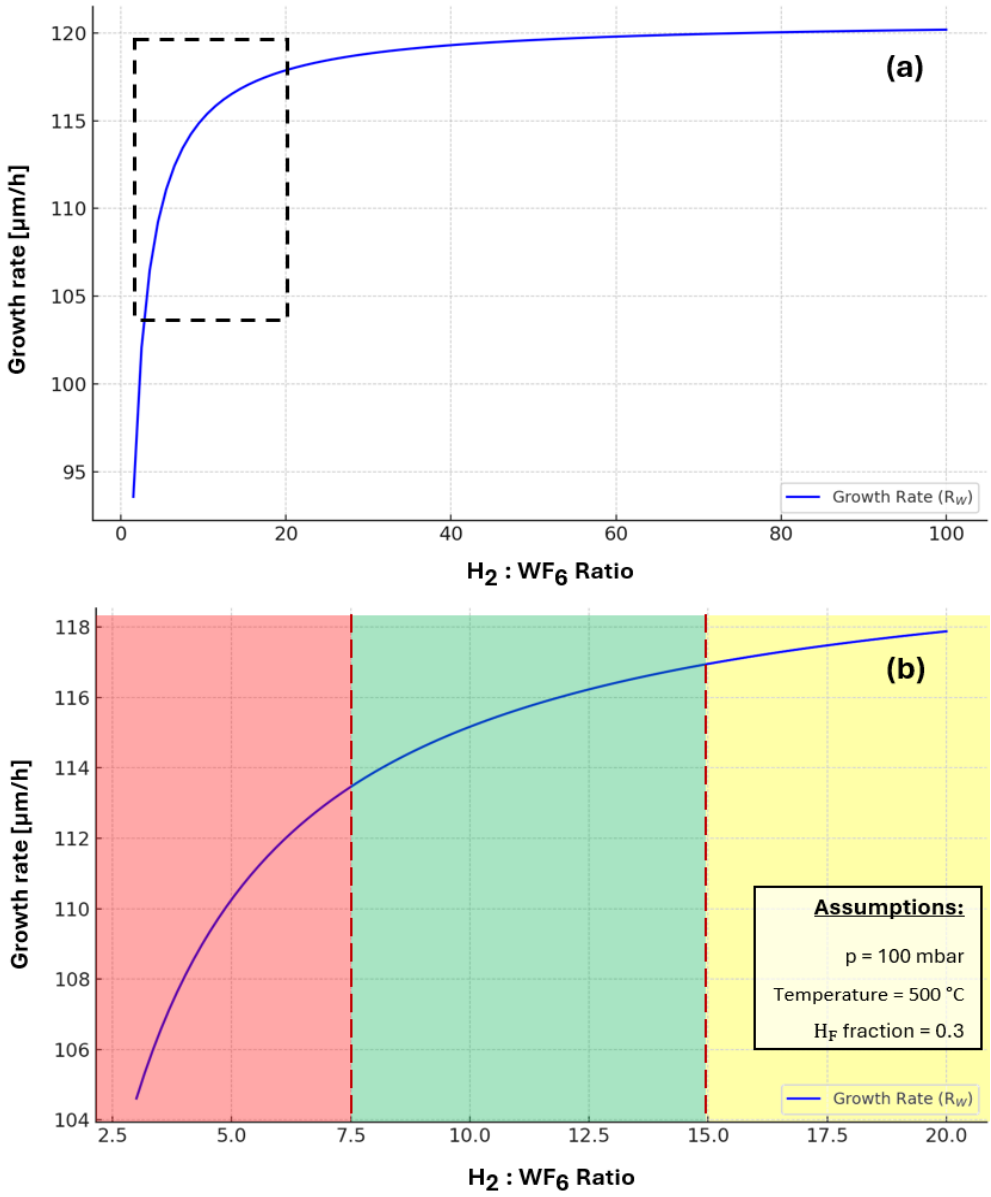


*Figure 16: W growth rate Rw as a function of precursor ratios, varying from 0 to 80 in (a) and from 0 to 20 in (b). Ratios below 7.5 are categorized as inefficient (red), those from 7.5 to 15 provide reasonable growth conditions (green), and ratios above 15 are deemed non-economic (yellow). The calculations and associated categories are based on constant parameters of 500 °C, 100 mbar, and an HF fraction of 0.3.*

Having outlined the current production chain – including the fundamentals of CVD technology, the selection of suitable process variants and precursors, and a brief examination of the reaction kinetics and parameter constraints – the next step is to translate these theoretical principles into practical applications. The objective is to enable the large-scale production of a resilient $W_f$/W composite material with consistent material properties. This goal was initially pursued using the established Batch-LPCVD process, which is illustrated in Figure 17 and builds on insights from reference [294].

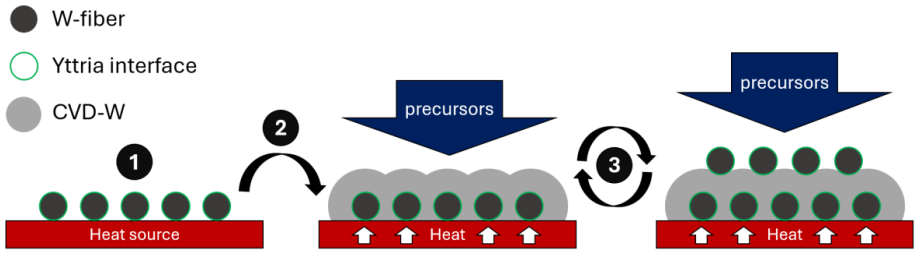


*Figure 17: Schematic representation of the Batch-LPCVD process. Step 1: Position the yttria-coated W-textile fabrics evenly across the heat source. Step 2: Initiate the precursor flow and apply heat to promote the deposition of CVD-W around the fibers, thereby sealing the fabrics. Step 3: Sequential stacking additional layers, repeating Step 2 until the desired component thickness is attained, adapted from [294].*

Considerable advancements have been achieved in scaling this approach, with composite sample sizes expanded from 50 x 50 $mm^2$ to dimensions comparable to those of ITER monoblocks. This milestone, first reported by Schwalenberg et al. in reference [4], achieved fiber volume fractions between 10.4% and 12.16%. Furthermore, the study investigated the fracture mechanics of these upscaled materials, providing insights that complement the fracture toughness estimates proposed by Gietl et al. in reference [196]. Nevertheless, the findings presented in reference [4] also highlight notable reproducibility limitations, which will be further examined in the subsequent chapter.

# 4 Reproducibility Limitations

This chapter introduces a fundamental challenge inherent to the original Batch-LPCVD process: the limited reproducibility of the resulting composite material properties. Figure 18, adapted from data presented in reference [4], illustrates this issue. Specifically, Figure 18 (a) highlights the variability in mechanical responses among multiple $W_f$/W specimens produced from the same material, while Figure 18 (b) reveals the presence of prominent voids within the composite structure. Such inconsistencies substantially limit the material's suitability for commercial applications, where consistent material properties and stringent quality standards are paramount.

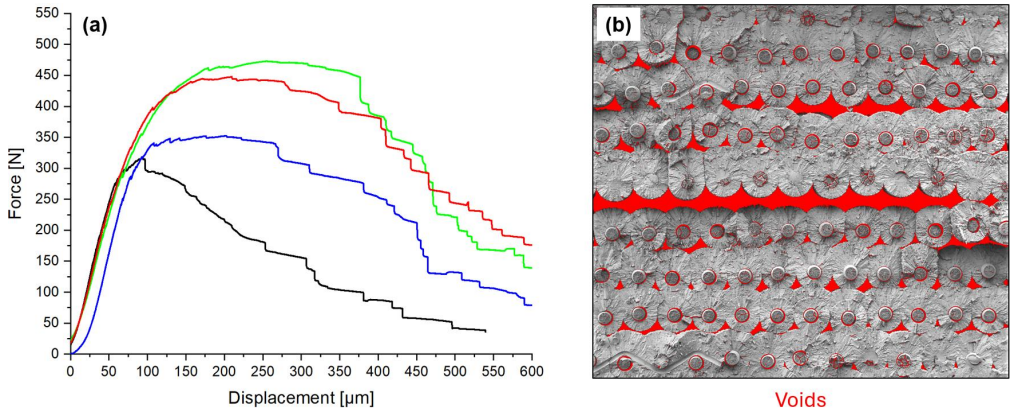


*Figure 18: (a) Three-point bending tests of CVD-$W_f$/W samples made from the same composite material at room temperature, adapted from [4], illustrating the variability in mechanical response; (b) SEM image of the composite structure, highlighting voids (in red) that contribute to these inconsistencies.*

In order to justify further upscaling efforts for $W_f/W$ composites, it is imperative to first resolve the aforementioned reproducibility issues. The initial publication of this thesis, entitled "*Bulk Tungsten Fiber-Reinforced Tungsten ($W_f/W$) Composites Using Yarn-Based Textile Preforms*", directly addresses this challenge. As indicated by the title, this study examines the incorporation of yarn-based textile preforms into the composite matrix as an alternative to conventional fabrics composed of individual W-filaments (illustrated in Figure 9). This approach was originally proposed in references [3, 295, 296].

The central objective of this study is to investigate whether, and to what extent, the consistency of material performance in $W_f/W$ composites can be improved when the textile preforms integrated into the composite are made either exclusively from yarns or from a combination of yarns and single filaments. In order to ensure comparability with the results presented in Figure 18, the dimensions of the manufactured composites were adapted to the specifications documented in reference [4].

Within the scope of this dissertation, several additional measures were developed as essential prerequisites for attaining the results reported in Publication [1]. These measures, briefly summarized in Table 1, encompass methodological adjustments such as the redefinition of process protocols, optimization of monitoring procedures, and the replacement and repositioning of key system components. Without these targeted interventions, the practical implementation of the proposed approach would have been unfeasible.

*Table 1: Applied practical measures to increase deposition homogeneity.*

| Challenge | Measure(s) |
|---|---|
| Frequent oxidation of samples | Modify process protocol and increase Argon volume flows during operation |
| High mechanical stress induced by thermal cycling | Integrate a base plate made of the substrate material, decrease heating- and cooling rates |
| Broken CVD-W parts from the precursor shower embedded in the sample | Clean and sandblast all surface structures to increase the adhesion of W at the precursor shower |
| Limited Monitoring and process control | New Code and integration of new monitoring features |
| High risk of sudden production stoppage | Identify wear parts, their service life and set regular maintenance intervals |
| Sodium hydroxide (NaOH) and Sodium fluoride (NaF) deposits, resulting in pressure fluctuations | Installation of a new bypass valve enabling purging during operation |
| Regular blocking of the turbo pump | Adjusting the process protocol and redirecting gas flow by repositioning valves |
| Inhomogeneous W deposition | Integrate precursor heating system, adjust flow conditions by increasing precursor pipe diameters |
| High manual efforts and wavy surface | New Sample holder design + new precursor shower design |

Additional details regarding the implemented measures, the utilized WILMA chemical processing plant, and an overview of the developed codes and models are provided in the Appendix.

However, it is important to note that a comprehensive technical description of the processing plant exceeds the scope of this thesis. Nonetheless, the first publication, revisited in the following chapter, is intended to provide a coherent and concise summary of the core challenge, the investigated approach, and the achieved results.

Journal of
Nuclear Engineering

# Yarn-Based Tungsten Fiber-Reinforced Tungsten

**Volume 4 · Issue 2** | June 2023

MDPI

mdpi.com/journal/jne
ISSN 2673-4362

Journal of
*Nuclear Engineering*

Article

# Bulk Tungsten Fiber-Reinforced Tungsten ($W_f$/W) Composites Using Yarn-Based Textile Preforms

Alexander Lau, Jan Willem Coenen, Daniel Schwalenberg, Yiran Mao, Till Höschen, Johann Riesch, Leonard Raumann, Michael Treitz, Hanns Gietl, Alexis Terra et al.

Special Issue
Feature Paper Special Issue for Editorial Board Members (EBMs) of Journal of Nuclear Engineering
Edited by
Prof. Dr. Dan Gabriel Cacuci

MDPI

https://doi.org/10.3390/jne4020027

Journal of
*Nuclear Engineering*

MDPI

*Article*

# Bulk Tungsten Fiber-Reinforced Tungsten ($W_f$/W) Composites Using Yarn-Based Textile Preforms

**Alexander Lau [1,2,*], Jan Willem Coenen [1,3,*], Daniel Schwalenberg [1,4], Yiran Mao [1], Till Höschen [5], Johann Riesch [5], Leonard Raumann [1], Michael Treitz [1,4], Hanns Gietl [6], Alexis Terra [1], Beatrix Göhts [1], Christian Linsmeier [1], Katharina Theis-Bröhl [7] and Jesus Gonzalez-Julian [2]**

1 Forschungszentrum Jülich GmbH, Institut für Energie- und Klimaforschung-Plasmaphysik, 52425 Jülich, Germany
2 Department of Ceramics, RWTH Aachen University, 52074 Aachen, Germany
3 Department of Engineering Physics, University of Wisconsin-Madison, Madison, WI 53706, USA
4 Department of Mechanical, Automotive and Aeronautical Engineering, University of Applied Sciences Munich, 80335 Munich, Germany
5 Max-Planck-Institut für Plasma Physik, 85748 Garching, Germany
6 Fusion Safety Program, Idaho National Laboratory, Idaho Falls, ID 83415, USA
7 University of Applied Sciences Bremerhaven, 27568 Bremerhaven, Germany
* Correspondence: a.lau@fz-juelich.de (A.L.); j.w.coenen@fz-juelich.de (J.W.C.)

**Abstract:** The use of tungsten fiber-reinforced tungsten composites ($W_f$/W) has been demonstrated to significantly enhance the mechanical properties of tungsten (W) by incorporating W-fibers into the W-matrix. However, prior research has been restricted by the usage of single fiber-based textile fabrics, consisting of 150 µm warp and 50 µm weft filaments, with limited homogeneity, reproducibility, and mechanical properties in bulk structures due to the rigidity of the 150 µm W-fibers. To overcome this limitation, two novel textile preforms were developed utilizing radial braided W-yarns with 7 core and 16 sleeve filaments (R.B. 16 + 7), with a diameter of 25 µm each, as the warp material. In this study, bulk composites of two different fabric types were produced via a layer-by-layer CVD process, utilizing single 50 µm filaments (type 1) and R.B. 16 + 7 yarns (type 2) as weft materials. The produced composites were sectioned into KLST-type specimens based on DIN EN ISO 179-1:2000 using electrical discharge machining (EDM) and subjected to three-point bending tests. Both composites demonstrated enhanced mechanical properties with pseudo-ductile behavior at room temperature and withstood over 10,000 load cycles between 50–90% of their respective maximum load without sample fracture in three-point cyclic loading tests. Furthermore, a novel approach to predict the fatigue behavior of the material under cyclic loading was developed based on the high reproducibility of the composites produced, especially for the composite based on type 1. This approach provides a new benchmark for upscaling endeavors and may enable a better prediction of the service life of the produced components made of $W_f$/W in the future. In comparison, the composite based on fabric type 1 demonstrated superior results in manufacturing performance and mechanical properties. With a high relative average density (>97%), a high fiber volume fraction (14–17%), and a very homogeneous fiber distribution in the CVD-W matrix, type 1 shows a promising option to be further tested in high heat flux tests and to be potentially used as an alternative to currently used materials for the most stressed components of nuclear fusion reactors or other potential application fields such as concentrated solar power (CSP), aircraft turbines, the steel industry, quantum computing, or welding tools. Type 2 composites have a higher layer spacing compared to type 1, resulting in gaps within the matrix and less homogeneous material properties. While type 2 composites have demonstrated a notable enhancement over 150 µm fiber-based composites, they are not viable for industrial scale-up unlike type 1 composites.

**Keywords:** tungsten; metal matrix composites; CVD; yarns; preforms; textiles; fusion



**Citation:** Lau, A.; Coenen, J.W.; Schwalenberg, D.; Mao, Y.; Höschen, T.; Riesch, J.; Raumann, L.; Treitz, M.; Gietl, H.; Terra, A.; et al. Bulk Tungsten Fiber-Reinforced Tungsten ($W_f$/W) Composites Using Yarn-Based Textile Preforms. *J. Nucl. Eng.* **2023**, *4*, 375–390. https://doi.org/10.3390/jne4020027

Academic Editor: Dan Gabriel Cacuci

Received: 29 March 2023
Revised: 25 April 2023
Accepted: 27 April 2023
Published: 4 May 2023

## 1. Introduction

### 1.1. Mechanical Properties of Tungsten and $W_f$/W Composites

Tungsten (W) is currently the prime candidate material for the first wall armor and in particular for the highly loaded components such as the divertor of future nuclear fusion reactors. However, pure tungsten is inherently brittle below the ductile–brittle transition temperature (DBTT), and cracking could lead to a complete loss of function of the respective wall component [1–7]. Another issue for the mechanical properties of tungsten is the randomly distributed ultimate tensile strength (UTS). The weakest point in the component determines the fracture toughness, and therefore the material's lifetime is difficult to predict [8–11]. To mitigate this problem and to improve the toughness and reproducibility of tungsten-based components, tungsten fiber-reinforced tungsten ($W_f$/W) metal matrix composites are being developed [10,12–22]. As shown in Figure 1, extrinsic toughening mechanisms such as fiber pull-out, ductile deformation, and/or crack bridging are applied to promote a pseudo-ductile behavior that significantly increases the application range of $W_f$/W composites compared to brittle tungsten. More information can be found in [6,13,23,24].

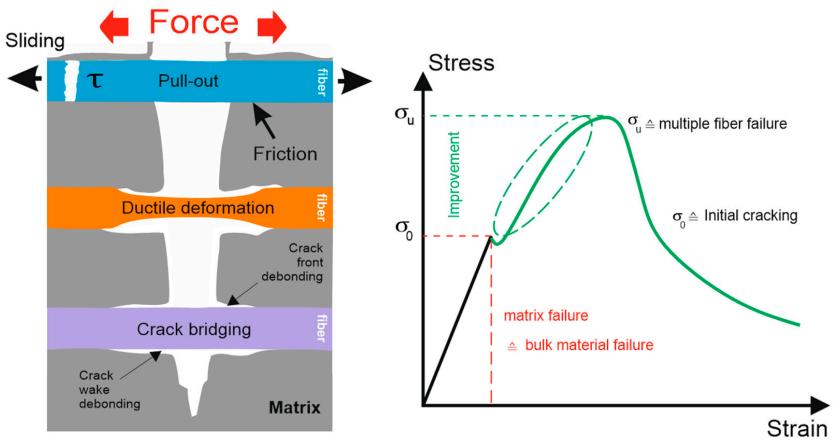


**Figure 1.** Energy dissipation mechanisms in a fiber-based metal matrix composite: pull-out of fibers, ductile deformation, crack bridging and crack wake, and front debonding of the applied ceramic oxide-based interface [20,25].

### 1.2. Production of $W_f$/W via Chemical Vapor Deposition (CVD)

One of the most reliable methods to produce a dense $W_f$/W composite is the use of the heterogeneous reaction between tungsten hexafluoride ($WF_6$) and hydrogen ($H_2$), forming solid tungsten on the W-fibers and gaseous hydrogen fluoride (HF). The toxic HF is extracted and neutralized with an alkalic sodium hydroxide solution. The process conditions for the chemical vapor deposition vary between 300–800 °C and 1–1000 mbar in a vacuum reaction chamber, using argon gas to prevent oxidation. The modelling of the highly sensitive reaction kinetics and the influence of each production parameter has been studied and is further described in [26–29]. Based on this knowledge and a series of process optimizations such as the integration of a preheating system, it is now possible to deposit pure tungsten very reproducibly on the fiber surfaces in a layer-by-layer process. Here, the theoretical and practical deposition rates show very high agreement.

A visual representation of the layer-by-layer technique is provided in Figure 2, which illustrates how the required composite thickness (h) is achieved.

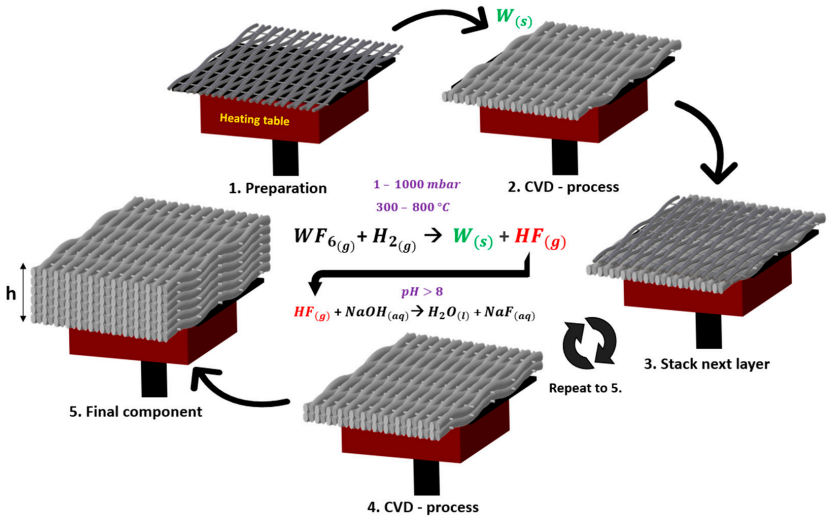


**Figure 2.** Layer-by-layer CVD process principle.

In order to maintain the performance of the material under fusion conditions and to improve the mechanical properties even further, an oxide–ceramic interface, e.g., yttria interface, is necessary [5–7,25,30–34]. To merely demonstrate the advantages of the fiber-reinforcement, the application of an interlayer is not essential for initial experiments since the samples are not tested in a fusion environment. Therefore, the samples used in this work were obtained without an interlayer to reduce the fabrication effort.

### *1.3. Development of New Tungsten Preforms*

Up to now, the state of the art has been the usage of preforms, which are depicted in Figure 3. These preforms are based on single filaments of potassium-doped tungsten wires with diameters of 150 µm warp and 50 µm weft filaments [17,35].

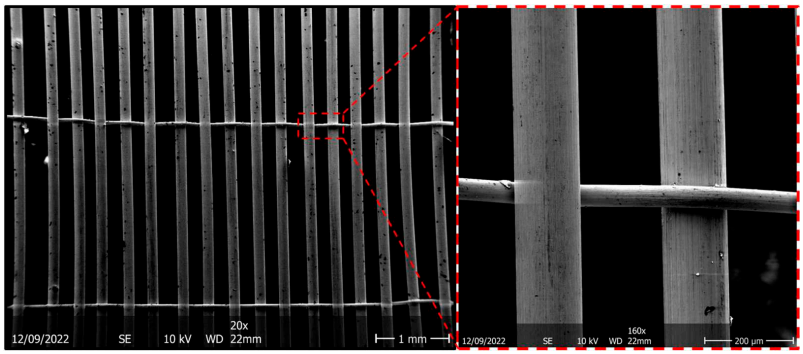


**Figure 3.** Preform type based on single-fibers microscopic structure. Image was obtained with scanning electron microscope (SEM) Carl Zeiss LEODSM982.

In Figure 4, 25 layers of these base fabrics have been stacked with the CVD process to reach the geometrical range of the potential application field. Despite having remarkable mechanical properties, as presented in [17], single wire-based fabrics are not suitable for an industrial scale-up when stacked layer-by-layer due to the high risk of delamination between each individual layer caused by the high stiffness of the 150 µm fibers. Therefore,

the layer-spacing is not homogeneously distributed, which makes it challenging to achieve consistent mechanical properties.

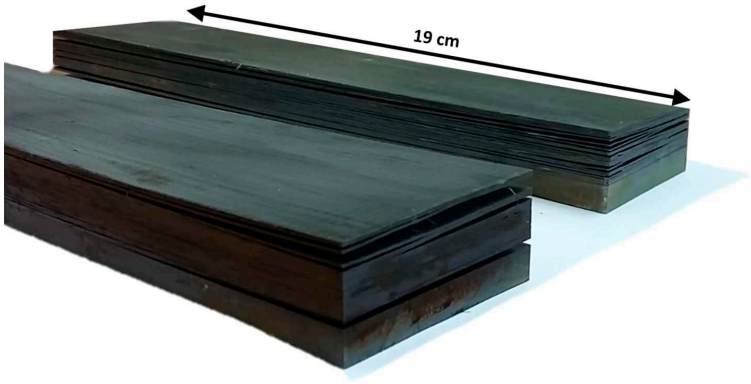


**Figure 4.** CVD stacking of 25 layers of single wire-based preforms [17].

In order to enhance the mechanical properties of the base fabrics, the utilization of higher strength fiber bundles was targeted through the introduction of two new yarn-based textile preforms, as detailed in [36,37]. These preforms, as illustrated in Figure 5, were constructed using 20 µm W-fibers, with the goal of increasing the flexibility of the base fabrics and ensuring sufficient flattening of each layer.

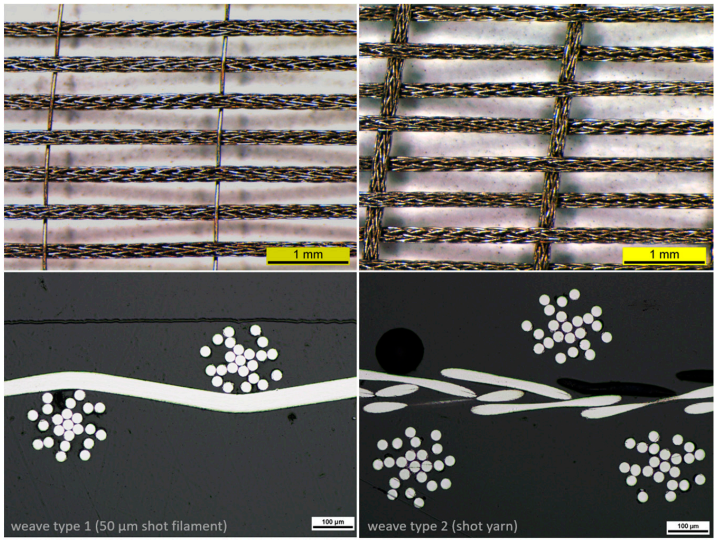


**Figure 5.** Comparison: (**a**) Fabric type 1 with 50 µm weft filament; (**b**) fabric type 2 with weft yarn. Top pictures show the tungsten fabrics as fabricated and were obtained via Zeiss optical microscope. Button images show metallographic cuts of each type and were made with a Nikon Eclipse LV 150 NL.

Both fabrics use radial braided yarns with 7 core and 16-sleeve filaments (R.B. 16 + 7) for the warp material. This yarn was selected due to its superior mechanical properties after infiltration with CVD-W, a high fiber volume fraction, high microstructure homogeneity,

and an increased flexibility compared to single fibers with a diameter of 150 µm [16]. As a weft material, the fabric type 1 (a) uses a single filament with a diameter of 50 µm, and type 2 (b) uses the yarn R.B. 16 + 7. In order to upscale $W_f/W$ composites for industrial use, it is important to determine which new fabric type performs best and results in the best mechanical properties when processed into a solid composite. Additionally, it is important to investigate if the yarn-based fabrics represent an appropriate base material for a layer-by-layer CVD-process. To evaluate the mechanical properties of the fibers, mechanical cyclic loading tests must be conducted to demonstrate that $W_f/W$ does not exhibit brittle fracture behavior under cyclic loading.

## 2. Comparison of Bulk $W_f/W$ Using Yarn-Based Preforms

### *2.1. Production*

The two new base fabrics depicted in Figure 5 were cut into pieces measuring $5.8 \times 19.5\ cm^2$ using electrical discharge machining (EDM). After cutting, the preforms were cleaned and dried before being clamped in a specimen holder as shown in Figure 6 to stretch and smooth the fabrics as much as possible. Here, it can be seen that three fabrics can be coated in parallel, but only one multi-layer sample for each fabric type could be produced due to the limited amount of the base material.

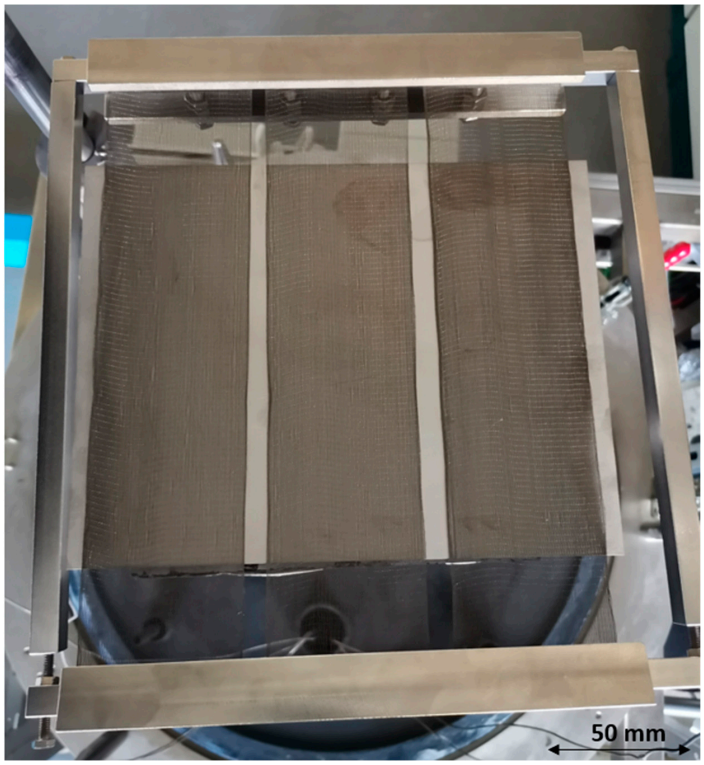


**Figure 6.** CVD process applied on three parallel coated fabrics.

For all batches, the heating table was maintained at a temperature of 540 °C, and the reaction chamber was kept at an absolute pressure of 120 mbar.

A gas flow rate of 12,500 sccm for hydrogen and 1000 sccm for $WF_6$ (with a $H_2$:$WF_6$ ratio of 12.5:1) was utilized. The use of a weft yarn in the manufacturing process resulted in an inhomogeneous spacing between the warp and weft materials. In order to ensure,

that any 2D gaps between the warp and weft materials were closed with CVD-W, a higher process time of 3 h for type 2 was selected compared to 2.5 h for type 1.

### 2.2. Optical Analysis, Density and Fiber Volume Fraction

Figure 7 shows a representative top and side view of the bulk materials produced, based on the example of type 2. It can be seen in the upper picture that the 2D surface of each batch could be closed completely. This shows that the chosen parameters are suitable to produce a homogenous matrix.

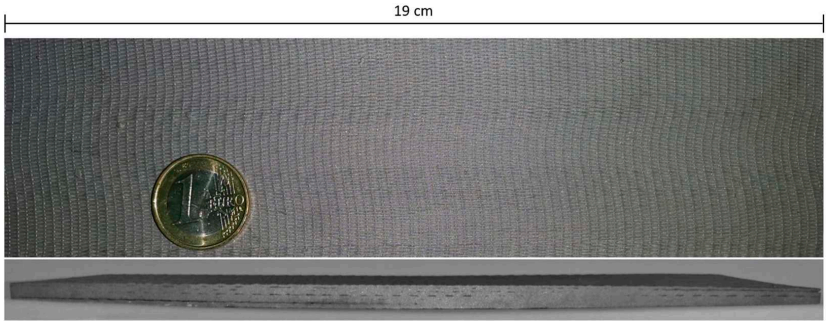


**Figure 7.** Representative images of top and side view for both WfW composites after CVD stacking (type 2).

Figure 8 shows a comparison of the cross-sectional surface of bulk composite type 1 (a) and type 2 (b) on a macroscopic scale. The cross-sectional microstructure of each sample is shown in Figure 9 for fabric type 1 and in Figure 10 for the type 2.


**Figure 8.** Solid composites of six layers via CVD: Fabric 1 (**a**), Fabric 2 (**b**).


**Figure 9.** $W_f/W$ composite based on type 1. Image obtained with a Zeiss optical microscope. (**a**) shows the side view of the composite, (**b**) shows the front view.

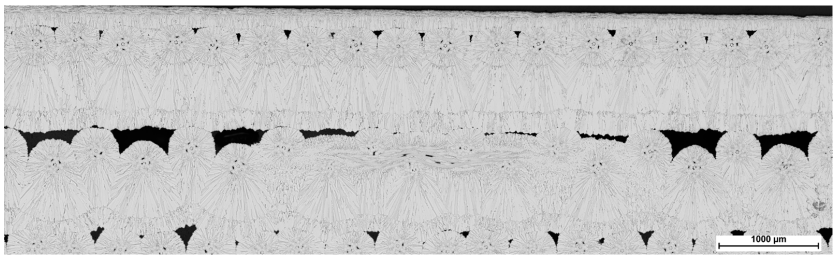


**Figure 10.** Front view of the $W_f/W$ composite based on type 2. Image obtained with a Zeiss optical microscope.

The composite material comprised of fabric type 1 fabrics exhibit a macroscopic resemblance to solid tungsten blocks. However, upon close examination through larger magnification, it is revealed that the material displays small, perforated structures within each yarn. Here, both the constituent yarns and fabric layers exhibit a homogeneous distribution throughout the material. Conversely, the interlayer spacing in type 2 composites is relatively wide, leading to noticeable macroscopic gaps. Since composite type 1 had a shorter deposition time, the thickness of CVD-W between each layer was lower compared to type 2. This results in a significantly higher fiber volume fraction, ranging between 14–17%, in contrast to 7–10% in type 2. Despite the higher fiber volume fraction, the measured relative average density of the type 1 composite, determined using the Archimedean principle with five cut specimens, was only slightly higher at $97.14 \pm 0.3\%$ compared to $96.59 \pm 0.5\%$ for type 2. It is important to note, that the cut specimens for Type 2 had a more similar appearance to those of type 1 than those depicted in Figure 8b. Cutting specimens at more inhomogeneous areas of the produced composite, as depicted in Figure 8b, would likely result in a lower density. To conduct a statistically significant analysis, several specimens from different areas should be cut and tested. Nonetheless, the measured average densities are, especially for type 1, significantly higher than the maximum relative density of 92% realized for the single-fiber based fabrics presented in [17].

### 2.3. Mechanical Characterization

In order to investigate which material performs better under mechanical stress, KLST-type specimens were cut according to DIN EN ISO 179-1:2000 from each of the composites produced using EDM and further subjected to monotonic and cyclic three-point bending tests. A tensile testing machine equipped with a 5 kN load cell (TIRAtest 2820, Nr. R050/01 from TIRA GmbH, integrated with OPTO ENGINEERING-TC4 M004-C) was utilized for all mechanical tests described below. The setup is shown in Figure 11. Here, the camera objective, the test samples, and the stamp of the testing machine can be seen. For evaluation, the testing time, absolute force, machine displacement, and video images were captured at room temperature.

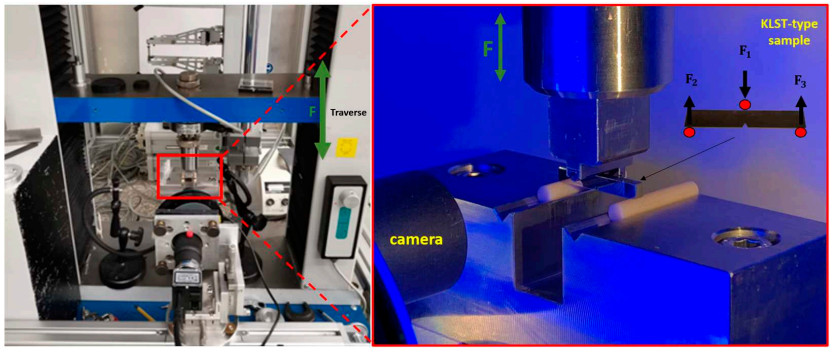


**Figure 11.** TIRAtest 2820, Nr. R050/01 setup with KLST-type $W_f/W$ samples for three-point bending tests and cyclic loading tests.

#### 2.3.1. Monotonic Three-Point Bending Tests with KLST-Type Samples

In Figure 12, a representative crack behaviour of one of the samples is depicted, starting unloaded in (a) to fully broken in (d).

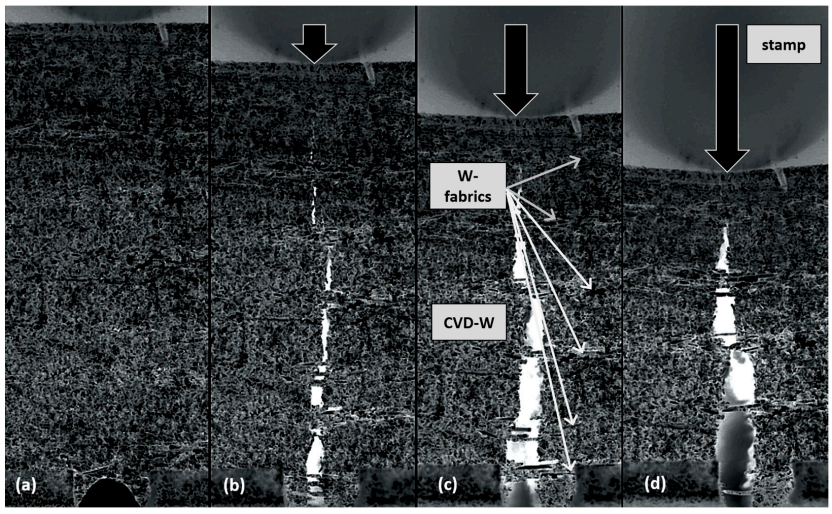


**Figure 12.** Crack behaviour during three-point bending test from (**a**) unloaded state, (**b**) initial cracking, (**c**) clear cracking, and (**d**) almost full broken sample.

In Figure 13, the obtained force–displacement curves of all samples are presented and compared to pure, field-assisted, sintered W-powders, sintered at 1900 °C and 50 MPa with a 93% rel. density.

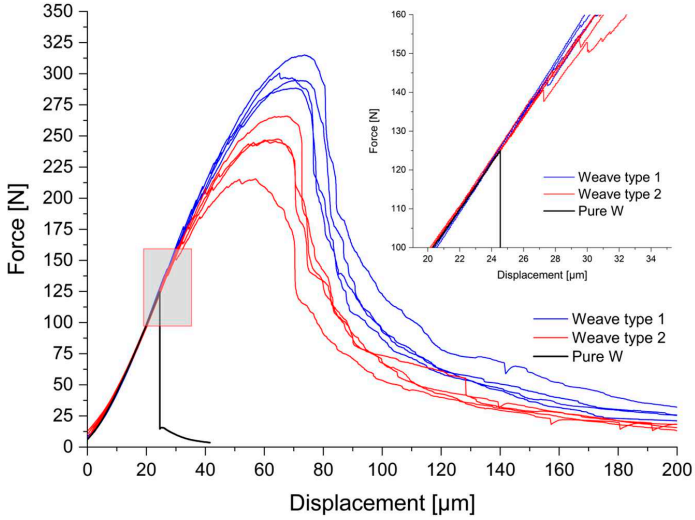


**Figure 13.** Force over displacement curves of KLST-type samples of fabric type 1, type 2, and sintered W-sample (Pure W powders 5 µm, field-assisted sintering at 1900 °C, 50 MPa, 93% rel. density).

The results presented in Figure 13 and the accompanying fracture images in Figure 12 provide convincing evidence for the theoretical pseudo-ductile mechanisms outlined in Figure 1. In particular, the crack bridging mechanism can be clearly observed on the macroscopic scale. In order to further examine the microstructure of the broken composites, Figure 14 presents two SEM-images: the left image (a) illustrates the crack bridging mechanism in detail. The right image (b) highlights, that some fibers display ductile necking (marked in green), while others exhibit brittle fracture (marked in red).

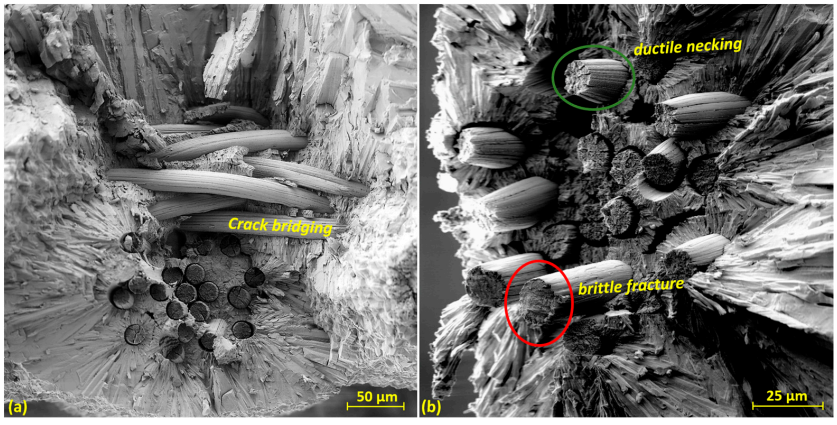


**Figure 14.** Representative fracture images of type 2 for both composites, images taken with SEM Carl Zeiss LEO DSM 982. (**a**) illustrates crack bridging, and (**b**) depicts ductile necking in the green-marked region and brittle fracture in the red-marked region.

Although not all fibers exhibit ductile necking, the load–displacement curves in Figure 13 do not show abrupt failure. At this point, it has to be highlighted again that the composites were produced without an yttria interface, which would decrease the fiber matrix adhesion and should further improve the performance of the material and, e.g., the necking behavior [5–7]. It appears that as the number of fibers within the matrix increases, so does the likelihood of contributing to the mechanisms of pseudo-ductile materials. As a result, the reproducibility of mechanical properties improves with a higher number of W-fibers in the CVD-W matrix, but this hypothesis needs to be confirmed through further experiments. The produced composite type 1 demonstrates a superior performance with a significantly higher mean maximum load capacity of 299.74 N compared to 243.96 N for type 2. The reproducibility of the load–displacement curves is also superior for type 1, which can be attributed to the more homogeneous fabric distribution as observed in Figures 9 and 10. Upon examination of the enlarged area in the upper right corner of Figure 13, initial cracking can be observed in the same range as for pure, sintered tungsten without fiber reinforcement. However, instead of a brittle fracture behavior as seen for the sintered sample, both of the composites show a stable crack growth, resulting in an increase of the maximum load capacity.

#### 2.3.2. Cyclic Tests with KLST-Type Samples

In order to evaluate the KLST-type specimen under cyclic loading, the average maximum load was firstly measured for each composite type. Subsequently, 10,000 load cycles were applied between 50–90% of the avg. respective maximum load, with a frequency of 1 Hz, on each material. Figure 15 shows a representative overview for composite type 1 before (a) and after (b) cyclic loading, highlighting the crack growth in yellow. It can be seen, that the specimen remained consistent without the occurrence of complete failure after the experiment.

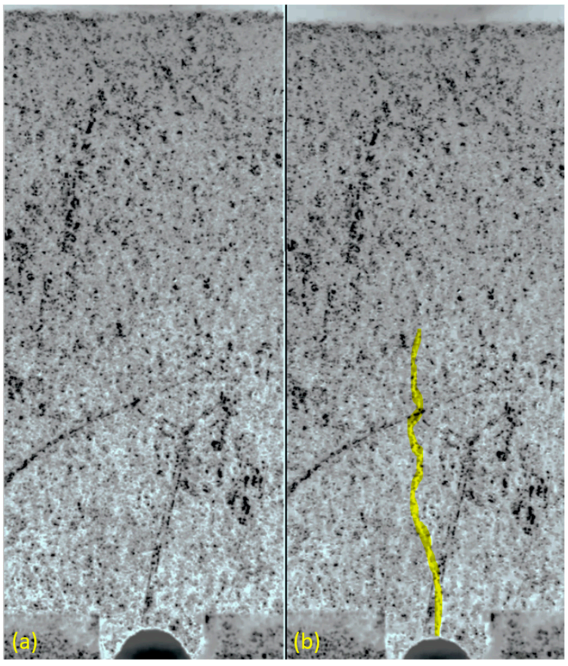


**Figure 15.** Cyclic mechanical loading tests of composite type 1 before (**a**) and after (**b**) 10,000 load cycles between 50–90% of the rel. max. load capacity. The crack growth is highlighted in yellow.

However, due to the high number of cycles and corresponding high amount of data, only the beginning and the end of cyclic loading were captured in images. During the experimental investigation, it was observed that the cracks in the matrix responded to changes in the load with a slight opening and closing behavior. This cyclic loading resulted in the propagation of cracks, which became more pronounced with an increasing number of loading cycles, which leads to the question, at which number of cycles the material would break completely.

2.3.3. Prediction of the Fatigue Behavior

It can be seen in Figure 16 that the displacement over the total number of cycles for the 10,000 load cycles is not constant, which means that the sample shows signs of fatigue over time.

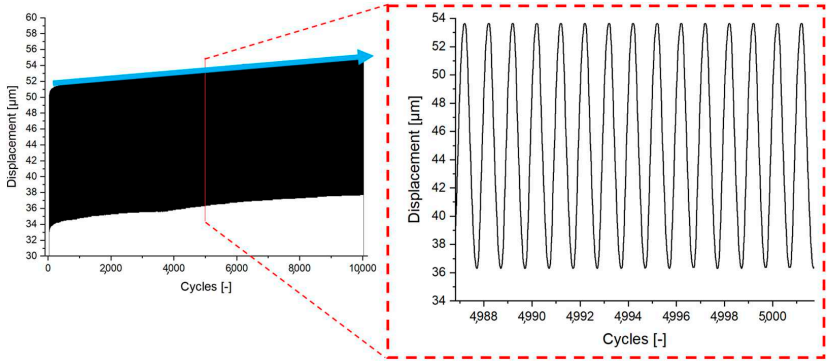


**Figure 16.** Cyclic loading tests between 50–90% of the avg. max. load. Representative overview for both composites.

In the literature, fatigue behavior prediction is often achieved through the measurement of the crack length over a given number of cycles [38,39]. As mentioned above, the amount of data for such a high number of cycles does not allow the evaluation with this approach. Therefore, the goal in this work is to extrapolate the displacement movement over the total number of cycles instead. In order to demonstrate that the trend can be extrapolated up to the point of critical displacement, which was measured first hand by monotonic three-point bending tests, the average critical displacement value of the better performing composite type 1 was initially determined with the data presented in Figure 13 and averaged to a value of 72.11 $\pm$ 1.95 µm. Following that, the upper boundary of the mechanical load cycles was further increased from 90% to 95% (150–285 N) in order to reduce the necessary number of cycles to break the samples. This cyclic load range was applied at a frequency of 1 Hz until the material experienced complete failure. Figure 17 shows the corresponding displacement in micrometers over the time in seconds. The red marks indicate the maximum peaks of the sinusoids, and the black line shows the average critical displacement, which was determined from the fully broken samples in initial tests. It is evident that once the predicted critical displacement of the sample is exceeded, a complete failure of the sample occurs in the next cycle. This supports the assumption, that cyclic loading tests and classic three-point bending tests have matching critical displacement limits, and therefore the fatigue behavior over time can be extrapolated for cyclic loading. To predict the fatigue behavior, a linear regression was performed on the entire dataset. In Figure 18, the red marks represent the displacement maxima of each sinusoid in Figure 17, plotted against the number of cycles. The fit of the blue trendline describes the trend with an adjusted R-square of 85.99%.

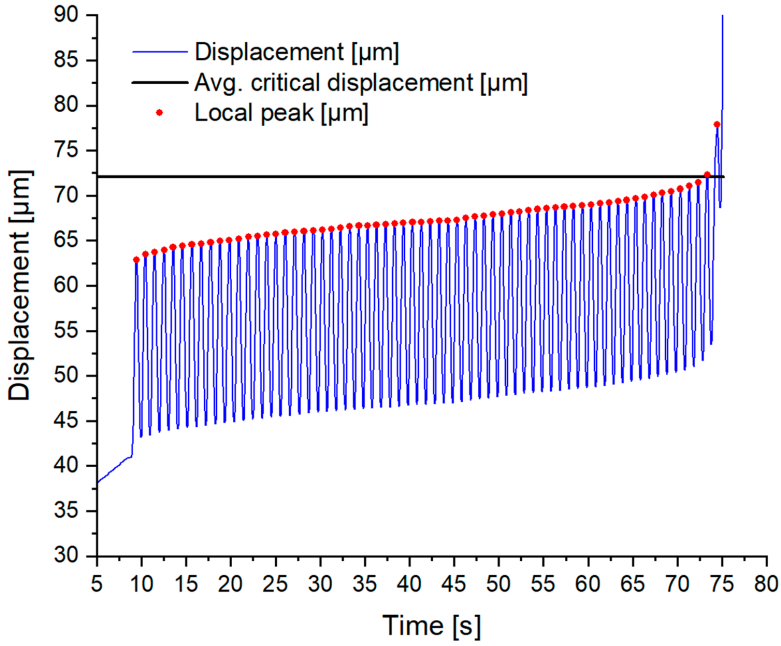


**Figure 17.** Cyclic loading tests between 50–95% of the avg. max. load of composite type 1.

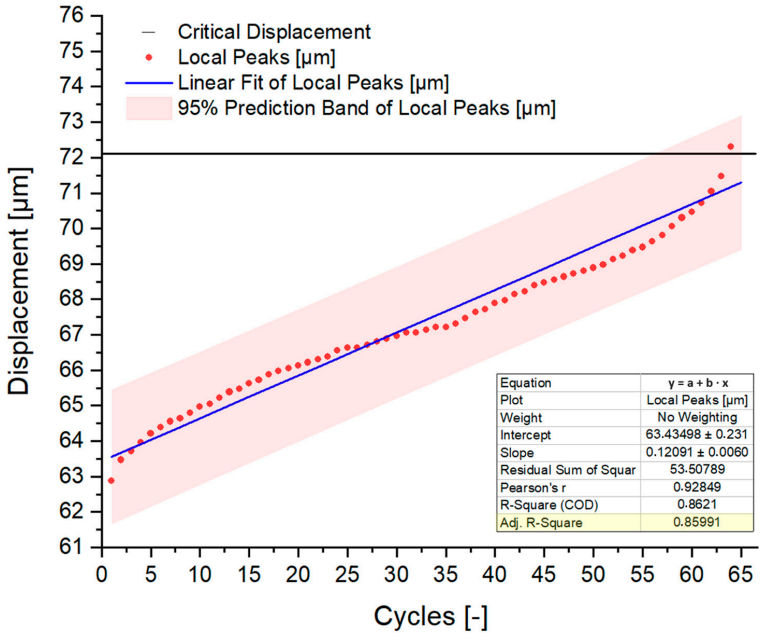


**Figure 18.** Maxima of each sinusoid displacement [µm] over the total number of mechanical load cycles [−]. The red dots show each maximum, the blue line shows the trendline of a linear regression.

Therefore, it seems, that a simple linear regression can be used to make initial predictions of the number of mechanical load cycles for each load range. Using the same critical

displacement limit and the data in Figure 16 with the specimen that had been tested for 10,000 cycles between 50–90% of the rel. maximum load, a linear regression suggests that the cycling load could potentially be increased to approx. 58,000 cycles for this load range.

In order to improve the accuracy of the fatigue behavior predictions, the function can be split into two parts. The data suggest, that as the displacement trend approaches the point of critical displacement, the linear trend function shifts towards an exponential growth function. By separating the data into ranges below and above 96% of the relative critical displacement value, the coefficient of determination (adjusted R-square fit) shows that below 96%, the data fits 99.03% to that of a linear function, and above 96%, an exponential growth function fits with 98.25% to the dataset. This behavior is illustrated in Figure 19. Therefore, the simple linear regression can be further improved if needed.

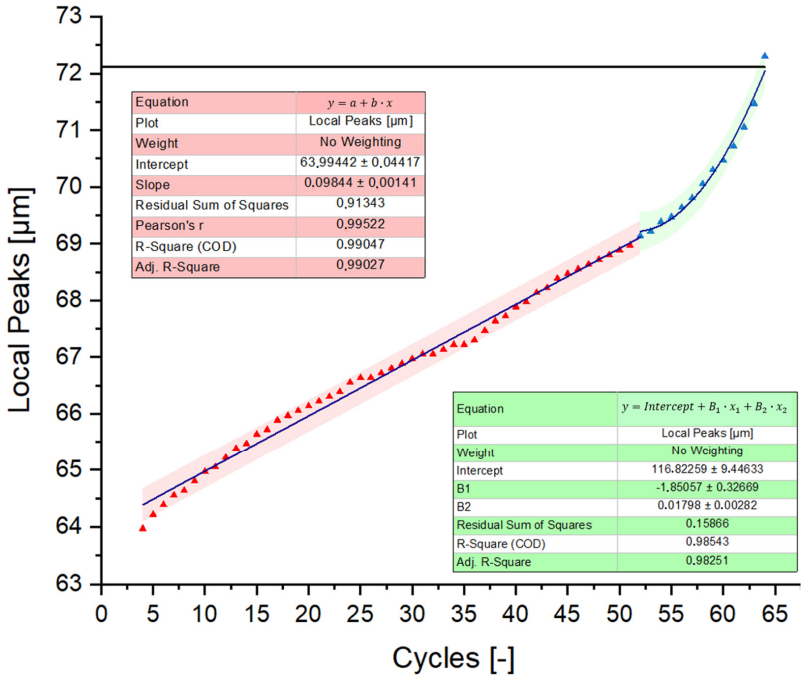


**Figure 19.** Split function of the displacement [µm] over total numbers of cycles [−]. The green marked area shows the values below 96% of the critical displacement value as a linear trend, and the red marked area describes the values above 96% as an exponential growth.

## 3. Conclusions and Outlook

The results show that the usage of yarn-based fabrics for CVD stacking are not just increasing the fiber volume fractions and densities of $W_f/W$ composites, but also increasing the reproducibility compared to the results presented in [17] for 150 µm single fiber-based fabrics. In Table 1, the material properties of each composite material produced are shown in an overview. The improvement can be explained with a significant increase of the total number of fibers per volume unit (one yarn has 23 fibers with a total diameter of approx. 190 µm), an improved processability, and a more homogeneous fiber distribution within the CVD-W matrix. This applies in particular for type 1, where the layer spacing is lower due to the reduced thickness of the weft material. Therefore, the usage of W-yarns as a warp material in combination with single weft fiber is a promising combination for the scale-up of $W_f/W$.

**Table 1.** Comparison table.

| Aspect | Type 1 | Type 2 |
|---|---|---|
| Weft material | Yarn R.B. 16 + 7 | Yarn R.B. 16 + 7 |
| Warp material | 50 µm filament | Yarn R.B. 16 + 7 |
| Avg. relative density | 97.14% | 96.59% |
| Fiber volume fraction | 14–17% | 7–10% |
| Processing Multilayer | very good | macroscopic gaps |
| Avg. max. load (KLST-type samples) | 299.74 N | 243.96 N |
| 10,000 cycles between 50–90% of rel. max. load | Sample intact—prediction possible | Sample intact—prediction not possible |
| Reproducibility | Very good | OK |

It should be emphasized that the application of an interface should further reduce the fiber–matrix adhesion and enhance the pseudo-ductile mechanisms such as the "pull-out" effect. The presented method to predict the fatigue behavior under cyclic mechanical loading tests might also pose an option to predict the lifetime under different stress conditions, such as thermal cyclic loading. However, the developed method needs to be further validated and investigated on further test samples.

Future efforts will focus on developing a more efficient manufacturing process that allows for the same or better material properties at significantly lower production costs and times. Alternative production approaches such as the combination of the field-assisted sintering technology with the CVD process or the infiltration of stacked fabrics (CVI) are currently under investigation and will be presented in the future.

**Author Contributions:** Conceptualization, A.L., J.W.C., M.T. and H.G.; Methodology, A.L., J.W.C., D.S., Y.M., J.R. and A.T.; Software, L.R. and H.G.; Validation, J.W.C. and J.R.; Formal analysis, A.L., T.H., L.R. and B.G.; Investigation, A.L., D.S., L.R. and A.T.; Data curation, J.W.C., Y.M., B.G. and J.G.-J.; Writing—original draft, A.L.; Writing—review & editing, J.W.C., J.R., L.R., H.G., C.L., K.T.-B. and J.G.-J.; Visualization, A.L.; Supervision, J.W.C., C.L., K.T.-B. and J.G.-J.; Project administration, C.L. All authors have read and agreed to the published version of the manuscript.

**Funding:** This work has been funded by the European Union via the Euratom Research and Training Programme (Grant Agreement No. 101052200—EUROfusion).

**Data Availability Statement:** Please contact the corresponding authors for further information.

**Acknowledgments:** This work has been carried out within the framework of the EUROfusion Consortium, funded by the European Union via the Euratom Research and Training Programme (Grant Agreement No. 101052200—EUROfusion). Views and opinions expressed are, however, those of the author(s) only and do not necessarily reflect those of the European Union or the European Commission. Neither the European Union nor the European Commission can be held responsible for them.

**Conflicts of Interest:** The authors declare no conflict of interest.

## References

1. Pitts, R.; Carpentier, S.; Escourbiac, F.; Hirai, T.; Komarov, V.; Lisgo, S.; Kukushkin, A.; Loarte, A.; Merola, M.; Naik, A.S.; et al. A full tungsten divertor for ITER: Physics issues and design status. *J. Nucl. Mater.* **2013**, *438*, S48–S56. [CrossRef]
2. Linsmeier, C.; Rieth, M.; Aktaa, J.; Chikada, T.; Hoffmann, A.; Houben, A.; Kurishita, H.; Jin, X.; Li, M.; Litnovsky, A.; et al. Development of advanced high heat flux and plasma-facing materials. *Nucl. Fusion* **2017**, *57*, 092007. [CrossRef]
3. Philipps, V. Tungsten as material for plasma-facing components in fusion devices. *J. Nucl. Mater.* **2011**, *415*, S2–S9. [CrossRef]
4. Coenen, J.W. Fusion Materials Development at Forschungszentrum Jülich. *Adv. Eng. Mater.* **2020**, *22*, 1901376. [CrossRef]
5. Evans, A.; Zok, F.; Davis, J. The Role of Interfaces in Fiber-Reinforced Brittle Matrix Composites. *Compos. Sci. Technol.* **1991**, *42*, 3–24. [CrossRef]

6. Mao, Y.; Coenen, J.; Riesch, J.; Sistla, S.; Almanstötter, J.; Jasper, B.; Terra, A.; Höschen, T.; Gietl, H.; Linsmeier, C.; et al. Influence of the interface strength on the mechanical properties of discontinuous tungsten fiber-reinforced tungsten composites produced by field assisted sintering technology. *Compos. Part A Appl. Sci. Manuf.* **2018**, *107*, 342–353. [CrossRef]
7. Shu, R.; Mao, Y.; Coenen, J.W.; Terra, A.; Liu, C.; Schönen, S.; Riesch, J.; Linsmeier, C.; Broeckmann, C. Interface and mechanical properties of the single-layer long fiber reinforced Wf/W composites fabricated via field assisted sintering technology. *Mater. Sci. Eng. A* **2022**, *857*, 144098. [CrossRef]
8. Gandhi, C.; Ashby, M. Fracture-Mechanism Maps for Materials Which Cleave—Fcc, Bcc and Hcp Metals and Ceramics. *Acta Metall. Mater.* **1979**, *27*, 1565–1602. [CrossRef]
9. Gietl, H.; Olbrich, S.; Riesch, J.; Holzner, G.; Höschen, T.; Coenen, J.; Neu, R. Estimation of the fracture toughness of tungsten fibre-reinforced tungsten composites. *Eng. Fract. Mech.* **2020**, *232*, 107011. [CrossRef]
10. Mao, Y.; Coenen, J.W.; Riesch, J.; Sistla, S.K.; Almanstötter, J.; Reiser, J.; Terra, A.; Chen, C.; Wu, Y.; Raumann, L.; et al. Fracture behavior of random distributed short tungsten fiber-reinforced tungsten composites. *Nucl. Fusion* **2019**, *59*, 086034. [CrossRef]
11. Zinkle, S.; Ghoniem, N. Operating temperature windows for fusion reactor structural materials. *Fusion Eng. Des.* **2000**, *51–52*, 55–71. [CrossRef]
12. Zhang, L.; Jiang, Y.; Fang, Q.; Zhang, T.; Wang, X.; Liu, C. Toughness and microstructure of tungsten fibre net-reinforced tungsten composite produced by spark plasma sintering. *Mater. Sci. Eng. A* **2016**, *659*, 29–36. [CrossRef]
13. Zhang, L.; Jiang, Y.; Fang, Q.; Xie, Z.; Miao, S.; Zeng, L.; Zhang, T.; Wang, X.; Liu, C. Microstructure and mechanical properties of tungsten composite reinforced by fibre network. *Front. Mater. Sci.* **2017**, *11*, 190–196. [CrossRef]
14. Zhang, L.; Jiang, Y.; Fang, Q.; Liu, R.; Xie, Z.; Zhang, T.; Wang, X.; Liu, C. Comparative Investigation of Tungsten Fibre Nets Reinforced Tungsten Composite Fabricated by Three Different Methods. *Metals* **2017**, *7*, 249. [CrossRef]
15. Mao, Y.; Coenen, J.W.; Riesch, J.; Sistla, S.; Chen, C.; Wu, Y.; Raumann, L.; Neu, R.; Linsmeier, C.; Broeckmann, C. Spark Plasma Sintering Produced W-Fiber-Reinforced Tungsten Composites. In *Spark Plasma Sintering of Materials: Advances in Processing and Applications*; Springer Nature: Cham, Switzerland, 2019; pp. 239–261. [CrossRef]
16. Treitz, M. Development of Production Routines for Fibre Reinforced Metal Matrix Composites. Master's Thesis, University of Applied Sciences Munich, Munich, Germany, 2019.
17. Schwalenberg, D.; Coenen, J.W.; Riesch, J.; Hoeschen, T.; Mao, Y.; Lau, A.; Gietl, H.; Raumann, L.; Huber, P.; Linsmeier, C.; et al. Large-Scale Tungsten Fibre-Reinforced Tungsten and Its Mechanical Properties. *J. Nucl. Eng.* **2022**, *3*, 306–320. [CrossRef]
18. Zhao, S.X.; Liu, F.; Qin, S.G.; Song, J.P.; Luo, G.N. Preliminary Results of W Fiber Reinforced W (Wf/W) Composites Fabricated with Powder Metallurgy. *Fusion Sci. Technol.* **2013**, *64*, 225–229. [CrossRef]
19. Riesch, J.; Höschen, T.; Linsmeier, C.; Wurster, S.; You, J.-H. Enhanced toughness and stable crack propagation in a novel tungsten fibre-reinforced tungsten composite produced by chemical vapour infiltration. *Phys. Scr.* **2014**, *T159*, 014031. [CrossRef]
20. Riesch, J.; Han, Y.; Almanstötter, J.; Coenen, J.W.; Höschen, T.; Jasper, B.; Zhao, P.; Linsmeier, C.; Neu, R. Development of tungsten fibre-reinforced tungsten composites towards their use in DEMO—Potassium doped tungsten wire. *Phys. Scr.* **2016**, *T167*, 014006. [CrossRef]
21. Mao, Y.; Coenen, J.; Sistla, S.; Liu, C.; Terra, A.; Tan, X.; Riesch, J.; Hoeschen, T.; Wu, Y.; Broeckmann, C.; et al. Design of tungsten fiber-reinforced tungsten composites with porous matrix. *Mater. Sci. Eng. A* **2021**, *817*, 141361. [CrossRef]
22. Mao, Y.; Coenen, J.W.; Sistla, S.; Tan, X.; Riesch, J.; Raumann, L.; Schwalenberg, D.; Höschen, T.; Chen, C.; Wu, Y.; et al. Development of tungsten fiber-reinforced tungsten with a porous matrix. *Phys. Scr.* **2020**, *T171*, 014030. [CrossRef]
23. Terentyev, D.; Riesch, J.; Lebediev, S.; Bakaeva, A.; Coenen, J. Mechanical properties of as-fabricated and 2300 °C annealed tungsten wire tested up to 600 °C. *Int. J. Refract. Met. Hard Mater.* **2017**, *66*, 127–134. [CrossRef]
24. Zhao, P.; Riesch, J.; Höschen, T.; Almanstötter, J.; Balden, M.; Coenen, J.; Himml, R.; Pantleon, W.; von Toussaint, U.; Neu, R. Microstructure, mechanical behaviour and fracture of pure tungsten wire after different heat treatments. *Int. J. Refract. Met. Hard Mater.* **2017**, *68*, 29–40. [CrossRef]
25. Coenen, J.W.; Antusch, S.; Aumann, M.; Biel, W.; Du, J.; Engels, J.; Heuer, S.; Houben, A.; Hoeschen, T.; Jasper, B.; et al. Materials for DEMO and reactor applications—Boundary conditions and new concepts. *Phys. Scr.* **2015**, *T167*, 014002. [CrossRef]
26. Raumann, L.; Coenen, J.W.; Riesch, J.; Mao, Y.; Gietl, H.; Höschen, T.; Linsmeier, C.; Guillon, O. Modeling and validation of chemical vapor deposition of tungsten for tungsten fiber reinforced tungsten composites. *Surf. Coat. Technol.* **2019**, *381*, 124745. [CrossRef]
27. Gietl, H.; Riesch, J.; Coenen, J.; Höschen, T.; Neu, R. Production of tungsten-fibre reinforced tungsten composites by a novel continuous chemical vapour deposition process. *Fusion Eng. Des.* **2019**, *146*, 1426–1430. [CrossRef]
28. Raumann, L.; Coenen, J.; Riesch, J.; Mao, Y.; Schwalenberg, D.; Wegener, T.; Gietl, H.; Hoschen, T.; Linsmeier, C.; Guillon, O. Modeling and experimental validation of a W-f/W-fabrication by chemical vapor deposition and infiltration. *Nucl. Mater. Energy* **2021**, *28*, 101048. [CrossRef]
29. Raumann, L.; Coenen, J.; Riesch, J.; Mao, Y.; Schwalenberg, D.; Gietl, H.; Linsmeier, C.; Guillon, O. Improving the W Coating Uniformity by a COMSOL Model-Based CVD Parameter Study for Denser W-f/W Composites. *Metals* **2021**, *11*, 1089. [CrossRef]
30. You, J.; Visca, E.; Bachmann, C.; Barrett, T.; Crescenzi, F.; Fursdon, M.; Greuner, H.; Guilhem, D.; Languille, P.; Li, M.; et al. European DEMO divertor target: Operational requirements and material-design interface. *Nucl. Mater. Energy* **2016**, *9*, 171–176. [CrossRef]

31. Mao, Y.; Engels, J.; Houben, A.; Rasinski, M.; Steffens, J.; Terra, A.; Linsmeier, C.; Coenen, J. The influence of annealing on yttrium oxide thin film deposited by reactive magnetron sputtering: Process and microstructure. *Nucl. Mater. Energy* **2017**, *10*, 1–8. [CrossRef]
32. Garrison, L.; Katoh, Y.; Snead, L.; Byun, T.; Reiser, J.; Rieth, M. Irradiation effects in tungsten-copper laminate composite. *J. Nucl. Mater.* **2016**, *481*, 134–146. [CrossRef]
33. Coenen, J.; Berger, M.; Demkowicz, M.; Matveev, D.; Manhard, A.; Neu, R.; Riesch, J.; Unterberg, B.; Wirtz, M.; Linsmeier, C. Plasma-wall interaction of advanced materials. *Nucl. Mater. Energy* **2017**, *12*, 307–312. [CrossRef]
34. Palaniyappan, S.; Trautmann, M.; Mao, Y.; Riesch, J.; Gowda, P.; Rudolph, N.; Coenen, J.W.; Neu, R.; Wagner, G. Yttria-Coated Tungsten Fibers for Use in Tungsten Fiber-Reinforced Composites: A Comparative Study on PVD vs. CVD Routes. *Coatings* **2021**, *11*, 1128. [CrossRef]
35. Gietl, H.; von Muller, A.; Coenen, J.; Decius, M.; Ewert, D.; Hoschen, T.; Huber, P.; Milwich, M.; Riesch, J.; Neu, R. Textile pre-forms for tungsten fibre-reinforced composites. *J. Compos. Mater.* **2018**, *52*, 3875–3884. [CrossRef]
36. Coenen, J.W.; Huber, P.; Lau, A.; Raumann, L.; Schwalenberg, D.; Mao, Y.; Riesch, J.; Terra, A.; Linsmeier, C.; Neu, R. Tungsten fiber reinforced tungsten (Wf/W) using yarn based textile preforms. *Phys. Scr.* **2021**, *96*, 124063. [CrossRef]
37. Coenen, J.; Treitz, M.; Gietl, H.; Huber, P.; Hoeschen, T.; Raumann, L.; Schwalenberg, D.; Mao, Y.; Riesch, J.; Terra, A.; et al. The use of tungsten yarns in the production for W-f/W. *Phys. Scr.* **2020**, *T171*, 014061. [CrossRef]
38. Hertzberg, R.; Vinci, R.; Hertzberg, J. *Deformation and Fracture Mechanics of Engineering Materials*, 6th ed.; Wiley: Hoboken, NJ, USA, 2020.
39. Meyers, M.; Chawla, K. *Mechanical Behavior of Materials*, 2nd ed.; Cambridge University Press: Cambridge, UK; New York, NY, USA, 2009.

# 6 Publication 1 – Epilogue

The findings presented in Publication [1] highlight the exceptional efficiency of the optimized Batch-LPCVD process, which integrates the operational measures delineated in Chapter 4 and employs yarn-based textile fabrics as an innovative substitute to conventional textiles composed of individual W-filaments. This methodological advancement enables the fabrication of $W_f$/W composites with outstanding consistency in material properties and even predictable fatigue behavior under cyclic mechanical loading conditions at ambient temperatures. The results presented herein establish a unique reproducibility benchmark for W-based composites, underscoring their significant potential for prospective commercial applications, particularly in light of the superior performance of WFRCs under neutron-irradiated environments, as previously discussed in Sections 2.3 and 2.4.

Having successfully resolved the inconsistencies in material properties, the next major objective of this thesis is to advance the production of WFRCs toward industrial scalability while maintaining CVD as the primary consolidation method. However, achieving this goal introduces new significant obstacles, particularly in terms of manufacturing speed and cost-effectiveness – both critical factors for achieving commercial viability. A comprehensive examination of the existing Batch-LPCVD process, discussed in the following sections, elucidates the magnitude of these challenges and establishes a foundation for targeted improvements.

# 7 Limitations in Scaling the Batch-LPCVD Process

A comprehensive evaluation of the current Batch-LPCVD process has revealed several intrinsic limitations that constrain its scalability. These challenges fall into three main categories: production throughput, maintenance requirements, and deposition efficiency. Collectively, these factors pose substantial barriers to the efficient, large-scale production of $W_f$/W composites.

## 7.1 Production Throughput

The most significant technical constraint of the current Batch-LPCVD process is its low production throughput. Producing a single layer of $W_f$/W, as described in Publication [1], necessitates a process duration exceeding 15 hours. This timeframe includes approximately two hours for preliminary operations, two and a half hours to achieve chemical equilibrium within the reaction chamber, another two and a half hours to seal each textile layer via CVD, followed by approximately eight hours for rinsing, cooling, and reopening the chamber.

Although each step is crucial for maintaining product quality, the total processing time per layer significantly constrains the production throughput. For example, the large-scale samples comprising 25 $W_f$/W composite layers, as documented in reference [4], required a total production time of over three months. Possible adjustments to critical process parameters, such as increasing the reaction temperature or chamber pressure, could partially alleviate these constraints, as previously discussed in Chapter 3.4. Nonetheless, the prolonged heating and cooling phases remain as the dominant bottlenecks. Overcoming these time constraints is therefore crucial to the implementation of a scalable production method. However, this is not the sole factor impeding the scalability of the process.

## 7.2 Maintenance Intervals

In addition to throughput constraints, the current Batch-LPCVD process imposes considerable maintenance requirements that limit both scalability and economic viability. These maintenance issues are closely intertwined with throughput concerns, since frequent shutdowns negatively impact overall productivity. While certain issues, such as turbo pump clogging, have already been resolved to facilitate the production of samples presented in Publication [1], other critical components still necessitate regular maintenance or replacement. These components include pH meter electrodes, check valves for the sodium hydroxide supply, pressure sensors, mass flow controllers for process gases, specific piping sections, the gas scrubber circulation pump, and thermocouples.

Although these components generally do not pose immediate operational risks and typically require maintenance at extended intervals, their combined effects elevate overall costs and logistical demands. To enable large-scale WFRC production, it is essential to account for these components as spare parts in budget planning and to reassess their maintenance schedules with respect to process upscaling. The following sections highlight the two most critical maintenance-related challenges. These issues not only diminish production efficiency, but also represent significant obstacles to the broader scalability of the Batch-LPCVD method.

### 7.2.1 Preheating Pipes Clogging

One of the persistent challenges in scaling the Batch-LPCVD process is the frequent need to replace the preheating pipes, which are responsible for delivering reactive precursors, such as $WF_6$ and $H_2$, to the substrate. Preheating these precursors is critical for achieving uniform CVD-W deposition across the desired surface structures. However, this preheating step inadvertently causes the accumulation of W within the piping system, which progressively compromises pressure control and eventually leads to complete blockages. Current mitigation approaches primarily involve the periodic replacement of these pipes and increasing their diameter. However, such interventions alter the precursor flow conditions and thus influence the boundary layer dynamics, which ultimately affects the CVD-W deposition behavior, as illustrated in Figure 13 and further elaborated in reference [297]. Under industrial conditions, this issue becomes even more pronounced, as heightened process demands are likely to amplify maintenance requirements, thereby raising the associated efforts and costs. These challenges are further compounded by the maintenance of the scrubber tank, which introduces additional complexities and operational constraints.

### 7.2.2 Gas Scrubber Tank

Maintaining the gas scrubber tank represents another significant operational challenge of the Batch-LPCVD process, as it requires frequent interventions and labor-intensive procedures. The rapid accumulation of sodium fluoride, resulting from the substantial quantities of sodium hydroxide required to neutralize acidic gases, swiftly brings the tank to its solubility limit. This problem is intensified by extended process durations and larger product sizes. According to the process parameters and sample dimensions detailed in Publication [1], a maintenance cycle is required after every three batches. Each maintenance cycle entails the disassembly of the scrubber tank, the disposal of hazardous waste, and the replenishment of the tank with fresh water.

These procedures substantially disrupt production continuity and diminish operational efficiency. In addition, the handling and disposal of hazardous waste raise environmental and safety concerns. Addressing these issues is critical for developing a sustainable manufacturing route that is capable to meet the stringent requirements of advanced technologies, such as nuclear fusion. One key factor contributing to the high frequency of these maintenance cycles is the low deposition efficiency, which is briefly introduced in the following section.

### 7.3 Low Deposition Efficiency and Economical Aspects

Another notable economic limitation of the current Batch-LPCVD method is its inherently low deposition efficiency, illustrated by the considerable consumption of precursors like $WF_6$. The present process requires approximately 15 kilograms of $WF_6$ to produce one kilogram of $W_f/W$ composite. This discrepancy underscores the inefficiency of the procedure, as only a small fraction of the $WF_6$ contributes directly to forming the desired composite layers.

One potential solution to mitigate this issue could be the integration of a recycling loop to recover and reuse unreacted precursor material. However, implementing such a system is highly complex and requires a comprehensive evaluation as part of future research or through collaboration with industrial partners. Within the scope of this thesis, the focus is primarily placed on investigating alternative production strategies to address the critical technical challenges outlined in the previous sections, such as reducing production time and maintenance requirements. These strategies are anticipated to be the key to enhancing the scalability and economic feasibility of the process. The following section provides an overview of the approaches explored within the context of this work.

## 8 Upscaling Methods

In order to address the limitations identified in the Batch-LPCVD process, the following chapters examine three alternative production strategies. These approaches are designed to increase throughput, reduce maintenance requirements, enhance cost-effectiveness, and improve the overall material performance. Each strategy targets the specific constraints outlined in previous sections, with the ultimate goal of enabling industrial-scale feasibility.

1. ***Combining Chemical Vapor Deposition (CVD) and Spark Plasma Sintering (SPS)***
2. ***Continuous Chemical Vapor Deposition (Continuous CVD)***
3. ***Chemical Vapor Infiltration (CVI)***

The first strategy, introduced in the second publication of this dissertation and entitled "*Combining Chemical Vapor Deposition and Spark Plasma Sintering for the Production of Tungsten Fiber-Reinforced Tungsten (Hybrid-$W_f$/W)*", explores the integration of the Batch-LPCVD process with consolidation techniques commonly used in powder metallurgy. Its primary objective is to determine whether the multiple consolidation steps required by Batch-LPCVD can be reduced to a single step by integrating sintering methodologies into the established process chain outlined in Section 3 of this work. The following section revisits this publication, outlining its potential advantages and key findings.

ADVENGMAT
Vol. 26 – No. 20
October 2024

# ADVANCED ENGINEERING MATERIALS

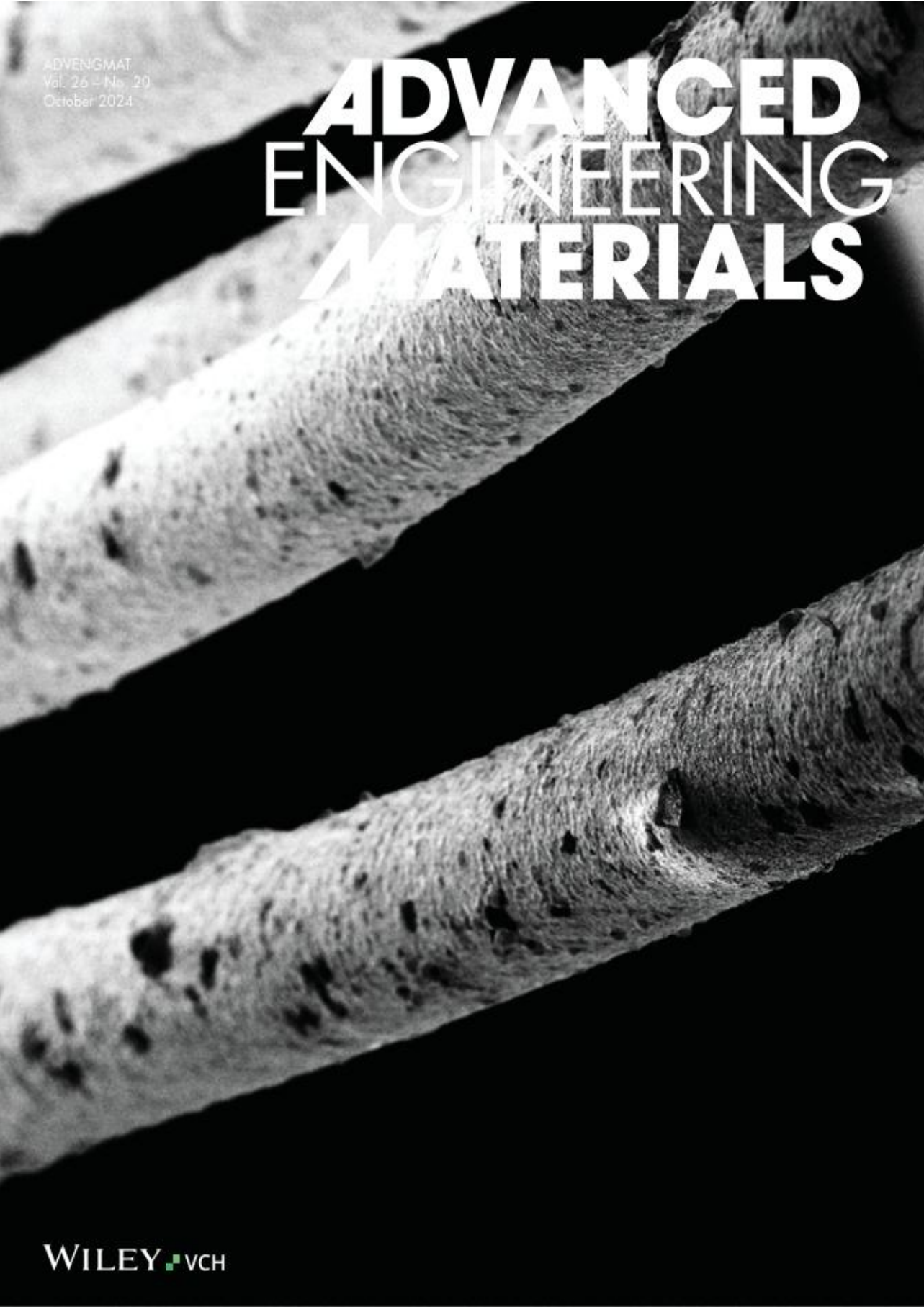

WILEY VCH

RESEARCH ARTICLE

ADVANCED ENGINEERING MATERIALS

www.aem-journal.com

# Combining Chemical Vapor Deposition and Spark Plasma Sintering for the Production of Tungsten Fiber-Reinforced Tungsten (Hybrid – $W_f$/W)

*Alexander Lau,* Yiran Mao, Rui Shu, Jan W. Coenen, Melina Poll, Christian Linsmeier, and Jesus Gonzalez-Julian*

**Successful upscaling of tungsten fiber-reinforced tungsten composites ($W_f$/W) on industrial level could represent an important milestone for future nuclear fusion reactors. The primary objective of these materials is to enhance the durability and operational lifespans of critical components. Developing mature manufacturing approaches remains a challenge, highlighting the need for innovative solutions. This study evaluates the feasibility of merging chemical vapor deposition (CVD) with spark plasma sintering (SPS) for producing such composites. This analysis indicates that combining CVD-W sealed tungsten fabrics with SPS requires additional manufacturing steps or the utilization of tungsten powders for effective sintering. The process is currently only suitable for simple textile structures utilizing single filaments, mitigating one of the main advantages of CVD. Configurations such as radially braided yarns are currently less compatible to the high stress levels during SPS. A key outcome of this work is the introduction of a thin secondary CVD-W interface into the composite design, substantially improving the stability of the yttria-interface and effectively shielding the W-fibers from potential matrix interactions. This innovation reduces issues such as carbon embrittlement and allows the potential integration of tungsten fibers into different matrix materials such as ceramics, broadening the potential application range of tungsten fiber-reinforcements.**

## 1. Introduction

Navigating the path toward a sustainable energy future, the meticulous selection of materials for the development and design of future nuclear fusion power plants stands out as a significant challenge.[1–9] In this context, the pivotal first wall armor and divertor components within a fusion reactor confront harsh conditions, encompassing elevated temperatures, intense neutron radiation, and erosive plasma interactions. In recognition of these rigorous demands, the research spotlight turned toward tungsten-based components, considering them as promising solutions.[10,11] However, the intrinsic brittleness of pure tungsten introduces vulnerability, as fractures may manifest below the threshold of ductile–brittle transition temperature,[12] thereby engendering apprehensions of potential structural failure. In order to overcome this hurdle, investigations are currently underway into tungsten fiber-reinforced tungsten ($W_f$/W) composites as a viable solution. This approach entails the integration of potassium-doped tungsten filaments, boasting elevated recrystallization temperatures and ductility at room temperature, into a tungsten matrix and enduring the resistance in face of neutron irradiation.[2,12–14] The interface between these components comprises an oxide-ceramic material, such as yttria, strategically engineered to reduce the fiber–matrix adhesion and working as a

A. Lau, Y. Mao, R. Shu, J. W. Coenen, C. Linsmeier
Institut für Energie- und Klimaforschung – Plasmaphysik
Forschungszentrum Jülich GmbH
52428 Jülich, Germany
E-mail: a.lau@fz-juelich.de

A. Lau, J. Gonzalez-Julian
Department of Ceramics
RWTH Aachen University
52074 Aachen, Germany

The ORCID identification number(s) for the author(s) of this article can be found under https://doi.org/10.1002/adem.202301929.



DOI: 10.1002/adem.202301929

R. Shu
Institute for Materials Applications in Mechanical Engineering
RWTH Aachen University
52062 Aachen, Germany

J. W. Coenen
Department of Engineering Physics
University of Wisconsin-Madison
Madison, WI 53706, USA

M. Poll
Institut für Energie- und Klimaforschung – Werkstoffsynthese und Herstellungsverfahren
Forschungszentrum Jülich GmbH
52428 Jülich, Germany

predetermined fracture point. This design element facilitates the controlled transfer of mechanical loads to the resilient tungsten fibers, thereby enhancing the overall structural integrity in fusion related environments.[11,14–19] The construction of the tungsten matrix can be achieved through two distinct methodologies: The first involves the chemical reaction between tungsten hexafluoride and hydrogen, culminating in the relatively stress-free chemical vapor deposition (CVD). CVD engenders a refined crystal structure and elevates the recrystallization temperature of the matrix.[20–23] As a result, this technique provides enhanced resilience against thermal shocks, amplifies material density, and results in a significant improvement of the composite's performance. Alternatively, the matrix can be fabricated via powder metallurgical procedures, with a specific emphasis on the utilization of spark plasma sintering (SPS) techniques. The endeavor to scale up the powder metallurgical method presently provides a more attainable, cost-efficient, and expeditious avenue. More information can be found in other studies.[24–31] While these methods have traditionally been explored separately, our study evaluates the combination of these techniques, aiming to uncover potential benefits.

## 2. Theoretical Background

The concept of combining CVD with SPS originates from the intention to reduce the substantial manufacturing costs and extended production timelines that are currently associated with the fabrication of layered CVD-based composite materials, as illustrated in **Figure 1**.

Achieving a uniform CVD-W seal demands a precisely tailored setup, which is schematically depicted in **Figure 2**. This setup

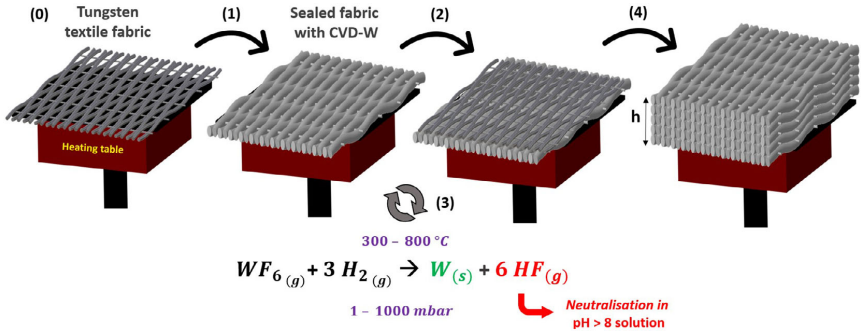


**Figure 1.** Batch CVD process: 0) positioning of flat textile fabric on the heat source, 1) sealing the fabric with CVD-W, 2) positioning of the subsequent layer, 3) repeat 1 and 2) to desired component thickness h, 4) removal of final component.

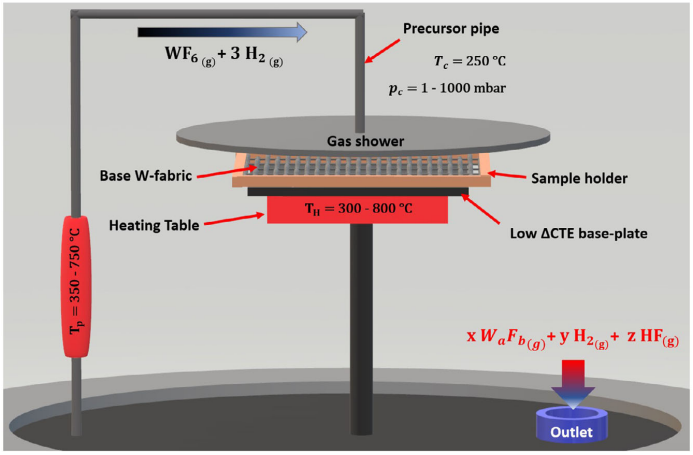


**Figure 2.** Schematic overview of a CVD reaction chamber: Precursors flow through a preheating system, reacting in a heterogeneous reaction on flattened tungsten fabrics, resulting in a homogeneous W-sealing. $T_C$ = Ambient temperature reaction chamber; $p_c$ = Total pressure reaction chamber; $T_H$ = Temperature heat source; $T_p$ = Temperature preheater; $x$, $y$, $z$, $a$, $b$ = Stoichiometric coefficients.

 

encompasses defined preheating conditions, volume flow adjustments calibrated to fabric size, controlled precursor volume flow ratios, pipe diameters leading to preferred laminar flow conditions, and well-defined retention times for the precursors on the reaction surface. Additionally, a base plate, strategically positioned between the heat source and the substrate, is required. This plate should have a minimal differential in the coefficient of thermal expansion (ΔCTE) compared to the substrate, ensuring homogeneous heat transfer. Furthermore, the synergy of the gas shower dimensions, specific adhesion surfaces, and distances to the reaction surface significantly contribute to the homogeneity of the tungsten films and sealings, which can be applied with the current configuration of the CVD machine in Figure 2. The layer thickness achievable with this setup can be varied approximately from 0.3 to 3500 $\mu m\,h^{-1}$, depending on the selected process parameters. The heterogeneous reaction between the precursors is primarily used within a low-pressure regime spanning from 1 to 1000 mbar, in conjunction with elevated temperatures ranging from 300 to 800 °C. An incremental increase in parameters, such as pressure or temperature, could trigger a transition toward a homogeneous reaction type, which is not desirable for the intended deposition in this context.

Comprehensive insights into reaction kinetics, crystal growth modelling, and the impact of the textile fabric dimensions on the composite's properties are documented in refs. [32–35].

Recent advancements in the geometric scaling of $W_f/W$ composites have been realized,[19] particularly in understanding size-related effects. Efforts have also been concentrated on improving the consistency of the mechanical properties, allowing for more accurate predictions of material behavior under various load conditions. A key development in this area is the incorporation of radially braided yarns into $W_f/W$ production, significantly boosting the reproducibility of layered CVD-based $W_f/W$ to align with industrial standards. A detailed exploration of this significant advancement can be found in refs. [16,36,37]. However, the existing process still follows the sequential approach introduced in Figure 1. Each layer necessitates careful opening of the reaction chamber, followed by extensive cleaning and replacement of worn parts before starting the next batch. Additionally, prolonged heating and cooling periods serve two purposes: promoting chemical stability during heating and reducing the risk of oxidation during cooling, which is maintained below 200 °C. This demanding production process is a primary barrier to achieving an industrial scale of $W_f/W$ composites via CVD. Upscaling the setup depicted in Figure 2 still carries the potential to represent a mature production method, as long as the sealing process is limited to a single deposition batch.

This could be achieved, if many single layers of CVD-sealed $W_f/W$ are further manufactured via SPS, a concept visually represented in **Figure 3**.

SPS is usually characterized by the application of a pulsed direct current (DC) and uniaxial pressure to facilitate the sintering of powder compacts. The sample dimensions are proportional to the machine size, which showcases a robust scalability. The process' uniqueness lies in its ability to achieve rapid densification at lower temperatures and shorter dwell times compared to traditional sintering methods.[38–40] The electrical field reduces the energy barrier for atomic diffusion across the particle boundaries and does not only facilitate atomic transport, but also interacts with defects and interfaces, influencing grain boundary migration and sintering kinetics. This interaction leads to the suppression of grain coarsening and the promotion of finer grain structures.[41,42] In the context of SPS – $W_f/W$ fabrication, the integration of additional graphite foil serves as a strategic approach to enable the removal of the composite after sintering. Nonetheless, the presence of carbon raises concerns regarding carbon embrittlement: Even trace amounts of carbon, measured in parts per million (ppm), can adversely affect the properties of tungsten fibers, as detailed in ref. [43]. The search for cost-efficient alternatives to graphite or CFC still remains

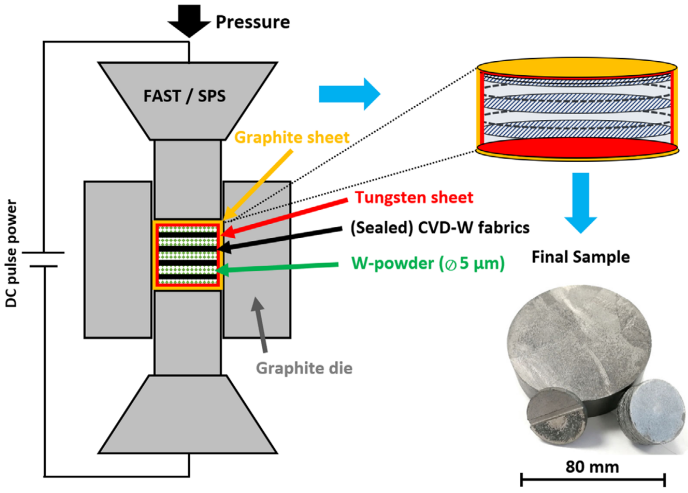


**Figure 3.** Schematic representation illustrating cyclic process of SPS.

difficult, as these materials must be electrically conductive and require a high thermal stability. The current method to prevent fiber embrittlement is to use thin tungsten sheets: These act as a protective barrier and ensure that the carbon interactions take place with the sheets and not with the fibers themselves.

By deflecting these interactions, the structural integrity and performance of the fibers are maintained, ensuring their quality and functionality. Drawing on insights from refs. [44–56], the inclusion of CVD-W could further improve the stability of the composite during sintering. This approach could simplify upscaling by replacing the need for W-sheets and providing more robust protection for the fibers and the ceramic interface, which currently exhibits instabilities during SPS, as discussed by Shu et al. in.[57] The potential benefits of incorporating CVD-W into composite design are further explored in Sections 4.4 and 4.5.

## 3. Experimental Section

The initial components or base discs used in this study were composed of two distinct single layers, one made of yarn-based fabrics and a second of 150 µm single fiber-based fabrics. The structures are illustrated in **Figure 4**. In order to attain the depicted structures, each fabric type was initially coated with a thin yttria interface using magnetron sputtering, achieving a thickness ranging from 1 to 2.5 µm. The yttria coating process used similar parameters to those outlined by Mao et al.[30]

Following the yttria coating, both fabric types were completely sealed using CVD. The CVD parameters closely align with those in ref. [16]: $T_H = 540\,°C$, $p_c = 100$ mbar, volume flow ratio $H_2$: $WF_6 = 12.5$: 1 for 180 min. The detailed process parameters are provided in the attachments of this work. It is important to note that adjustments may be necessary for larger scales or different sample sizes. The base discs, made of single or two layers of $W_f$/W, were then precision-cut using abrasive water cutting into dimensions suitable for the molds of the SPS device, as illustrated in **Figure 5**.

The cut fabrics were then layered and sintered using SPS to form a consolidated composite material in various configurations, including: stacking sealed single layers of $W_f$/W without W-powders, two CVD-sealed layers without powders, and single layers with W-powders (average particle diameter = 5 µm). Each approach used sintering parameters of 1800 °C for 5 min at pressures of 50 MPa, according to the parameters used by Shu et al. in.[57] As shown in **Figure 6**, the surface area of each disc varied based on the fabric's orientation during CVD, either toward the flat base plate or the surrounding environment/gas shower

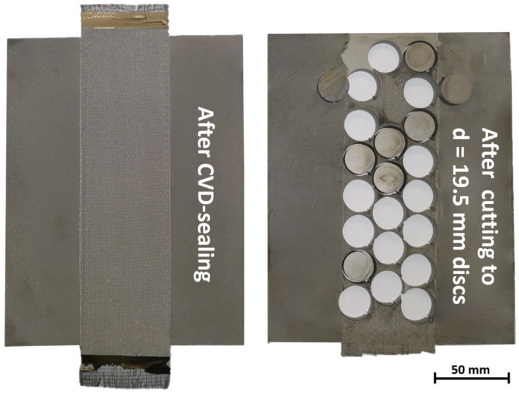


**Figure 5.** Tungsten fabrics embedded in a CVD-W matrix (left), cut into discs with a diameter of $d = 1.95$ cm for stacking via SPS process (right).

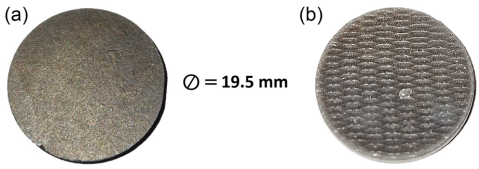


**Figure 6.** Tungsten fabrics, embedded in a CVD-W matrix and cut into discs that fit into the graphite containers of the SPS device: a) A flat surface, which had direct contact to a W base-plate during CVD, and b) a rough surface, which faced the environment/gas shower.

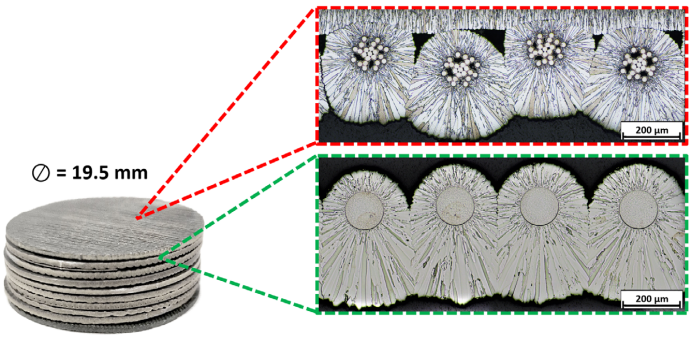


**Figure 4.** Single-layer CVD $W_f$/W before SPS. The red marked image shows the microstructure of a sealed yarn-based fabric and the green marked image sealed 150 µm single fiber-based fabrics.

 

(Figure 2, Supporting Information). To minimize potential gaps within each layer, the stacking procedure ensured that flat and rough surfaces were aligned (a-a, b-b).

Postsintering, each sample was cut using electrical discharge machining (EDM) and subsequently examined under a microscope after grinding, polishing, and edging of the surface.

## 4. Results

### 4.1. Single-Layer Stacking

Direct stacking of individually sealed $W_f$/W fabrics could eliminate the need for additional tungsten powders and also significantly reduce production time and costs while maintaining fiber volume fractions similar to those in conventional CVD stacking. However, as demonstrated in **Figure 7**, applying high pressures during SPS leads to the complete disintegration of each individual layer of $W_f$/W. This finding suggests that this method, whether using yarn-based or single fiber-based fabrics, lacks practical utility for future applications.

### 4.2. Double-Layer Stacking

Based on prior research[16,19,36,58] and practical observations, it is evident that enlarging the geometric dimensions of $W_f$/W substantially improves its mechanical resilience. This finding has led to the development of a method involving the sealing of two $W_f$/W layers via CVD, followed by SPS stacking. This approach is envisioned as a potential compromise, offering the advantage of being adaptable to any base fabric type. This flexibility not only broadens design possibilities but could still significantly reduce production time and costs for large components. Additionally, this technique is capable of achieving a fiber volume fraction comparable to conventional CVD stacking, as demonstrated in Figure 1.

**Figure 8** presents two macroscopic images before and after SPS processing, illustrating that a consolidated material can be produced utilizing this technique.

However, a detailed analysis of the microstructure using scanning electron microscope (SEM) imaging techniques reveals a direct correlation between matrix cracking and the orientation of the W-fabrics during CVD. This correlation, initially introduced in Figure 6, becomes more apparent when examining the variations in microstructure due to the initial surface roughness, as depicted separately in **Figure 9** and **10**. The transition area between two sintered discs with flat surfaces leads to a matrix without cracking. The blue highlighted section in Figure 9 emphasizes a flat transition area, which results in a more homogeneous mechanical stress distribution during SPS, thus mitigating cracking within the CVD-W matrix.

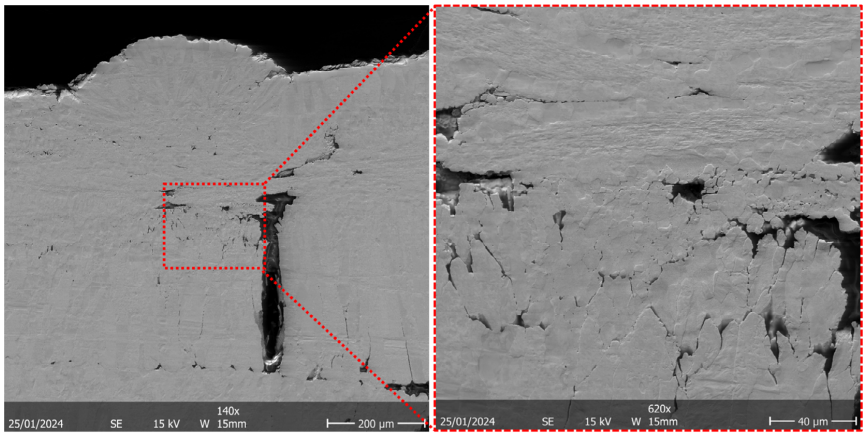


**Figure 7.** Stacked single-layers of $W_f$/W post SPS, images taken via SEM Carl Zeiss LEODSM982.

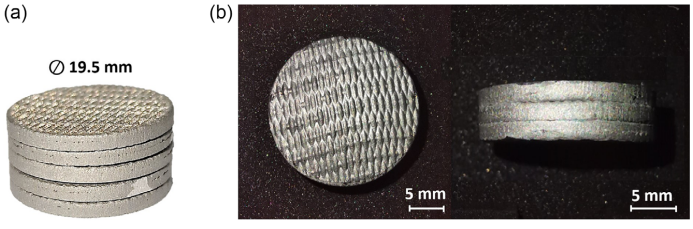


**Figure 8.** CVD-sealed discs (each two CVD-sealed layers) a) before, and b) after SPS.

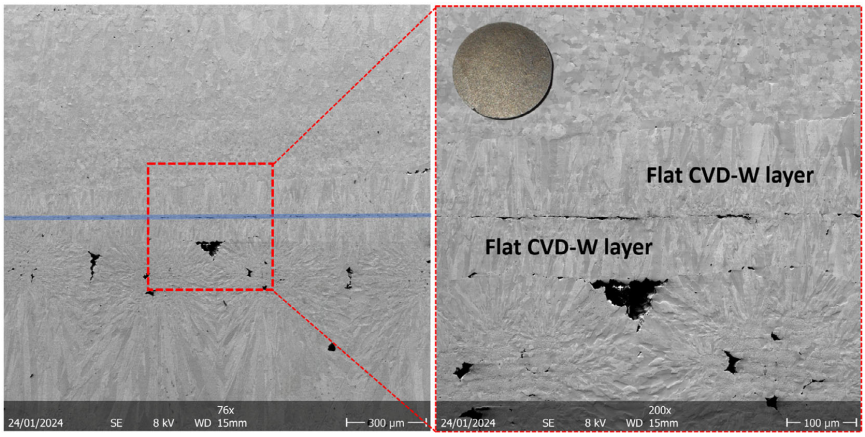


**Figure 9.** Microscopic structure of sealed double-layer CVD discs after SPS processing with flat transition area (marked in blue). No macroscopic cracks can be observed.

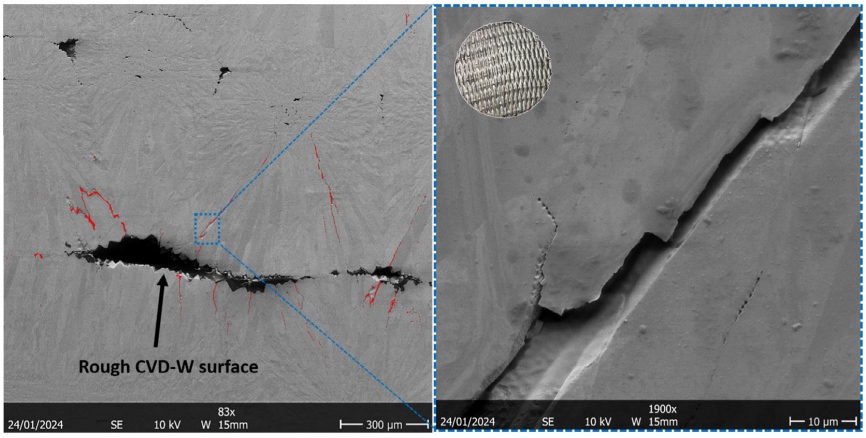


**Figure 10.** Microscopic structure of sealed double-layer CVD discs with a rough transition area. Initiated cracks introduced by high-pressure application during SPS are marked in red.

Notably, the visible pores in Figure 9 are attributed to the CVD process, not to the SPS process.

However, a rough surface leads to more significant pores, resulting in cracks within the CVD-W matrix after sintering, as shown in Figure 10. The cracks initiated by SPS are highlighted in red.

Overall, this attempt could serve as a potential compromise under the condition that the surface area is flattened sufficiently via grinding and polishing or additional CVD sealing steps could be utilized before applying sintering techniques. Still, this approach does not seem to serve as an ideal solution for further upscaling due to the heightened risk of matrix cracking.

### 4.3. Single-Layer Stacking with Powders

In order to achieve a more uniform mechanical stress distribution within the matrix and avoid additional surface treatment steps, this study also investigates sintering CVD-sealed $W_f/W$ single layers alongside with tungsten powders. The produced material closely resembles the material in Figure 8 and shows no macroscopic cracking. The microscopic analysis shown in **Figure 11** reveals that tungsten powders significantly improve the mechanical stress distribution. The W-powders effectively bridge the gaps between individual CVD-W layers, thereby mitigating the impact of the surface roughness and reducing the necessary CVD sealing steps back to a single application. However, it

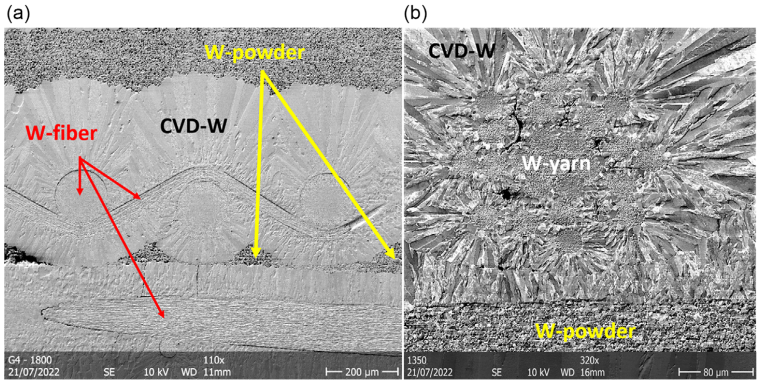


**Figure 11.** a) CVD-W-sealed single-fiber-based fabric after SPS with W-powders, and b) CVD-W sealed yarn-based fabric after SPS with W-powders.

is important to consider the limitations of this approach. The introduction of W-powders results in a reduced fiber volume fraction, which can significantly diminish the projected performance of such composites. Therefore, a comprehensive re-evaluation of combining CVD sealing with SPS is essential within this context.

However, this experiment serves as a proof of concept, particularly if there is a need to enhance, for example, thermal shock resistance or thermal conductivity. In such cases, the advantageous characteristics of CVD-W potentially offers a solution.

### 4.4. Yttria Interface Protection Utilizing CVD-W

Referring to Shu et al.[57] achieving consistent interface stabilities with conventional SPS methods remains a significant challenge. As already introduced in Section 2, yttria stability poses no concerns when using CVD-W as a matrix material.[44–56] The instability of the yttria interface appears to result from either the manufacturing method or the different structures of the matrix. To elucidate this further, **Figure 12**a provides a direct comparison between the fine crystalline and dense architecture of CVD-W in contrast to the porous structure of sintered W-powders, highlighting the potential of CVD-W to inhibit yttria diffusion into the matrix during SPS. In order to verify this, the microstructure of all discussed samples of Sections 4.1–4.3 has been analyzed utilizing SEM and energy-dispersive X-ray spectroscopy (EDX) techniques. Figure 12b shows a representative EDX analysis of the post-SPS structures, including the W-fiber, yttria interface, and the surrounding CVD-W matrix. Remarkably, no change in yttria thickness is observed before and after SPS, and no significant traces of yttria can be detected in the environment, which is a significant improvement compared to the composite structures presented in ref. [57].

A direct comparison is feasible in this context, given that the same equipment was utilized under identical process parameters. Therefore, the incorporation of CVD-W into the matrix design of SPS produced materials serves to be a fundamental solution in order to prevent instabilities of the ceramic interface.

For practical applications, however, it is also crucial to investigate whether the application of a thin CVD-W layer is sufficient enough to achieve an increased stability. In order to test the hybrid approach with a thin-film application of CVD-W for the

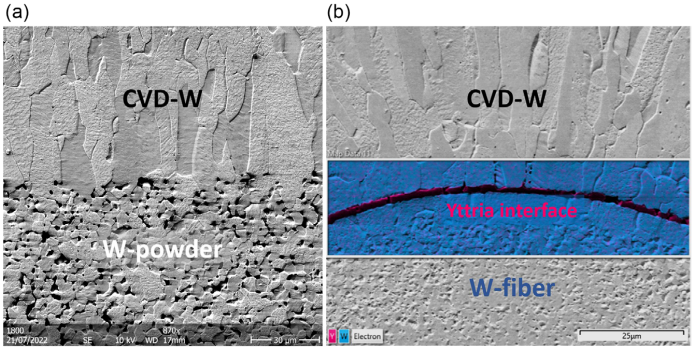


**Figure 12.** a) SEM image of the microstructures of CVD-W and W-powders post SPS, and b) EDX analysis of the W-fiber, interface, and matrix post-SPS, highlighting the yttria stability using CVD-W.

 

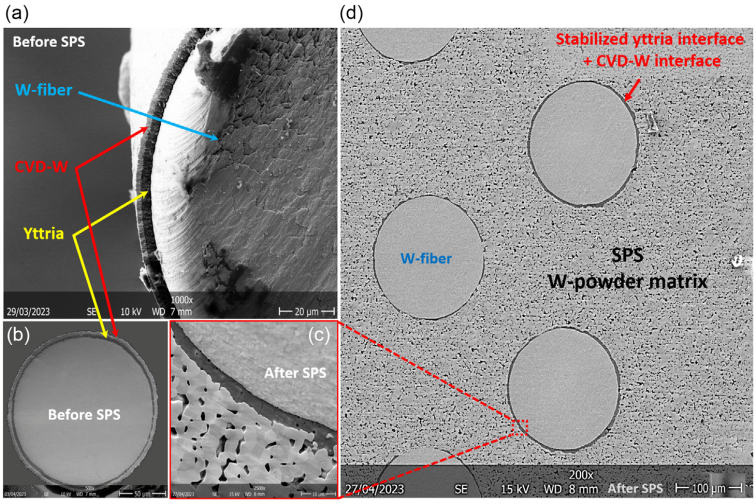


**Figure 13.** Hybrid $W_f/W$ with double-interface matrix: a) cut W-fiber including yttria and CVD-W coating before SPS, b) full cross-sectional overview of a single-coated W-fiber before SPS, c) stabilized yttria interface after SPS, and d) final matrix overview of hybrid $W_f/W$ after SPS.

first time, the same methodology as described in Section 3 is utilized, but varying CVD-parameters to $T_H = 420\,°C$, $p_c = 100$ mbar, volume flow ratio of $H_2$: $WF_6 = 12.5$: 1 for 8 min. These parameters result in a CVD-W thickness between 3 and 5 µm. The detailed protocol is provided in the attachments. **Figure 13**a,b showcase the coated fibers before sintering, highlighting the remarkable uniformity of the CVD-W films on the fiber surfaces. The resulting structures after SPS are depicted in Figure 13c,d. These images also reveal a clear improvement of the yttria stability compared to the results presented in ref. [57]. However, following sintering, the visibility of the CVD-W layer diminishes, indicating a potential necessity for a minimum thickness. While the optimal thickness of CVD-W for peak performance remains unexplored in this study, it is evident that the utilization of a thin-film shield comprising CVD-W has a considerable positive impact on the ceramic interface, consequently enhancing the desired composite structure and expected performance under fusion-related environments.

### 4.5. Tungsten Fiber Protection Utilizing CVD-W

In order to explore the advantages of using a CVD-W coating to preserve the integrity of W-fibers in carbon-containing matrices as outlined in Section 2, an additional experiment was conducted using $Cr_2AlC$ powders as the matrix material. The primary objective of this experiment is to subject tungsten fibers to conditions that would cause failure in the absence of a protective coating and to assess whether a CVD-W coating can preserve the ductility of the W-fibers. The selection of $Cr_2AlC$ powders was based on prior research indicating that tungsten fibers lose their ductility when exposed to both aluminum and carbon.[43,59] As mentioned in ref. [43], detecting trace amounts of carbon within the range of several parts per million (ppm) can be challenging, even when employing EDX techniques. The validation of this hypothesis is thus examined by producing test samples and analyzing the fracture behavior of the resulting composites. The experimental procedure aligns with the method outlined in chapter 3, with SPS parameters adapted to.[60] Slight variations are detailed in the attachments. The CVD parameters are similar to those used for the samples presented in Figure 13.

Following processing, the sample produced was sectioned into five KLST-type specimens using EDM and subsequently tested according to DIN EN ISO 179-1:2000 standards with a loading speed of $1\,\mu m\,s^{-1}$. The results are shown in **Figure 14**.

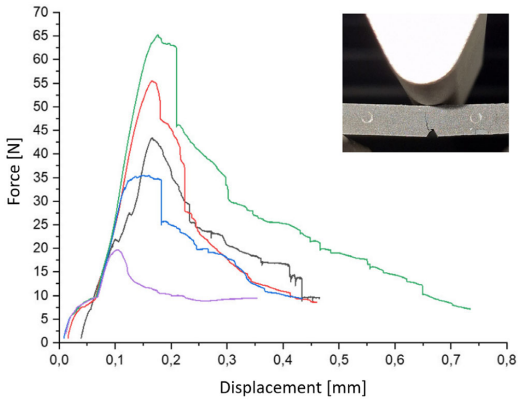


**Figure 14.** Force–displacement curves of KLST-type samples according to DIN EN ISO 179-1:2000 made of tungsten fiber-reinforced $Cr_2AlC$ after SPS processing.

All specimens exhibit a typical pseudoductile fracture behavior, showing increasing load-bearing capacity after initial crack formation. The low reproducibility of the diagrams is likely attributed to several factors such as a low fiber volume fraction <10%, an uneven layer distribution due to manual integration, and inconsistencies in matrix properties resulting from not optimized process parameters. Nevertheless, this figure clearly demonstrates that the W-fibers retained at least partially their ductility and capability to reinforce a ceramic matrix in the presence of carbon and aluminum, which would not be the case in the absence of a CVD-W protective layer surrounding the ceramic interface.[43,59]

Examining the fracture surface of the composites in **Figure 15**a reveals the interactions between the CVD-W coating and the surrounding matrix, leading to the formation of unidentified new phases. Conversely, Figure 15b demonstrates that the protective CVD-W shield primarily interacts with the matrix, thereby significantly reducing interactions between the fiber and matrix.

Although trace elements of carbon and aluminum are still present within the yttria layer, increasing the thickness of the CVD-W should prevent the interaction between the fiber and matrix entirely. However, the determination of the optimal CVD-W layer thickness and its dependence on the sintering parameters remain explored within this study.

## 5. Discussion

The methodologies analyzed in Section 4.1–4.3 explore various sintering techniques for entirely sealed textile fabrics made of potassium-doped tungsten fibers with CVD-W. While two methods are considered to be practically feasible, their practical relevance is reduced by additional drawbacks. Nonetheless, a crucial advantage emerges in principle: an anticipated increase in thermal shock resistance and thermal conductivity compared to a pure matrix of sintered W-powders.[20–23] The implementation of a chemical vapor infiltration (CVI) process would still be a preferable solution to enhance the properties of the composites, but this approach has not yet been successfully scaled up in practice.[17] If this situation persists, the methods introduced in Sections 4.2 and 4.3 could regain practical significance.

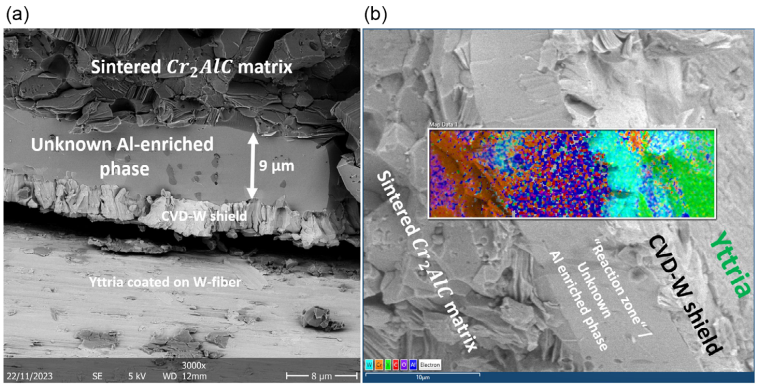


**Figure 15.** EDX analysis of W-fiber-reinforced matrix containing chromium, aluminum, and carbon with protective layer of 4.5 µm of CVD-W.

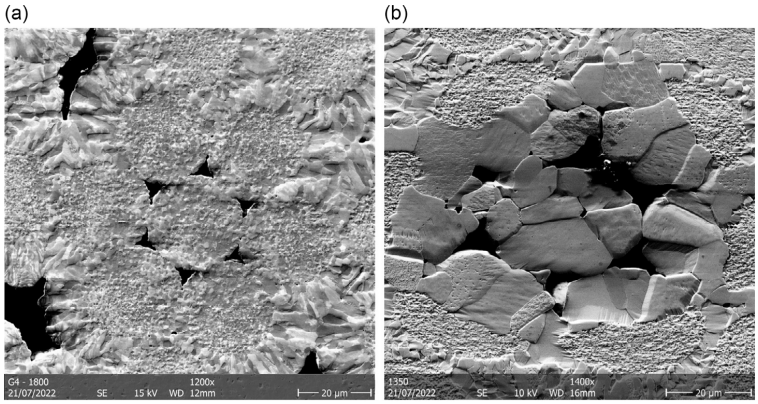


**Figure 16.** W-Yarn destruction post SPS: a) peripheral region, and b) core region.

Sections 4.4 and 4.5 introduce a novel and the most promising strategy for combining CVD with SPS techniques: Here, tungsten fibers and yttria interfaces are simultaneously protected during SPS by a thin CVD-W layer, which is coated onto the yttria surfaces' presintering.

This method holds immense potential for the successful upscaling of tungsten fiber-reinforced tungsten ($W_f$/W) composites and offers a solution to implement tungsten fibers as a reinforcing element in different matrices such as ceramics, which are also known for their intrinsic brittleness.

However, this method does not comprehensively address all sintering-related challenges, as shown in **Figure 16**.

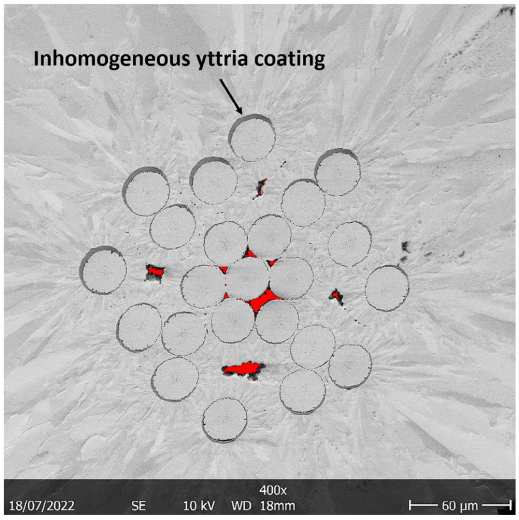


**Figure 17.** Demonstration of inhomogeneous yttria coating via magnetron sputtering on radial braided yarns after CVD and before SPS. Initially initiated CVD gaps are highlighted in red.

Notably, radial braided yarns, comprised of thin W-fibers ($d = 25$ µm), currently recrystallize during SPS, and this recrystallization is unevenly distributed throughout the produced samples.

This imbalance underlines the need for optimization strategies to achieve a more homogeneous stress distribution during SPS, which is potentially related to the pulsed direct current during the heating phase. The electrical conductivity of the W-fibers is significantly higher than that of the surrounding matrix, especially in the beginning of the sintering process. Consequently, the targeted values of the SPS machine may deviate from the actual conditions within the sample, which are impossible to measure directly. Hence, it is suggested that the yttria coating on the W-fibers could serve an additional role in composite production during SPS: The electrically insulating nature of yttria may mitigate the current passing through the W-fibers, reducing discrepancies in electrical conductivity between the fibers and matrix, thereby promoting a more uniform temperature distribution within the sample. **Figure 17**, which displays the structure of the yttria coating before SPS, provides further insights into the differences observed in Figure 16b.

Notably, the applied magnetron sputtering method primarily coats the outer shell of complex structures, offering a potential explanation for these variations between uncoated filaments in the core of the yarn and the coated sleeve filaments. These are just partially coated with yttria, but show less damage in average.

Enabling the application of high-quality yttria coatings via CVD could serve as a potential solution for successfully integrating complex textile structures like W-yarns into tungsten fiber-reinforced composites with SPS techniques. However, simple textile designs such as single fiber-based fabrics, demonstrate enhanced yttria coverage, potentially increasing their stability during SPS, as indicated in **Figure 18**. This figure also reveals a noteworthy aspect observed during this analysis: the partial deformation of W-fibers post-SPS, varying with the fibers' location. These findings underscore the need for further research into the interplay of fiber deformation and mechanical performance. Additionally, exploring the

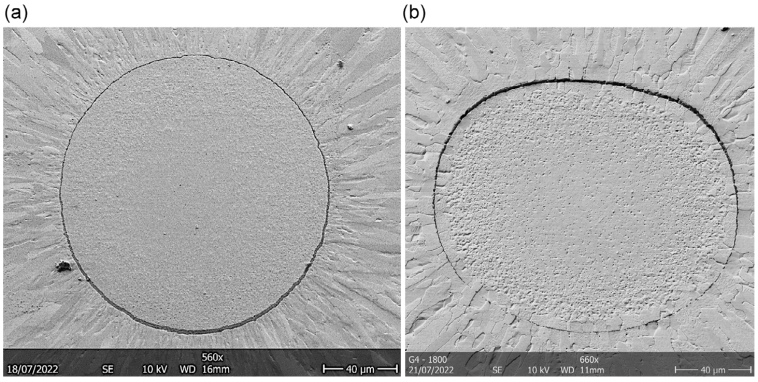


**Figure 18.** Comparison of a 150 µm W-fiber a) before, and b) post-SPS.

relationship between W-fiber diameter, potassium doping, and resulting material performance is essential for developing a sophisticated manufacturing process suitable for industrial applications.

## 6. Conclusion and Outlook

In this study, the potential synergy between CVD and SPS for the production of $W_f$/W was investigated. Stacking individual layers of fully sealed textile fabrics with CVD-W via SPS was found to be unsuitable for creating a coherent composite material, primarily due to the high mechanical stress applied by the SPS device. By enhancing the mechanical resilience of the base discs made of $W_f$/W through double CVD stacking, a solution was identified, particularly when there is a need for a rapid layer stacking. It is essential to note that this technique carries a significant risk of matrix cracking, as it heavily relies on the surface roughness. Therefore, before considering this approach for industrial applications, additional surface treatment steps and further in-depth investigation are required. Another technique explored involves the combination of CVD-W sealed fabrics with W-powders. While this method is technically achievable, it would result in a diminished material performance, which is attributed to a decrease in fiber volume fraction. To bolster the potential thermal shock resistance and conductivity of the composites through elevated CVD-W content, focus should primarily be directed toward enabling the upscaling of CVI techniques. Should practical challenges hinder the scaling of this method, the approaches outlined in Sections 4.2 and 4.3 could regain significance as a viable compromise solution.

A key finding of this research involves the strategic application of additional thin, finely crystallized CVD-W layers onto the ceramic interface. This technique significantly improves the stability of yttria and the potassium-doped W-fibers during SPS, substantially reducing the interaction with the surrounding matrix and the decrease of the yttria layer thickness during sintering.

Such a method not only addresses concerns like carbon embrittlement but may also enable the incorporation of W-fibers into a variety of matrix materials, extending beyond tungsten.

Additionally, it is indicated that the instabilities of the radially braided yarns are linked to the inhomogeneous application of yttria via physical magnetron sputtering. A homogeneous yttria coating via, for example, CVD techniques could serve as a potential solution. Initial experiments with Archer Technicoat Ltd, UK are currently being investigated. Future studies will focus on identifying the influence of the process parameters during CVD and SPS. Also, the impact of fiber diameter, potassium doping content, and homogeneity of each coating needs to be evaluated in order to find optimal composite structures for maximum material performance. Such efforts may even lead to the development of a diverse portfolio tailored to different application fields.

## Acknowledgements

This work was carried out within the framework of the EUROfusion Consortium, funded by the European Union via the Euratom Research and Training Programme (grant agreement no. 101052200. EUROfusion). Views and opinions expressed are however those of the author(s) only and do not necessarily reflect those of the European Union or the European Commission. Neither the European Union nor the European Commission can be held responsible for them.

Open Access funding enabled and organized by Projekt DEAL.

## Conflict of Interest

The authors declare no conflict of interest.

## Data Availability Statement

The data that support the findings of this study are available from the corresponding author upon reasonable request.

## Keywords

chemical vapor deposition-W, chemical vapor deposition-$W_f$/W, fusion, hybrid-$W_f$/W, metal matrix composites, spark plasma sintering-$W_f$/W, tungsten

Received: November 16, 2023
Revised: March 28, 2024
Published online:

[1] S. J. Zinkle, N. M. Ghoniem, *Fusion Eng. Des.* **2000**, *51–52*, 55.
[2] J. W. Coenen, Y. Mao, S. Sistla, A. V. Müller, G. Pintsuk, M. Wirtz, J. Riesch, T. Hoeschen, A. Terra, J. H. You, H. Greuner, A. Kreter, C. Broeckmann, R. Neu, C. Linsmeier, *Fusion Eng. Des.* **2019**, *146*, 1431.
[3] F. Klein, A. Litnovsky, T. Wegener, X. Y. Tan, J. Gonzalez-Julian, M. Rasinski, J. Schmitz, C. Linsmeier, M. Bram, J. W. Coenen, *Fusion Eng. Des.* **2019**, *146*, 1198.
[4] D. Stork, P. Agostini, J. L. Boutard, D. Buckthorpe, E. Diegele, S. L. Dudarev, C. English, G. Federici, M. R. Gilbert, S. Gonzalez, A. Ibarra, C. Linsmeier, A. L. Puma, G. Marbach, L. W. Packer, B. Raj, M. Rieth, M. Q. Tran, D. J. Ward, S. J. Zinkle, *Fusion Eng. Des.* **2014**, *89*, 1586.
[5] J. You, G. Mazzone, E. Visca, H. Greuner, M. Fursdon, Y. Addab, C. Bachmann, T. Barrett, U. Bonavolonta, B. Boswirth, F. M. Castrovinci, C. Carelli, D. Coccorese, R. Coppola, F. Crescenzi, G. Di Gironimo, P. A. Di Maio, G. Di Mambro, F. Domptail, D. Dongiovanni, G. Dose, D. Flammini, L. Forest, P. Frosi, F. Gallay, B. E. Ghidersa, C. Harrington, K. Hunger, V. Imbriani, M. Li, et al. *Fusion Eng. Des.* **2022**, *175*, 113010.
[6] J. H. You, G. Mazzone, E. Visca, C. Bachmann, E. Autissier, T. Barrett, V. Cocilovo, F. Crescenzi, P. K. Domalapally, D. Dongiovanni, S. Entler, G. Federici, P. Frosi, M. Fursdon, H. Greuner, D. Hancock, D. Marzullo, S. McIntosh, A. V. Muller, M. T. Porfiri, G. Ramogida, J. Reiser, M. Richou, M. Rieth, A. Rydzy, R. Villari, V. Widak, *Fusion Eng. Des.* **2016**, *109*, 1598.
[7] J. H. You, E. Visca, C. Bachmann, T. Barrett, F. Crescenzi, M. Fursdon, H. Greuner, D. Guilhem, P. Languille, M. Li, S. McIntosh, A. V. Muller, J. Reiser, M. Richou, M. Rieth, *Nucl. Mater. Energy* **2016**, *9*, 171.
[8] J. H. You, E. Visca, T. Barrett, B. Boswirth, F. Crescenzi, F. Domptail, M. Fursdon, F. Gallay, B. E. Ghidersae, H. Greunera, M. Li, A. V. Muller, J. Reiser, M. Richou, S. Roccella, C. Vorpahl, *Nucl. Mater. Energy* **2018**, *16*, 1.

 

[9] C. Linsmeier, M. Rieth, J. Aktaa, T. Chikada, A. Hoffmann, J. Hoffmann, A. Houben, H. Kurishita, X. Jin, M. Li, A. Litnovsky, S. Matsuo, A. von Muller, V. Nikolic, T. Palacios, R. Pippan, D. Qu, J. Reiser, J. Riesch, T. Shikama, R. Stieglitz, T. Weber, S. Wurster, J. H. You, Z. Zhou, *Nucl. Fusion* **2017**, *57*, 092007.
[10] J. Riesch, M. Aumann, J. W. Coenen, H. Gietl, G. Holzner, T. Höschen, P. Huber, M. Li, C. Linsmeier, R. Neu, *Nucl. Mater. Energy* **2016**, *9*, 75.
[11] J. Riesch, Y. Han, J. Almanstötter, J. W. Coenen, T. Höschen, B. Jasper, P. Zhao, C. Linsmeier, R. Neu, *Phys. Scr.* **2016**, *2016*, 014006.
[12] J. W. Coenen, *Adv. Eng. Mater.* **2020**, *22*, 1901376.
[13] J. W. Coenen, M. Berger, M. J. Demkowicz, D. Matveev, A. Manhard, R. Neu, J. Riesch, B. Unterberg, M. Wirtz, C. Linsmeier, *Nucl. Mater. Energy* **2017**, *12*, 307.
[14] J. W. Coenen, Y. Mao, S. Sistla, J. Riesch, T. Hoeschen, C. Broeckmann, R. Neu, C. Linsmeier, *Nucl. Mater. Energy* **2018**, *15*, 214.
[15] J. W. Coenen, Y. Mao, J. Almanstotter, A. Calvo, S. Sistla, H. Gietl, B. Jasper, J. Riesch, M. Rieth, G. Pintsuk, F. Klein, A. Litnovsky, A. V. Mueller, T. Wegener, J. H. You, C. Broeckmann, C. Garcia-Rosales, R. Neu, C. Linsmeier, *Fusion Eng. Des.* **2017**, *124*, 964.
[16] A. Lau, J. W. Coenen, D. Schwalenberg, Y. Mao, T. Höschen, J. Riesch, L. Raumann, M. Treitz, H. Gietl, A. Terra, B. Göhts, C. Linsmeier, K. Theis-Bröhl, J. Gonzalez-Julian, *J. Nucl. Eng.* **2023**, *4*, 375.
[17] J. Riesch, M. Aumann, J. W. Coenen, H. Gietl, G. Holzner, T. Hoschen, P. Huber, M. Li, C. Linsmeier, R. Neu, *Nucl. Mater. Energy* **2016**, *9*, 75.
[18] S. X. Zhao, F. Liu, S. G. Qin, J. P. Song, G.-N. Luoa, *Fusion Sci. Technol.* **2013**, *64*, 225.
[19] D. Schwalenberg, J. W. Coenen, J. Riesch, T. Hoeschen, Y. Mao, A. Lau, H. Gietl, L. Raumann, P. Huber, C. Linsmeier, R. Neu, *Engineering* **2022**, *3*, 306.
[20] S. Palaniyappan, M. Trautmann, Y. R. Mao, J. Riesch, P. Gowda, N. Rudolph, J. W. Coenen, R. Neu, G. Wagner, *Coatings* **2021**, *11*, 1128.
[21] H. O. Pierson, in *Handbook of Chemical Vapor Deposition (CVD) Principles, Technology, and Applications*, Noyes Publication, Park Ridge, NJ **1999**.
[22] X. Yongdong, X.-T. Xu, in *Chemical Vapour Deposition: An Integrated Design for High-Performance Materials*, Springer Science & Business Media March **2010**.
[23] J. Riesch, T. Höschen, C. Linsmeier, S. Wurster, J. H. You, *Phys. Scr.* **2014**, *2014*, 014031.
[24] Y. Mao, J. W. Coenen, C. Liu, A. Terra, X. Tan, J. Riesch, T. Höschen, Y. Wu, C. Broeckmann, C. Linsmeier, *J. Nucl. Eng.* **2022**, *3*, 446.
[25] Y. Mao, J. W. Coenen, J. Riesch, S. Sistla, J. Almanstötter, B. Jasper, A. Terra, T. Höschen, H. Gietl, M. Bram, J. Gonzalez-Julian, C. Linsmeier, C. Broeckmann, *Phys. Scr.* **2017**, *2017*, 014005.
[26] Y. Mao, J. W. Coenen, J. Riesch, S. Sistla, J. Almanstotter, B. Jasper, A. Terra, T. Hoschen, H. Gietl, C. Linsmeier, C. Broeckmann, *Composites, Part A* **2018**, *107*, 342.
[27] Y. Mao, J. W. Coenen, J. Riesch, S. Sistla, J. Almanstotter, J. Reiser, A. Terra, C. Chen, Y. Wu, L. Raumann, T. Hoschen, H. Gietl, R. Neu, C. Linsmeier, C. Broeckmann, *Nucl. Fusion* **2019**, *59*, 086034.
[28] Y. Mao, J. W. Coenen, J. Riesch, S. Sistla, J. Almanstötter, A. Terra, C. Chen, Y. Wu, L. Raumann, T. Höschen, H. Gietl, R. Neu, C. Broeckmann, C. Linsmeier, *Adv. Eng. Mater.* **2020**, *22*, 1901242.
[29] Y. Mao, J. W. Coenen, S. Sistla, X. Tan, J. Riesch, L. Raumann, D. Schwalenberg, T. Höschen, C. Chen, Y. Wu, C. Broeckmann, C. Linsmeier, *Phys. Scr.* **2020**, *2020*, 014030.
[30] Y. Mao, J. Engels, A. Houben, M. Rasinski, J. Steffens, A. Terra, C. Linsmeier, J. W. Coenen, *Nucl. Mater. Energy* **2017**, *T170*, 2.
[31] Y. R. Mao, J. Coenen, S. Sistla, C. Liu, A. Terra, X. Y. Tan, J. Riesch, T. Hoeschen, Y. C. Wu, C. Broeckmann, C. Linsmeier, *Mater. Sci. Eng., A* **2021**, *817*, 141361.
[32] H. Gietl, J. Riesch, J. W. Coenen, T. Höschen, R. Neu, *Fusion Eng. Des.* **2019**, *146*, 1426.
[33] H. Gietl, A. von Muller, J. W. Coenen, M. Decius, D. Ewert, T. Hoschen, P. Huber, M. Milwich, J. Riesch, R. Neu, *J. Compos. Mater.* **2018**, *52*, 3875.
[34] L. Raumann, J. W. Coenen, J. Riesch, Y. Mao, D. Schwalenberg, T. Wegener, H. Gietl, T. Hoschen, C. Linsmeier, O. Guillon, *Nucl. Mater. Energy* **2021**, *28*, 101048.
[35] L. Raumann, J. W. Coenen, J. Riesch, Y. R. Mao, D. Schwalenberg, H. Gietl, C. Linsmeier, O. Guillon, *Metals* **2021**, *11*, 1089.
[36] J. W. Coenen, P. Huber, A. Lau, L. Raumann, D. Schwalenberg, Y. Mao, J. Riesch, A. Terra, C. Linsmeier, R. Neu, *Phys. Scr.* **2021**, *96*, 124063.
[37] J. W. Coenen, M. Treitz, H. Gietl, P. Huber, T. Hoeschen, L. Raumann, D. Schwalenberg, Y. Mao, J. Riesch, A. Terra, C. Broeckmann, O. Guillon, C. Linsmeier, R. Neu, *Phys Scr.* **2020**, *2020*, 014061.
[38] O. Guillon, J. Gonzalez-Julian, B. Dargatz, T. Kessel, G. Schierning, J. Rathel, M. Herrmann, *Adv. Eng. Mater.* **2014**, *16*, 830.
[39] S. X. Song, Z. Wang, G. P. Shi, *Ceram. Int.* **2013**, *39*, 1393.
[40] J. Y. Wu, F. Chen, Q. Shen, J. M. Schoenung, L. M. Zhang, *J. Nanomater.* **2013**, *2013*, 2.
[41] Z. A. Munir, U. Anselmi-Tamburini, M. Ohyanagi, *J. Mater. Sci.* **2006**, *41*, 763.
[42] E. A. Olevsky, S. Kandukuri, L. Froyen, *J. Appl. Phys.* **2007**, *102*, 114913.
[43] C. C. Y. Mao, J. W. Coenen, J. Riesch, S. Sistla, J. Almanstötter, A. Terra, Y. Wu, F. L. Raumann, T. Höschen, H. Gietl, H. R. Neu, H. C. Linsmeier, C. Broeckmann, *Fusion Eng. Des.* **2019**, *145*, 18.
[44] P. Zhao, J. Riesch, T. Höschen, J. Almanstötter, M. Balden, J. W. Coenen, R. Himml, W. Pantleon, U. von Toussaint, R. Neu, *Int. J. Refract. Met. Hard Mater.* **2017**, *68*, 29.
[45] J. L. Walter, C. L. Briant, *J. Mater. Res.* **2011**, *5*, 2004.
[46] D. Terentyev, J. Riesch, S. Lebediev, T. Khvan, A. Zinovev, M. Rasinski, A. Dubinko, J. W. Coenen, *Int. J. Refract. Met. Hard Mater.* **2018**, *73*, 38.
[47] D. Terentyev, J. Riesch, S. Lebediev, A. Bakaeva, J. W. Coenen, *Int. J. Refract. Met. Hard Mater.* **2017**, *66*, 127.
[48] D. B. Snow, *Metall. Trans. A* **1979**, *10*, 815.
[49] D. B. Snow, *Metall. Trans. A* **1976**, *7*, 783.
[50] M. R. Ripoll, J. Očenášek, *Eng. Fract. Mech.* **2009**, *76*, 1485.
[51] V. Nikolic, J. Riesch, M. J. Pfeifenberger, R. Pippan, *Mater. Sci. Eng., A* **2018**, *737*, 434.
[52] S. N. Mathaudhu, A. J. deRosset, K. T. Hartwig, L. J. Kecskes, *Mater. Sci. Eng., A* **2009**, *503*, 28.
[53] O. Horacsek, *IEE Proc.-A: Phys. Sci., Meas. Instrum., Manage. Educ.* **1980**, *127*, 125.
[54] P. F. Browning, C. L. Briant, K. Rajan, B. A. Knudsen, *Eng. Failure Anal.* **1995**, *2*, 105.
[55] C. L. Briant, O. Horacsek, K. Horacsek, *Metall. Trans. A* **1993**, *24*, 843.
[56] B. Mainzer, C. R. Lin, M. Friess, R. Riedel, J. Riesch, A. Feichtmayer, M. Fuhr, J. Almanstötter, D. Koch, *J. Eur. Ceram. Soc.* **2021**, *41*, 3030.
[57] R. Shu, Y. Mao, J. W. Coenen, A. Terra, C. Liu, S. Schönen, J. Riesch, C. Linsmeier, C. Broeckmann, *Mater. Sci. Eng., A* **2022**, *857*, 144098.
[58] L. Raumann, J. W. Coenen, J. Riesch, Y. Mao, H. Gietl, T. Hoschen, C. Linsmeier, O. Guillon, *Surf. Coat. Technol.* **2020**, *381*, 124745.
[59] H. Z. Zhang, P. Z. Feng, F. Akhtar, *Sci. Rep.* **2017**, *7*, 1845.
[60] D. B. Lee, T. D. Nguyen, *J. Alloys Compds.* **2008**, *464*, 434.

# 10 Publication 2 – Epilogue

The findings presented in Publication [2] illustrate the substantial potential of the hybrid approach to extend the scope of applications for WFRCs. The incorporation of a thin sacrificial layer of CVD-W into the composite design results in a notable enhancement in the structural integrity of the W-fibers and the yttria interface during spark-plasma sintering (SPS). This innovation not only enhances the stability of conventional powder-based $W_f$/W composites but also provides a pathway for integrating W-fibers into chemically interactive matrix materials during sintering.

This advancement addresses specific challenges identified in the literature [298, 299] and may facilitate the incorporation of W-fiber reinforcement in W-based alloys, such as SMART alloys, which were previously introduced in Section 2.2. Additionally, it may permit the integration of W-fibers into advanced ceramic materials, such as those investigated by Gonzalez-Julian et al. in references [300, 301]. Accordingly, the presented hybrid strategy offers considerable potential for the development of WFRCs with tailored material properties, including density, oxidation resistance, and thermal conductivity. It is anticipated that such advanced composites could be utilized in various high-performance sectors, including aerospace, medical technologies, and nuclear environments.

Nevertheless, despite its conceptual promise for diverse industrial applications, scaling this method is currently constrained by various challenges that demand further investigation. For $W_f$/W composites, a major limitation lies in its reliance on W-powders during processing or the requirement of at least two Batch-LPCVD sealing steps prior to SPS. Both of these compromises introduce a considerable degree of intricacy to the manufacturing process, thereby imposing significant limitations on its scalability. Additionally, the current method and associated processing parameters are incompatible with W-yarns, which significantly restricts the design freedom of the resulting composite architecture. Furthermore, the hybrid approach results in composites with a lower relative density and inferior mechanical properties compared to those produced exclusively by the Batch-LPCVD method. Therefore, the results presented in Publication [1] still remain as the performance benchmark for $W_f$/W composites.

In light of the intended application of $W_f$/W composites in nuclear fusion environments, any decline in material performance is considered as unacceptable. To preserve the material performance outlined in Publication [1], a return to a purely CVD-based consolidation process is regarded as essential. The CVD technique continues to provide superior reliability and greater design flexibility for the resulting composite structures, as it introduces significantly lower stresses into the material compared to sintering methods. Building on this foundation, the second scaling strategy proposed in this thesis, the continuous CVD method, will be introduced in the following chapter.

# 11 Scaling Method 2 – Continuous CVD

The continuous CVD method, originally proposed by Gietl et al. in references [294, 302], represents the second upscaling approach investigated in this thesis. Similar to the hybrid method presented in Publication [2], this concept was developed to address the inherent limitations of the Batch-LPCVD process, particularly the time-intensive heating and cooling cycles discussed in Chapter 7.1. The fundamental premise of this approach is to establish a continuous manufacturing route for $W_f$/W composites, thereby eliminating the necessity for frequent chamber openings.

Central to this technique is the developed FRED (For Rotary Enhanced Deposition) system. This equipment was specifically designed as a customized upgrade to the existing WILMA chemical processing facility, extending its functionality to enable continuous CVD operation. An adapted 3D model of this system, based on the original construction data created and provided by Gietl in reference [294], is presented in Figure 19.

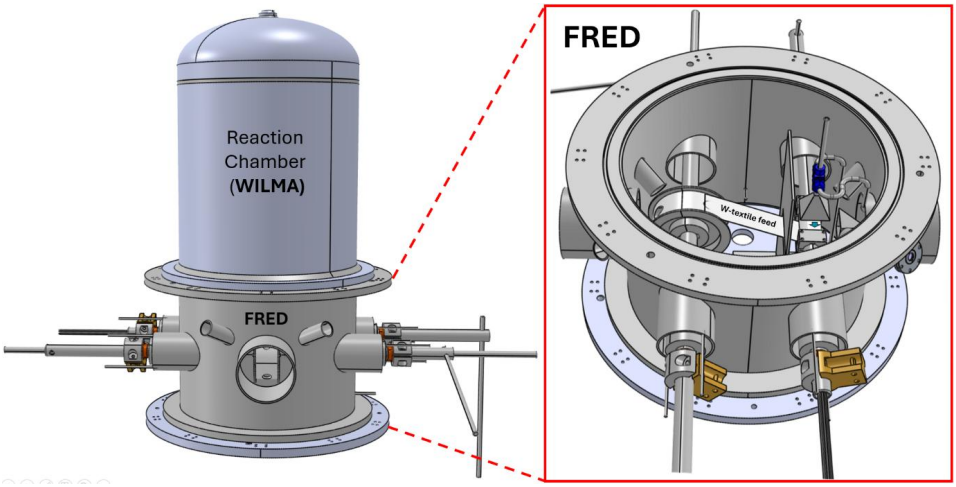


*Figure 19: WILMA reaction chamber with the integrated FRED setup for continuous CVD processing. Adapted from construction data provided by Gietl [294].*

Figure 20 provides an enlarged and more detailed overview of the highlighted section in Figure 19, offering a comprehensive insight into the most important design features of the FRED system [294].

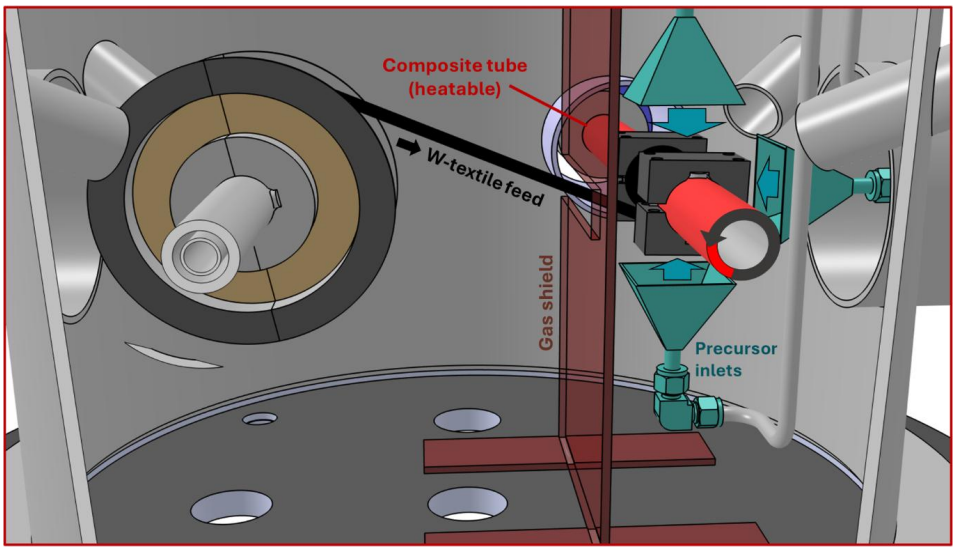


*Figure 20: Detailed schematic of the FRED system, showing the W-textile feed, precursor supply from three directions, rotating hot composite tube, and gas shield for enhanced deposition control. Adapted from construction data provided by Gietl [294].*

The key component of this configuration is a heatable and rotatable composite tube that serves as a deposition surface, analogous in function to the flat heating table described in Publications [1] and [2]. In order to guarantee the uninterrupted production of $W_f$/W composites, the system must ensure homogeneous deposition conditions throughout the entirety of the W-textile structure. This is intended to be achieved by maintaining a continuous supply of the precursors $WF_6$ and $H_2$ via three strategically positioned inlets. The W-textile is conveyed through a gas shield, which serves to prevent premature deposition of CVD-W. Importantly, the process is conducted in accordance with the parameter range defined in Section 3.4 to maintain consistent and reliable CVD-W deposition in a low-pressure environment.

Initial investigations employing the FRED system indicated the promising formation of localized regions with dense microstructures and favorable grain growth. However, the results also demonstrated inconsistencies in density distribution, which were initially attributed to the non-uniform flow of $WF_6$, likely driven by the combined effects of its high density and gravitational forces [302].

Further analysis conducted within the scope of this work revealed that insufficient precursor temperatures, rather than irregular precursor flow, were the primary cause of these inconsistencies. As previously outlined in Publication [2], achieving homogeneous deposition conditions necessitates rigorous control of precursor temperatures and partial pressures, alongside a precise regulation of the flow dynamics and residence times. Accordingly, a reliable and uniform consolidation with CVD-W can only be achieved through a meticulous calibration of all these parameters. Figure 21 underscores these findings, demonstrating that homogeneous deposition in both the FRED and Batch-LPCVD systems is unattainable without the integration of a preheating system, which allows for sufficient temperature control of the precursors.

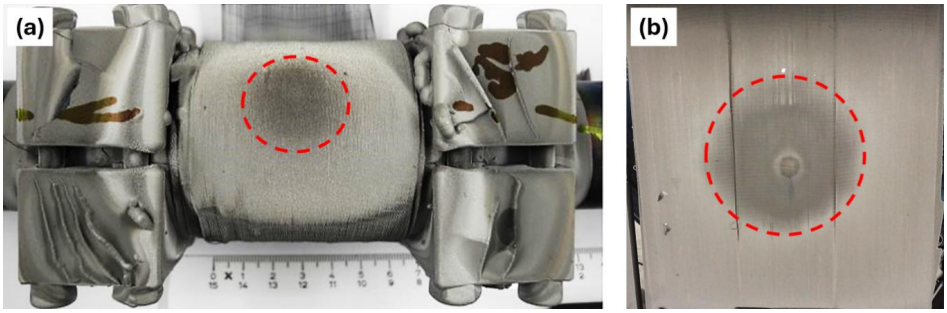


*Figure 21: Surface structures of W-textile fabrics post-CVD sealing in the absence of a preheating system, highlighting areas with reduced coating thickness. (a) Surface of the FRED setup; (b) Surface of the Batch-LPCVD setup.*

However, as previously discussed in Chapter 7.2.1, the incorporation of a preheating system introduces substantial operational challenges, such as an increased maintenance demand to ensure stable pressure control. These challenges are further intensified in the FRED system due to the uncontrolled deposition of CVD-W on several system components, including moving parts. This unintended material buildup not only heightens maintenance requirements but also increases the risk of particle detachment from critical areas, such as the upper precursor inlet shown in Figure 20. These detached particles can, in turn, embed themselves into the sample, leading to surface defects that compromise the structural integrity and reliability of the resulting composite material.

Even with a comprehensive redesign of the system, including the reduction and repositioning of the precursor inlets, enlargement of the composite tube diameter, or incorporation of supplementary shielding components, the continuous CVD process remains fundamentally constrained by the limited selection of suitable base materials.

As detailed in Publication [1], the intrinsic stiffness of conventional W-textiles poses a significant obstacle to further processing. This limitation is further exacerbated by the rotational dynamics inherent to the continuous CVD process, which introduces additional residual stresses into the composite material. As a result, only W-textiles with greater flexibility, produced from thinner fibers or yarns, can be considered as potentially suitable base materials for this manufacturing approach. Nevertheless, further research would be required to validate even their practical applicability.

This intrinsic limitation aligns with the constraints identified in the hybrid approach but manifests in an opposing manner. While the hybrid method is restricted by the incorporation of larger-diameter fibers, the continuous CVD process entirely excludes such rigid filaments, thereby markedly reducing the flexibility in composite design. Moreover, as documented in references [303-305], non-uniform fiber distributions and fiber bending angles within fiber-reinforced composites inevitably lead to a degradation of the desired material performance. Based on these insights, it becomes evident that the benchmark performance for $W_f$/W composites, as established in Publication [1], is unlikely to be achieved through the continuous CVD approach.

As previously discussed, any degradation in the resulting material performance is considered an unacceptable deviation from the desired outcome. Consequently, the viability of the continuous CVD method remains inherently limited at this stage. While conceptually promising, this approach ultimately fails to meet the stringent requirements for scalability, performance, and reliability, which are indispensable criteria for industrial implementation. In light of these limitations, this dissertation shifts its focus to the third and final scaling approach: the Chemical Vapor Infiltration (CVI) technique. This method offers a promising pathway to simultaneously address the aforementioned upscaling challenges and will be further detailed in the subsequent chapter.

# 12 Scaling Method 3 - Chemical Vapor Infiltration (CVI)

Chemical Vapor Infiltration (CVI) is an advanced adaptation of the CVD process, specifically tailored to deposit the desired matrix material within the intricate network of a porous structure, rather than merely coating or sealing their surfaces. This technique has already demonstrated its efficacy in fabricating carbon-carbon and ceramic matrix composites and has firmly established itself as a reliable manufacturing process for advanced materials in the aerospace and nuclear sectors [306-310]. Building upon this promising background and the fundamental groundwork laid by Juan Du in reference [307] and Riesch et al. in references [311-313], the present study seeks to advance the CVI process to enable the production of $W_f$/W composites at a process-relevant scale.

The primary objective is to leverage the versatility of the CVI technique to concurrently process multiple W-textile layers in a single step, thereby addressing the upscaling limitations previously identified in Chapter 7. In order to exploit this latent potential, it is imperative to first identify the major challenges that have previously hindered the upscaling of this method. The following subsection provides a concise overview of the results of previous CVI attempts and highlights the most critical obstacles that have been identified within the scope of this work.

## 12.1 Previous Attempts and Identified Challenges

In 2014, Riesch et al. achieved a significant milestone in the fabrication of $W_f$/W composites using the CVI technique, as documented in reference [311]. Their study demonstrated the first successful infiltration of a laboratory-scale $W_f$/W specimen, comprising a 10 x 9 array of single W-filaments. This achievement was realized at the inaugural pilot plant of Archer Technicoat Ltd. in the United Kingdom, employing a two-step CVI process featuring variable precursor flow directions and a movable heater.

Despite these promising initial results, subsequent efforts to replicate and upscale the CVI process at the WILMA chemical processing facility at Forschungszentrum Jülich in Germany encountered substantial challenges. Extensive investigations involving alternative precursor flow directions, revised heating strategies, and varied fiber arrangements did not yield comparable outcomes.

A recurring and critical issue observed in all experiments was the formation of sealed exteriors in the infiltrated samples, as illustrated in Figure 22. This phenomenon impeded the release of reaction by-products, such as HF, from within the sample body. The resulting accumulation of these by-products disrupted the chemical equilibrium, shifting it toward the reactant side and ultimately increasing the absolute pressure at the precursor inlet. As a consequence, all infiltration processes terminated prematurely, leaving the sample interiors largely unaffected.

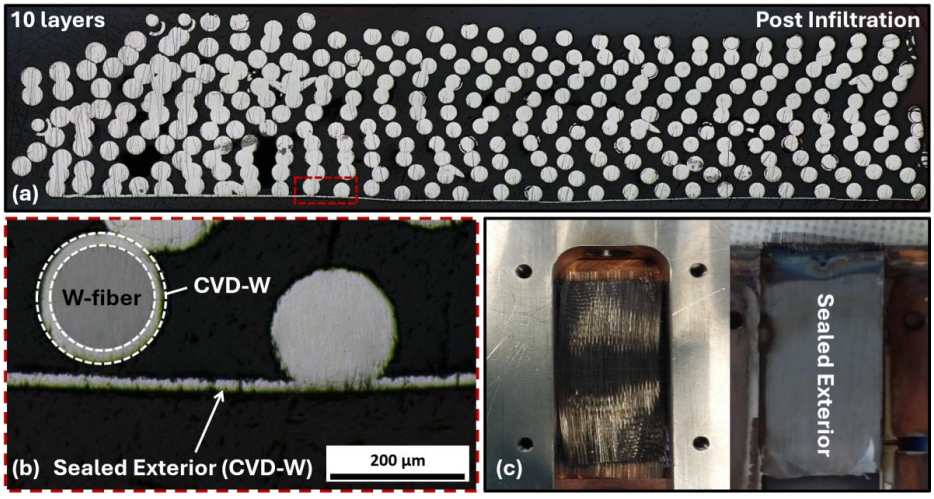


*Figure 22: Representative Illustration of Previous CVI Attempts. (a) Cross-sectional view of 10 stacked W-textile layers, illustrating a largely unaffected interior. (b) Enlarged view of the highlighted region in (a), highlighting the sealed exterior of the W-textile bundle. (c) Macroscopic images of the sample before (left) and after CVI (right), revealing that densification at the time was restricted to the outer shell.*

These observations underscore the inherent complexity of CVI, which diverges significantly from the more uniform and predictable characteristics of conventional CVD processes. The experimental results clearly indicate the necessity for advanced process control, while also revealing that the capabilities of the WILMA facility at the time were insufficient for achieving uniform matrix deposition. To address these limitations, it was first essential to develop a comprehensive production concept that provides a framework for identifying the necessary system modifications. With these insights in mind, the following chapter explores several CVI concepts aimed at overcoming these barriers and enabling a scalable composite production at the WILMA facility.

## 12.2 CVI Concepts for $W_f$/W Composite Production

The selection of an appropriate CVI concept is primarily dependent on the specific precursors used, and thus directly relates with their reaction kinetics [314-316]. Similar to standard CVD processes, CVI can be implemented in several modes, including isothermal CVI (I-CVI) [317], thermal gradient CVI (TG-CVI) [318, 319], pressure gradient CVI (PG-CVI) [320], and pulsed CVI (P-CVI) [321]. Each variant offers a distinct mechanism for controlling the growth behavior of the desired matrix material within the porous network of the specimen structure. Further details on the various CVI modes are discussed by Vignoles et al. in reference [322].

To establish a suitable baseline approach for the production of $W_f$/W composites using $WF_6$ and $H_2$ as precursors, it is instructive to revisit the relation between CVD-W growth rates ($R_W$) and the underlying process parameters, as illustrated in Figure 14 to Figure 16. These data reveal that the temperature has the most pronounced impact on the CVD-W growth rates. Therefore, to ensure optimal process control for this specific precursor combination, it is considered essential to adjust the temperature profile within the sample body. Consequently, this work primarily focuses on TG-CVI, aiming to establish a well-defined thermal gradient. To identify the most effective method for implementing this thermal gradient strategy, three conceptual approaches were evaluated:

### 12.2.1 Approach 1: Movable Heat Source with Multi-Stage Infiltration

The initial approach is based on the methodology proposed by Riesch et al. in reference [311], which utilized a movable heat source and a two-stage infiltration process. The proof of concept demonstrated at the laboratory scale, combined with its reliance on controlled temperature gradients, suggests that extending this technique to larger volumes could be potentially feasible. However, the requirement for multiple processing steps mirrors the inefficiencies observed in the Batch-LPCVD and hybrid methods discussed in Chapters 7 and 10. Furthermore, while the movable heat source offers flexibility in temperature control, it presents a significant risk of unintended CVD-W growth, which could result in the mechanical blockage of the movable component. This limitation is reminiscent of the challenges encountered with the FRED setup, as discussed in Chapter 11. Consequently, this method is considered as unsuitable for large-scale applications.

### 12.2.2 Approach 2: Multiple Heat Sources

An alternative approach for establishing a thermal gradient in the sample involves the use of multiple stationary heat sources. While this method appears relatively straightforward to implement within the WILMA configuration and avoids the reliance on movable components, the inherently high thermal conductivity of W introduces a fundamental challenge. It is anticipated that the resulting temperature gradients in $W_f$/W composites would not be sufficiently pronounced, particularly in regions close to the heat sources. This effect could intensify over extended processing times, as the densification of the composite further increases its thermal conductivity. Achieving a meaningful thermal gradient under such conditions would necessitate large sample dimensions, which are expected to be incompatible with the geometric constraints of the existing processing chamber. Furthermore, multiple processing steps would likely be required to achieve adequate densification. Therefore, the implementation of multiple heat sources has been excluded from further consideration in this study.

### 12.2.3 Approach 3: Active Sample Cooling

The third proposed strategy for establishing a controlled temperature gradient within a W-textile bundle involves the utilization of an active sample cooling mechanism. By selectively removing heat and consequently reducing the temperature in the peripheral regions of the specimen, this approach leverages the high thermal conductivity of W to inhibit undesirable chemical reactions at the outer surfaces. Accordingly, this method directly addresses the complications illustrated in Figure 22. In a CVI process employing $WF_6$ and $H_2$ as precursors, the objective is to maintain the temperature of the sample's edge regions below the critical reaction threshold of 300 °C.

This temperature control is intended to ensure a continuous precursor supply throughout the infiltration process, while enabling controlled matrix growth from the interior to the exterior and from hotter to cooler regions. Figure 23 provides a conceptual schematic of a typical TG-CVI process that employs this active cooling approach, adapted from Chawla in reference [323].

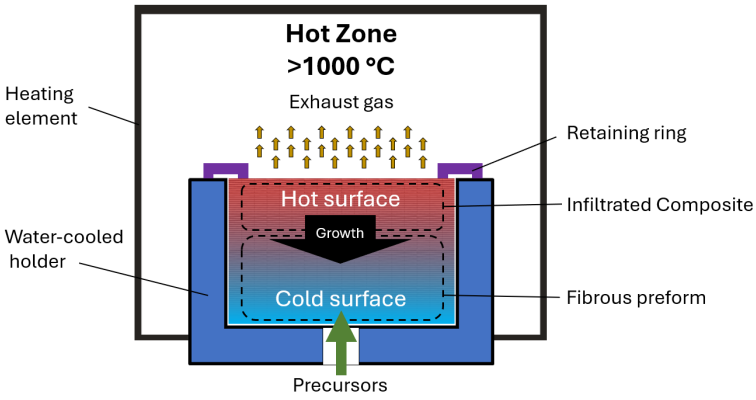


*Figure 23: Conceptual schematic of a conventional TG-CVI process for the infiltration of a fibrous preform. The graphic illustrates the establishment of temperature gradients between the hot and cold surfaces, the controlled precursor flow from the bottom to the top, and the expected matrix growth behavior within the composite structure, progressing from the hot surface toward the cold surface. Adapted from [323].*

Although this conventional TG-CVI configuration may initially appear suitable for achieving the desired temperature gradients, its prior implementations were restricted by the reliance on a global heat source. This design inherently increases energy consumption and promotes unintended deposition of the matrix material on the reactor walls. Over time, these deposits can delaminate, contaminate the exhaust pumping system, and eventually cause operational disruptions.

To mitigate these concerns, the incorporation of a localized heat source offers a more efficient alternative. However, this modification also requires a corresponding adjustment to the precursor flow direction. As indicated in Figure 23, introducing the precursor stream from the side opposite the heat source is considered essential for maximizing the temperature gradient, thereby providing enhanced control over the growth behavior of CVD-W within the porous microstructure.

Building on these considerations, the concept illustrated in Figure 24 was devised. By utilizing a localized heat source, active external cooling, and a cold precursor stream directed toward the heat source, this approach aims to create a stable and controllable thermal environment while minimizing manufacturing costs and equipment wear.

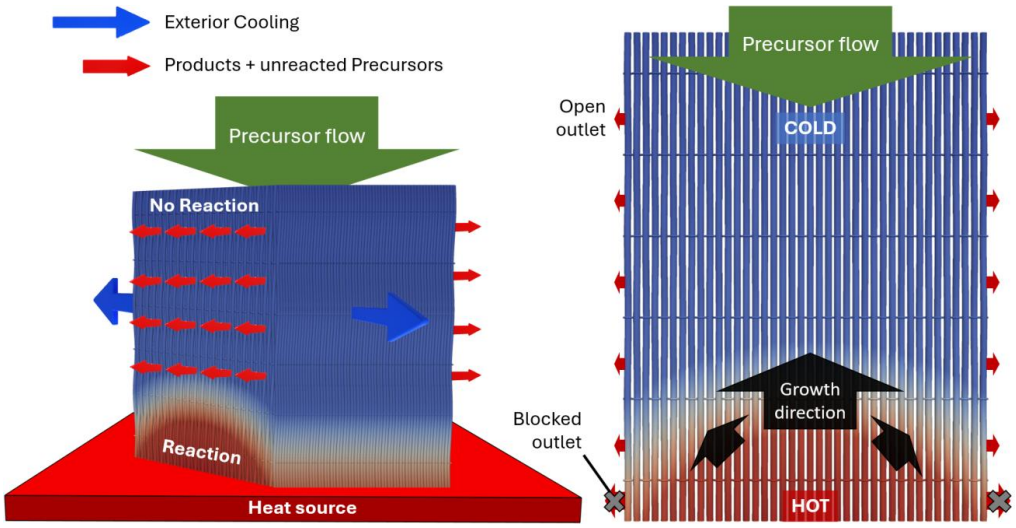


*Figure 24: Schematic of an initially asymmetric, three-dimensional temperature gradient in a W-textile bundle equipped with a localized heat source, active cooling on two sides, and gas outlets on the remaining sides. The left panel illustrates the thermal gradient, precursor flow, and reaction zones, while the right panel demonstrates the expected growth direction and gas flow behavior, highlighting the gradual blockage of the outlets in hotter regions as infiltration proceeds.*

In this configuration, two sides of the sample are actively cooled to precisely manage the local temperature profile, while the remaining two sides remain open to allow for the continuous removal of gaseous species, including unreacted precursors and HF, until peak densification is achieved.

While the initial temperature distribution may exhibit some asymmetry, the high thermal conductivity of W is expected to gradually intensify and align the gradient, thereby enabling increasingly refined control as the infiltration process advances. This control is intended to allow for the efficient cross-linking and sealing of W-textile packages regardless of the sample geometry, ultimately establishing a viable method for the industrial production of $W_f$/W composites.

At this stage, however, the approach remains predominantly theoretical. The following chapter transitions from this chosen conceptual framework to its practical implementation at the WILMA facility, focusing on the translation of these principles into a first conceptual prototype design.

## 12.3 Development of a Prototype Design

Adapting the advanced CVI concept presented in Figure 24 into a fully operational process at the WILMA facility necessitated specific modifications to the existing infrastructure. The prior integration of a localized heat source and the corresponding adjustment of the precursor flow direction during the preparation phase of the Batch-LPCVD process proved particularly advantageous for this adaptation.

These measures significantly streamlined the integration of the modified TG-CVI concept while preserving the availability of established coating and sealing procedures. Consequently, the modifications described herein can be regarded as a tailored upgrade rather than a complete redesign, analogous to the FRED system discussed in Chapter 11.

With these adjustments in place, the final modification to the WILMA facility involved the integration of an active sample cooling mechanism. A water-based cooling system was selected for its compatibility with the existing infrastructure and its effective heat transfer properties, which were considered essential for achieving significant temperature gradients within the sample body.

However, the introduction of water as a coolant directly into the reaction chamber gave rise to significant safety concerns. As elaborated in Publications [1] and [2], the chamber is designed to operate under reduced pressure, with localized temperatures approaching 800 °C, within an environment containing highly reactive species such as $WF_6$ and HF. A hypothetical failure of the coolant delivery system or excessively high coolant temperatures could initiate a rapid phase transition, resulting in a sudden pressure increase. Such a scenario could compromise the structural integrity of the chamber, damage critical components such as gaskets, and may inadvertently precipitate the release of hazardous gases. These considerations underscore the critical importance of thoroughly evaluating operational safety when implementing such design modifications.

To mitigate these conceptual challenges, a stepwise approach was adopted, commencing with a proof-of-concept configuration under controlled conditions. The primary objective was to first establish a foundational level of control over the temperature gradient across the sample, thereby verifying the viability of the concept before proceeding to more sophisticated modifications. This incremental strategy also aimed to minimize capital expenditures through the effective use of the existing infrastructure.

Figure 25 illustrates the developed prototype configuration, in which the active cooling system was positioned outside the WILMA reaction chamber to maintain a controlled and safe environment. The setup featured a water-cooled body connected to solid cooling rods and plates, creating direct thermal contact with the sample. The sample design utilized the base material available at the time and consisted of 40 stacked W-textile layers, with each layer measuring 58 mm × 120 mm. These layers were encapsulated in a copper shell and further equipped with pluggable gas outlets.

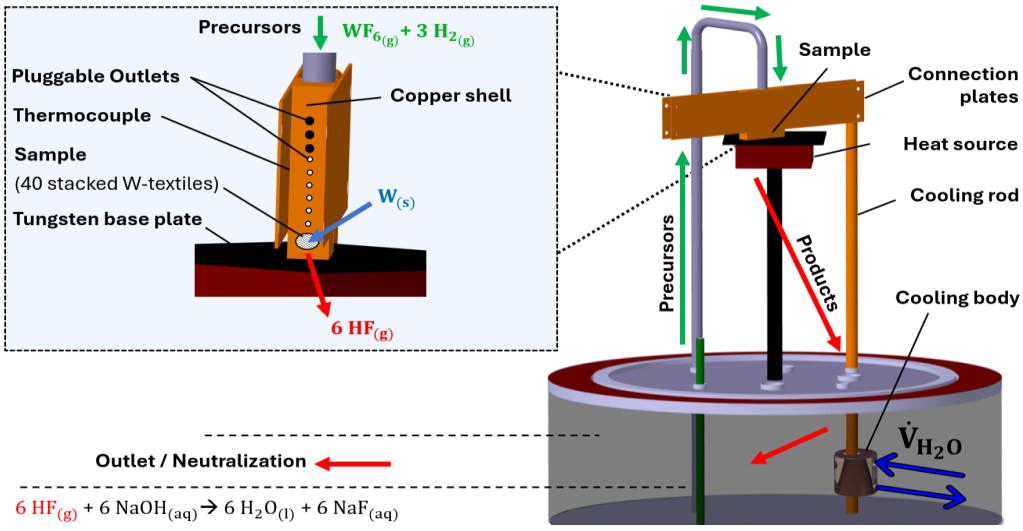


*Figure 25: Simplified WILMA configuration with an integrated local heat source and external cooling. The prototype includes cooling rods and plates in direct contact with a W-fiber bundle composed of individual W-filaments, enclosed in a copper shell and equipped with pluggable gas outlets.*

The gas outlet configuration was tailored to release the process gases exclusively in the immediate vicinity of the hot surfaces near the heat source, thereby preventing premature gas outflow and eliminating a potential source of error. Additionally, it was essential to assess whether the precursor flow could be effectively regulated in large-scale sample geometries, similar to those fabricated via the Batch-LPCVD method in Publications [1] and [4]. To this end, the stacked W-textiles were aligned longitudinally between the heat source and precursor inlet to maximize the sample height and diffusion pathways of precursors within the sample body.

Nevertheless, the transition from this conceptual prototype to a fully operational system necessitated additional refinements and the resolution of practical challenges, particularly the integration of the active sample cooling system. The following chapter outlines the primary steps of the implementation process, encompassing an overview of the reactor configuration and initial thermal modeling efforts. These aspects were instrumental in finalizing the prototype design and conducting the first experimental trials to validate the efficacy of the modified TG-CVI method proposed in this thesis.

## 12.4 Practical Implementation of the Prototype Configuration

To realize the proof-of-concept configuration illustrated in Figure 25, the geometry of the existing WILMA setup was first recorded and transferred to a CAD model. This model was then expanded to include the prototype design and refined to align with the operational constraints of the facility.

Figure 26 presents the geometric dimensions of the primary design elements. These include the cooling connections and an insulating layer specifically designed to minimize direct thermal contact between the heat source and the cooling plates. Further details regarding the external cooling body, chamber connection components, and gas outlet arrangement are provided in the Appendix.

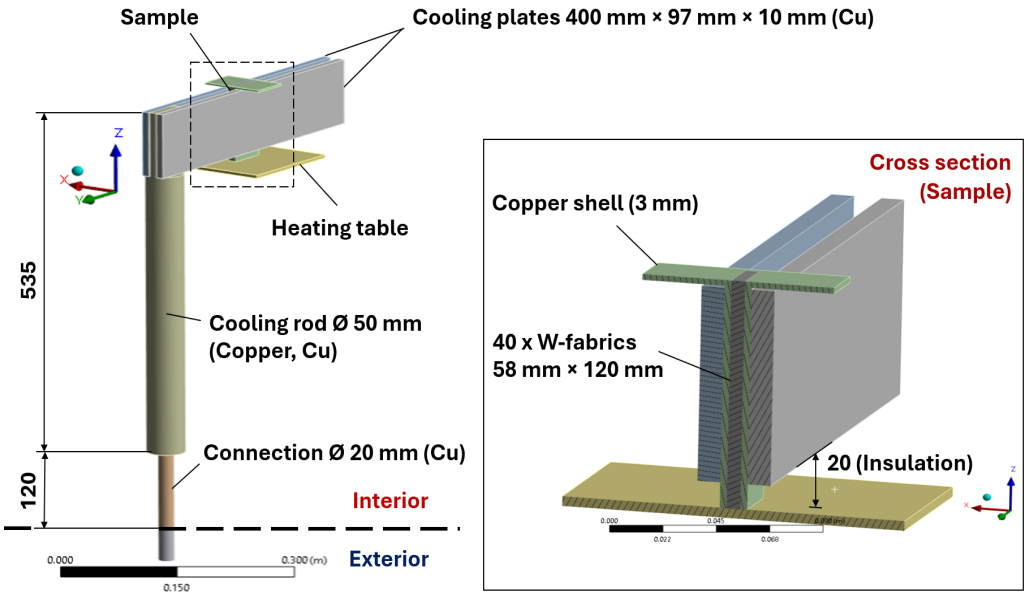


*Figure 26: Prototype setup: Geometrical dimensions of cooling plates, copper rods, insulation layer, and cooling distances.*

To implement the requisite coolant flow $\left(\dot{V}_{H_2O}\right)$ indicated in Figure 25, a new bypass line was integrated into the existing cooling circuit of the liquid ring pump. Under standard operating conditions, this circuit delivers the coolant with an inlet temperature of approximately 4 °C and an absolute pressure of 6 bar, thereby ensuring a reliable and efficient coolant supply. The diverted flow, with a specified maximum volumetric flow rate of 2 L $min^{-1}$, was connected to an electronically controlled valve, regulated by a Eurotherm 3508 PID controller.

This controller was originally employed to manage the preheater temperature in conventional coating and sealing processes. It was reprogrammed to now regulate both the preheater temperature and the coolant flow rate, based on input from a thermocouple positioned between the connection plates and the sample body, as illustrated in Figure 25. Accordingly, this reconfiguration ensured compatibility with established processes while enabling adjustments to the precursor temperature where necessary. Such flexibility could allow for enhanced control of the deposition rates, thereby creating opportunities for further process optimization subsequent to the potential validation of the concept.

To extend the operational capabilities of the facility, the integrated piping system was designed to transport both liquids and gases under high-pressure conditions, with components engineered to withstand pressures exceeding 250 bar. This design also served as a foundation for a potential future transition to internal water cooling within the WILMA reaction chamber.

To evaluate the performance of these system upgrades, the physically implemented prototype depicted in Figure 26 was imported into an ANSYS simulation environment. The thermal simulations utilized process-relevant data, including coolant flow rates, material properties, and available heating power, to predict the temperature distribution of the setup under various operating conditions. Additionally, diverse scenarios involving variations in material thicknesses and configurations with multiple cooling connections were analyzed. Corresponding models are provided in the Appendix.

Thermal contact conditions of the implemented setup were calibrated using experimental data, recorded at dedicated measurement points. This calibration not only validated the simulation model but also provided reliable initial estimates of the heat transfer behavior and corresponding temperature gradients. The thermal simulation, validated for a heating table temperature of 420 °C, is presented in Figure 27.

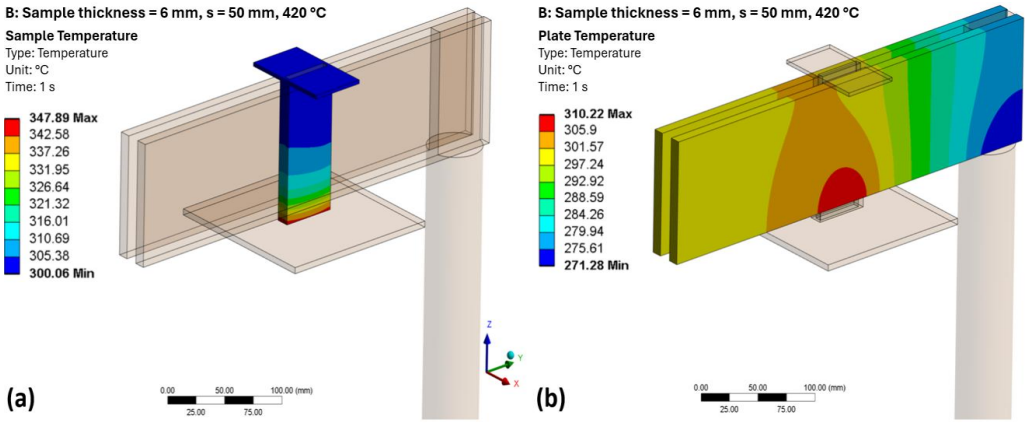


*Figure 27: ANSYS Temperature profile of the implemented Prototype setup with a heating table temperature of 420 °C. (a) Sample exterior. (b) Cooling plates.*

This thermal simulation confirmed that the desired initial temperature gradient, as described in the conceptual discussion in Section 12.2.3, could be achieved through the implemented modifications. According to the model, a considerable fraction of the sample remains below the critical reaction temperature threshold, while regions in proximity to the heat source exceed this limit. These preliminary investigations also demonstrated the feasibility of regulating an inert gas flow within the sample, hence validating the core functionality of the prototype configuration.

Nonetheless, the regulation of the precursor stream containing $WF_6$ and $H_2$ demanded further investigation, particularly over extended processing times. Furthermore, a comprehensive analysis of thermal contact fluctuations was not undertaken, as these parameters are known to vary significantly during the infiltration process. This underscores the inherent limitations of the model in reliably capturing such complex interactions over extended timescales, emphasizing the necessity for further experimental validation. Consequently, the subsequent section delineates the experimental procedure that was utilized to assess the feasibility of the proposed method under realistic operating conditions.

## 12.5 Experimental Procedure

Following the successful implementation of the prototype configuration and verification of the intended initial temperature distribution, the first CVI experiment was conducted. To ensure process safety and prevent condensation of corrosive gases on the reactor walls, the chamber dome was consistently maintained above a temperature of 120 °C. During the infiltration process, the external temperature of the sample was precisely controlled at 280 ± 10 °C for a total duration of 25 hours. In order to monitor the mass gain and to incrementally open the pluggable gas outlets, the reaction chamber was accessed on three occasions throughout the experiment.

To ensure complete reaction of residual $WF_6$ in the chamber and mitigate potential safety risks, the cooling system was deactivated during each chamber access. Consequently, the peripheral sample temperature temporarily exceeded the specified threshold during the bakeout process. Although the $WF_6$ flow was inactive during these intervals, it was anticipated that these precautionary measures might cause unintended CVD-W deposition at the sample's exterior.

In order to preserve the thermal stability of the sample during phases with activated precursor flow, it was necessary to operate the cooling system at its maximum capacity. Nevertheless, even this measure proved insufficient, necessitating frequent manual adjustments to the heating table temperature and absolute precursor volume flow rates to maintain the desired temperature range. A comprehensive overview of these adjustments, along with additional procedural details such as the precursor pressure profile over the course of the process, is provided in the Appendix.

This experimental procedure demonstrated that stable process conditions could be maintained throughout the entire infiltration run, with the $H_2$:$WF_6$ ratio consistently exceeding the target value of 12.5:1 at an absolute pressure of 95–105 mbar. Remarkably, this stability was achieved despite the inherent limitations of the prototype, such as limited cooling capacity and extended diffusion pathways created by the pluggable gas outlets.

The following section provides a more detailed evaluation of the concept, covering the changes to the setup, mass gain measurements, density distribution, mechanical performance, and the results of additional liquid metal infiltration trials with copper.

## 12.6 Concept Evaluation

Building on the insights gained from the experimental procedure, this chapter transitions to a critical evaluation of the proposed modified TG-CVI method and the developed prototype configuration, highlighting key observations and assessing its remaining limitations.

### 12.6.1 Experimental Setup

Figure 28 depicts the configuration of the CVI setup before and after the experiment. The presence of CVD-W deposits is clearly discernible in regions adjacent to the heat source, while no visible deposition is detected in areas closer to the external cooling system. This deposition pattern is primarily attributed to repeated chamber openings, as described in the previous chapter.

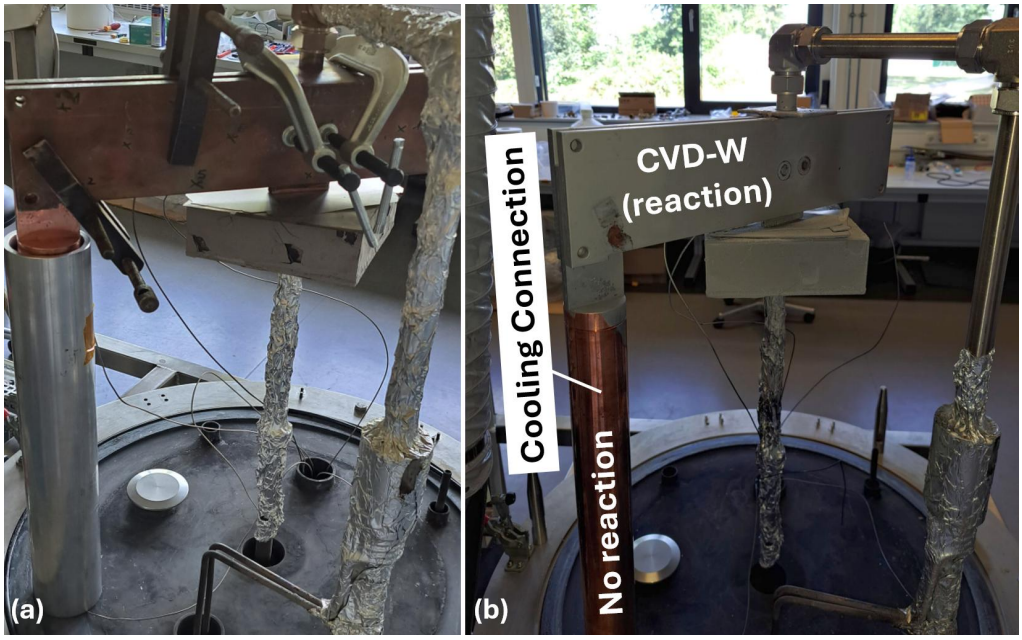


*Figure 28: Prototype CVI setup. (a) Configuration prior to the initial CVI experiment. (b) Configuration after the experiment, showing deposition effects on various components, including the cooling connection, and highlighting challenges posed by repeated chamber openings.*

### 12.6.2 Mass Gain Measurements

As outlined in Section 12.5, the chamber was periodically accessed for the purpose of monitoring the mass gain and incrementally opening the pluggable gas outlets. Given the necessity of reinstalling the assembly after each phase, it was not feasible to determine the mass of the specimen independently. Instead, the combined mass of the specimen including the copper shell was documented. The progression of infiltration was estimated based on this recorded total mass, utilizing the known values for the sample volume, fiber volume fraction, and densities of W-fibers and CVD-W as the matrix material, as summarized in Table 2.

*Table 2: CVI progress assessment via mass gain*

| Comments | Phase 1 | Phase 2 | Phase 3 | Unit |
|---|---|---|---|---|
| Process time per Batch | 7 | 5 | 13 | h |
| Sample Mass before Batch | 622,6 | 718,8 | 782,7 | g |
| Sample mass after Batch | 718,8 | 782,7 | 891,6 | g |
| CVD-W Mass Gain per Batch | 96,2 | 63,9 | 108,9 | g |
| General Mass Gain | 96,2 | 160,1 | 269,0 | g |
| CVI Progress / Estimate of relative Sample Density | 32,7% | 54,4% | 91,5% | - |

However, a precise understanding of the density distribution was only achievable after the removal of the copper shell, which is outlined in the following subsection.

### 12.6.3 Density Distribution

The density distribution of the fabricated $W_f$/W composite was analyzed by sectioning the produced material at multiple locations using electrical discharge machining (EDM). The cutting plan is detailed in the Appendix. Conventional density measurement methods, such as the Archimedes principle, proved unsuitable due to the residual porosity of the specimen. Consequently, the density was determined on the basis of the pixel density below a grayscale threshold in cross-sectional images.

Figure 29 illustrates the resulting density profile, highlighting successful fiber-crosslinking throughout the sample body. The relative density increased from an initial 56% before infiltration to a minimum of 79%, with values exceeding 97% in the lower hotter region, where the reaction was first initiated.

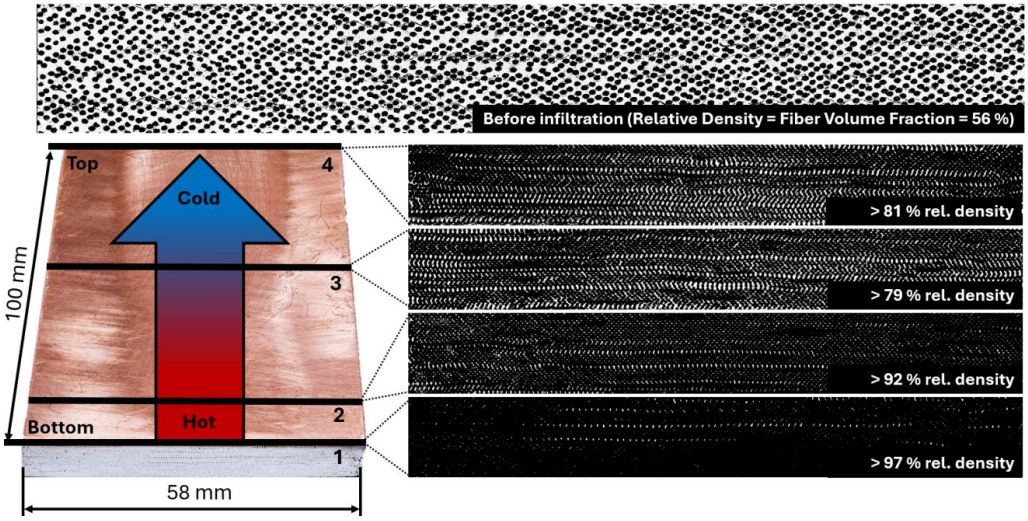


*Figure 29: Density profile of the Prototype CVI-$W_f$/W sample, highlighting consistent fiber-crosslinking.*

A detailed investigation of the density distribution revealed both progressive and cyclic fluctuations, predominantly caused by the alignment of textiles within the sample, as illustrated in Figure 30.

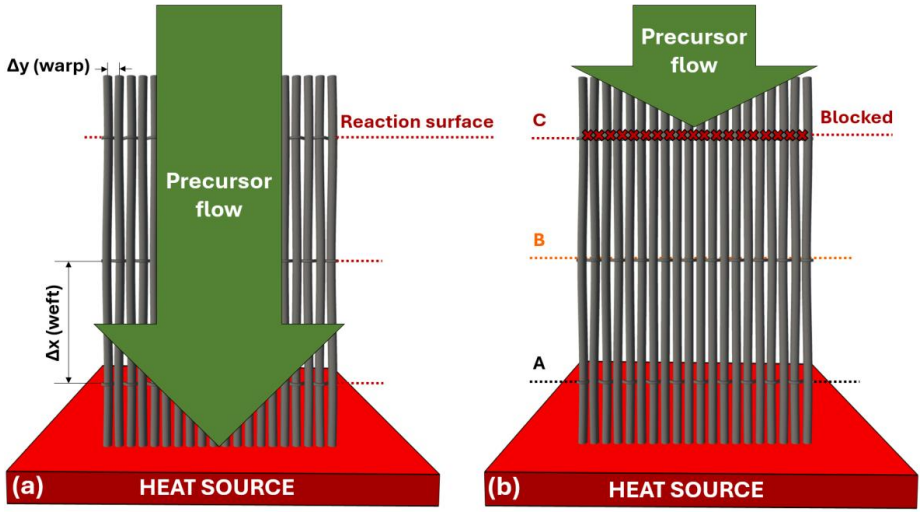


*Figure 30: Influence of textile orientation on material density for vertically oriented warp fibers. (a) shows the precursor flow at the beginning of the experiment, indicating the warp and weft spacing. (b) illustrates the formation of planes (A, B, and C), where premature blockages in plane C obstructed the flow to planes A and B, resulting in cyclical density variations.*

While the selected configuration successfully facilitated the investigation of precursor flow in process-relevant sample dimensions and allowed for a thorough evaluation of the underlying concept, it also revealed inherent limitations in producing a fully dense composite material.

The horizontal arrangement and progressive bridging of weft fibers led to the formation of discrete "planes" within the sample, labeled A, B, and C in Figure 30. The significantly higher weft to warp fiber spacing ratio (Δx = 2000 µm, Δy = 200 µm), coupled with insufficient vertical temperature gradients, led to premature blockages in the planes closer to the precursor inlet (Plane C). These blockages hindered the precursor flow to the lower planes (A and B) as the process continued.

These findings further contextualize the challenges in replicating the milestone reported by Riesch et al. in reference [311]. In contrast to the present study and prior CVI experiments conducted at the WILMA facility, their approach utilized individual W-filaments without the inclusion of weft fibers. Therefore, their design inherently avoided comparable blockage effects.

In general, four key factors were identified as contributors to the densification behavior of the composite through this method. These factors include the direction of precursor flow, the magnitude of temperature gradients, the orientation of textiles within the sample, and the potential deposition of CVD-W along the sample edges, which, in this case, was attributed to multiple chamber openings.

While these factors influence density distribution, the identified partially dense and partially porous microstructure presents intriguing opportunities for material optimization. In particular, the residual pores could serve as potential pathways for secondary material infiltration. Based on this consideration, the following subsection explores initial liquid metal infiltration trials with copper, focusing on how this method reduces residual porosity and may enhance its functional properties.

### 12.6.4 Liquid Metal Infiltration for Hybrid Composite Production

Drawing on insights from references [106, 217, 324, 325] and the observed material structure, an additional infiltration step with liquid copper was undertaken. Procedural details are provided in the Appendix. The primary objective was to reduce residual porosity, thereby creating a hybrid composite with a more uniform density distribution and potentially enhanced thermal conductivity.

Figure 31 illustrates the effectiveness of this approach. Liquid copper successfully infiltrated both highly porous regions (Figure 31a) and smaller pores in denser areas of the composite (Figure 31b), culminating in a fully densified material.

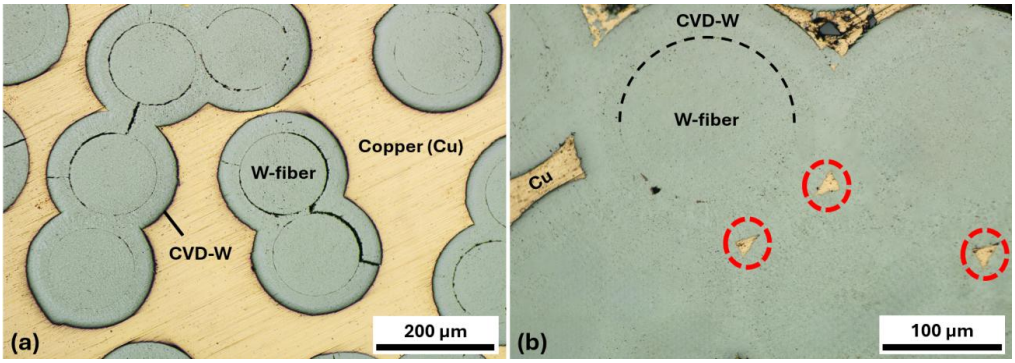


*Figure 31: Microscopic images of a $W_f$/W composite subsequent to liquid copper infiltration: (a) porous region illustrating extensive Cu infiltration around W-fibers and within the CVD-W matrix; (b) denser region highlighting localized Cu infiltration into small pores, indicated by red markers.*

Despite the success of this procedure in a small-scale specimen measuring 58 × 5 × 10 mm, the limited amount of synthesized material precluded a comprehensive evaluation of its material properties. In light of this constraint, mechanical testing was conducted on the remaining portion of the original CVI-$W_f$/W composite, enabling direct comparisons with previously fabricated materials and current industrial standards, as detailed in the following subchapter.

### 12.6.5 Mechanical Performance

To characterize the mechanical performance of the fabricated composite, KLST-type specimens were prepared via EDM for three-point bending tests. These tests were conducted using a TIRAtest 2820 (Model No. R050/01) in accordance with the DIN EN ISO 179-1:2000 standard, with a loading speed of 1 µm/s to ensure consistency with previously reported experimental conditions. Further experimental details, including specimen preparation and in situ imaging, are provided in the Appendix. The force-displacement behavior of the tested specimens is presented in Figure 32. The results reveal a characteristic pseudo-ductile fracture response, which initiates with a linear-elastic regime followed by a progressive load reduction beyond the peak force. This behavior indicates a notable capacity for energy dissipation during fracture, which contributes to the enhanced mechanical robustness of the material. Variations in mechanical response were observed, which can be attributed to differences in microstructural homogeneity and residual porosity, as discussed in earlier sections. Nevertheless, the consistent pseudo-ductile behavior across all tested specimens underscores the reliability of the fabricated CVI-$W_f$/W composite under bending loads.

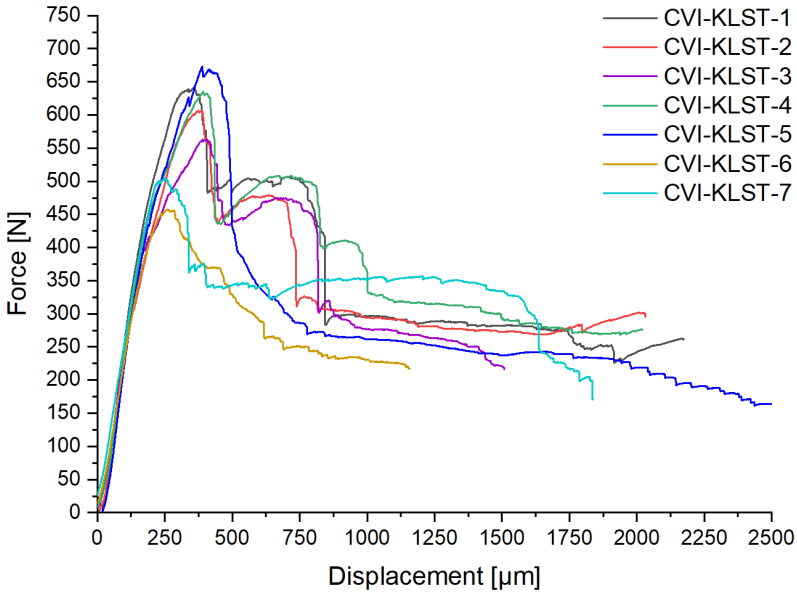


*Figure 32: Force-displacement curves of KLST-type specimens of CVI-$W_f$/W, illustrating variability in mechanical response due to residual porosity.*

In accordance with the protocol outlined in Publication [1], a remaining KLST specimen underwent cyclic mechanical loading to evaluate the material's behavior under dynamic stress conditions. Specifically, 10,000 loading-unloading cycles were applied within a load range of 200–400 N. As illustrated in Figure 33, the displacement response remained stable throughout the test, with minimal deviation. This outcome indicates excellent elastic recovery and negligible plastic deformation.

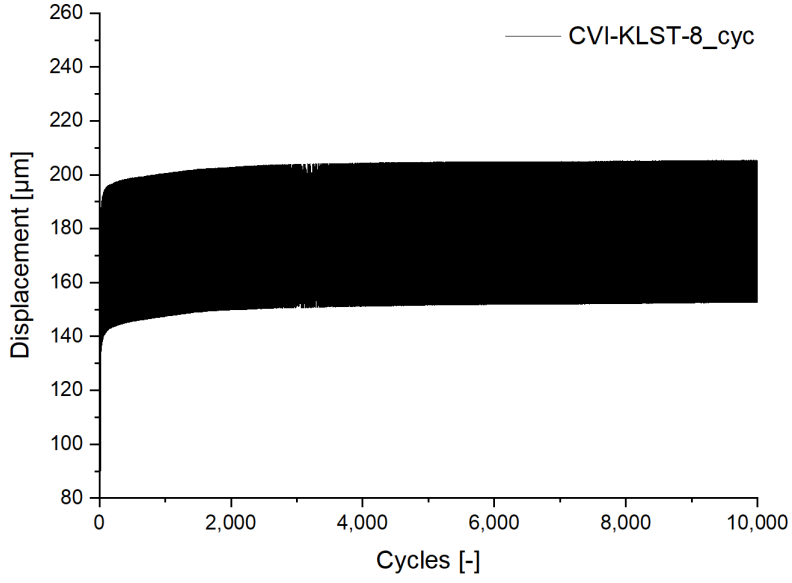


*Figure 33: Displacement response of a CVI-$W_f$/W specimen under cyclic mechanical loading between 200 N-400 N for 10,000 cycles, demonstrating stable deformation behavior over repeated loading-unloading cycles.*

To contextualize the performance of the CVI-derived $W_f/W$ composite, the mechanical properties of its best-performing specimen (CVI-KLST-5) were compared to those of yarn-based materials produced via the Batch-LPCVD method [1] and ITER-W, the current industrial standard.

As illustrated in Figure 34, the CVI-derived material (blue curve) demonstrates outstanding mechanical performance, with its fracture energy surpassing that of ITER-W (black curve) by more than two orders of magnitude. This pronounced capacity for energy absorption, largely attributable to the attained fiber volume fraction of 56%, establishes a new performance benchmark for $W_f/W$ composites.

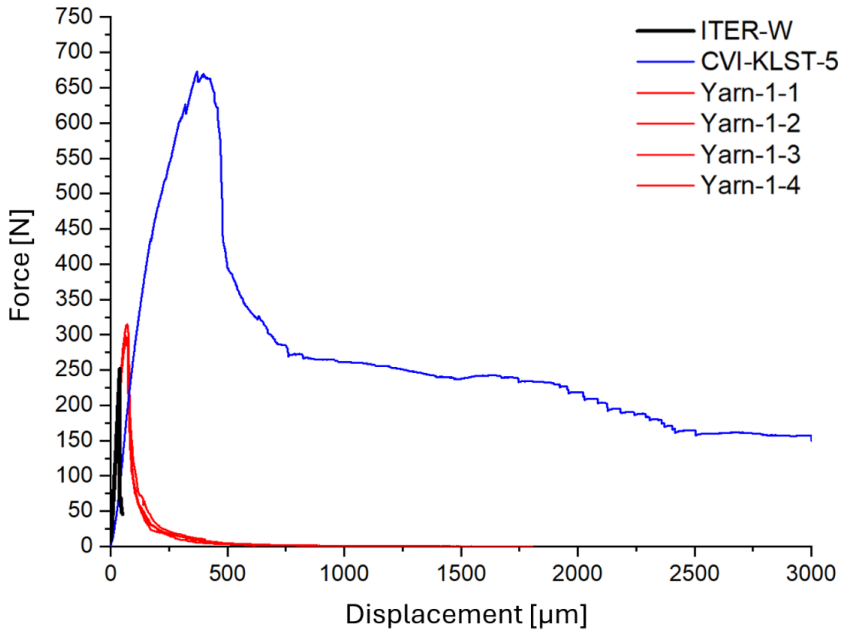


*Figure 34: Force-displacement curves for KLST-type specimens of yarn-based $W_f/W$ (Batch-LPCVD), single-fiber-based $W_f/W$ (CVI), and ITER-W, showcasing the performance gains achieved through CVI fabrication.*

Despite these advancements, the yarn-based material continues to demonstrate superior reproducibility, which remains a critical factor for commercial applications. Achieving the level of reliability reported in Publication [1] is therefore imperative. Given that relative densities exceeding 97% were achieved in the bottom sections of the prototype composite (evidenced in Figure 29), it is reasonable to anticipate that further enhancements in overall performance can be realized through additional process optimization steps.

While the successful validation of the CVI concept marks a significant milestone, several challenges remain. Key areas for improvement include reducing process variability, increasing production speed, ensuring recyclability, and refining densification control, all while enhancing the economic feasibility of the manufacturing process.

The following section outlines the conceptual evolution of the prototype into a more advanced CVI setup. This development directly addresses the identified limitations and is designed to enable the fabrication of $W_f/W$ composites with enhanced material properties, capable of meeting the stringent requirements of commercial applications, such as components for potential nuclear fusion reactors.

## 12.7 Transitioning to an Advanced CVI Configuration

Building upon the progressive approach outlined in Section 12.3, this chapter presents a sophisticated manufacturing concept aimed at addressing the residual limitations of the prototype configuration. The advanced setup integrates targeted enhancements to optimize temperature gradient control, refine precursor flow dynamics, and further enhance operational efficiency. The chapter commences with an introduction to the conceptual design, proceeds with a comprehensive description of the implementation process at the WILMA facility, and culminates in a presentation of the first experimentally validated thermal models. Finally, the chapter concludes with a critical evaluation of alternative textile configurations, providing a robust foundation for future investigations.

### 12.7.1 Conceptual Design

The proposed conceptual framework integrates a range of innovative features, the majority of which are illustrated in Figure 35 and further explored below.

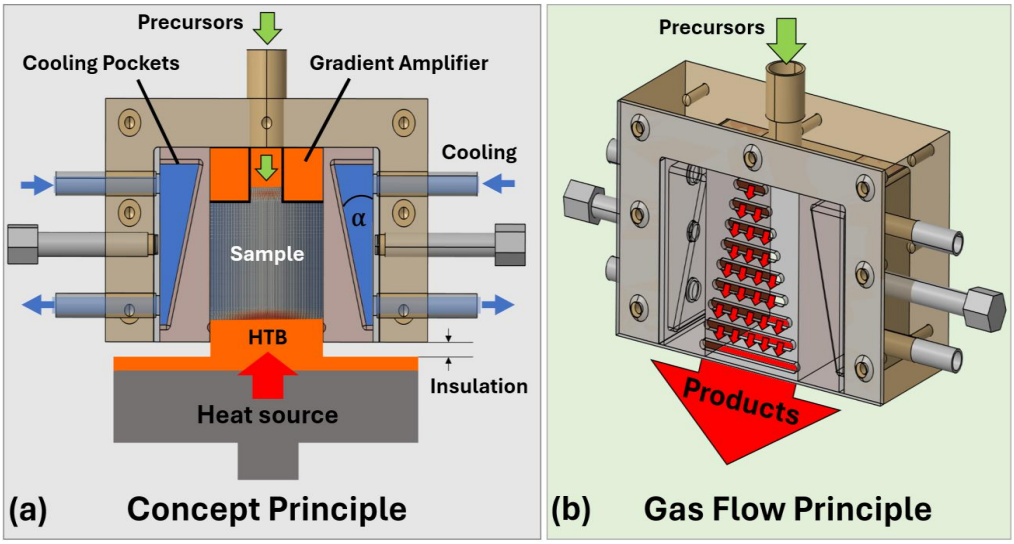


*Figure 35: Conceptual design of the advanced CVI setup. (a) Concept Principle: Cooling system with adjustable cooling pockets, gradient amplifier, heat transfer block (HTB) and an insulation layer. (b) Gas Flow Principle: Trapezoidal precursor flow layout for controlled infiltration and matrix growth.*

**1. Recyclable CVI Setup with Enhanced Cooling Capacity**

The advanced CVI configuration incorporates active water-cooling into the WILMA reaction chamber, utilizing movable cooling pockets and a support frame, both fabricated from high-temperature, fluorine-resistant AISI 314 steel alloy.

These components are meticulously engineered to ensure that the system can be readily recycled and adapted to evolving requirements. Each pocket features an adjustable angle (α), enabling precise adjustment of the coolant distance relative to the sample surface.

This cooling arrangement is thermally coupled to a customized copper gradient amplifier to address two remaining key challenges: significantly enhance the local heat transfer and enable refined control over the three-dimensional temperature gradient within the sample body. An additional purpose of this configuration is to improve the responsiveness of previously integrated automation system features (see Section 12.4). In the prototype setup, their effectiveness was limited by insufficient heat dissipation and delayed response times. The proposed adjustments aim to resolve these constraints, eliminating the need for frequent manual interventions and facilitating automated, extended infiltration runs in a single infiltration step.

**2. Trapezoidal Gas Flow with Edge Cooling**

The peripheral regions of the sample that are not directed toward the active cooling system are bordered by copper walls, which are arranged in a trapezoidal configuration to serve as a defined gas outlet. These elements are designed to direct precursor gases progressively toward the heated core, thereby eliminating the need for pluggable outlets and multiple chamber openings (see Section 12.5).

The walls are thermally connected to the cooling pockets, leveraging coppers' high thermal conductivity to cool the remaining edges of the sample. This approach has proven effective even for external cooling in the prototype design. Therefore, the setup is specifically tailored to prevent premature exterior sealing and ensure a consistent supply of precursors during extended infiltration periods. Technical drawings of the individual components are provided in the Appendix.

**3. Securing Scalability**

The advanced CVI configuration is specifically engineered to enable seamless upscaling to larger and more complex composite structures. Its modular architecture and adjustable components permit flexible adaptation to various cooling media and the generation of customized temperature gradients for specific sample dimensions. These aspects are considered essential for meeting the demands of industrial applications.

A notable advancement in this sophisticated concept is the incorporation of a heat transfer block (HTB), which facilitates the complete utilization of the thermal output from the available heat source. By increasing the energy input to the sample, the HTB is expected to reduce heating phases and enable higher core temperatures, ultimately reducing total production times. Moreover, the HTB enables precise modulation of the insulation layer height and fine-tuning of the system's energy balance, thereby enhancing operational versatility.

When integrated with automated process control and enhanced precursor flow dynamics, the system is devised to efficiently process samples with varying geometries. In its current configuration, developed and manufactured in collaboration with the Central Institute for Engineering (ZEA-1) at Forschungszentrum Jülich in Germany, it is designed to produce up to 300 layers of $W_f/W$ composites in diverse textile orientations. This capacity is determined solely by the geometrical dimensions of the reaction chamber and the available surface area of the localized heat source.

While the conceptual framework provides a robust foundation for further upscaling, it is not sufficient on its own to ensure safe operation. The successful integration of the setup into a chemical process environment, such as the WILMA facility, required additional modifications and safety measures, which are systematically detailed in the following subchapter.

### 12.7.2 Practical Implementation of the Advanced CVI Setup

As discussed in Section 12.3, the integration of water as a coolant into the WILMA reaction chamber poses considerable safety concerns. This chapter directly addresses these risks and details the modifications implemented to guarantee the safe and reliable operation of the facility, including the advanced CVI setup.

#### 1. Identification and Testing of Critical Components

The first essential step was to identify the most critical components and verify their functionality under modified operating conditions. Particular attention was directed toward welded structures, including the chamber connection and cooling pockets. Recognized as the most critical elements, the cooling pockets underwent structural integrity testing based on DIN EN 13445-3 principles prior to fabrication. Following successful validation, the components were fabricated and further evaluated under process-relevant pressures. To guarantee comprehensive structural reliability, all welded parts underwent helium leak testing at a sensitivity threshold below $10^{-8}$ mbar·l/s prior to installation. Comprehensive reports are available in the Appendix.

#### 2. Integration of the Internal Coolant Circuit

Upon successful completion of these qualification procedures, the external coolant circuit, pre-designed for elevated process pressures (see Section 12.4), was further expanded and coupled to the CVI system via the chamber connection part. Figure 36 provides a visual representation of these modifications and offers a comprehensive schematic of the principal design elements of the WILMA reaction chamber subsequent to the installation of the advanced CVI setup.

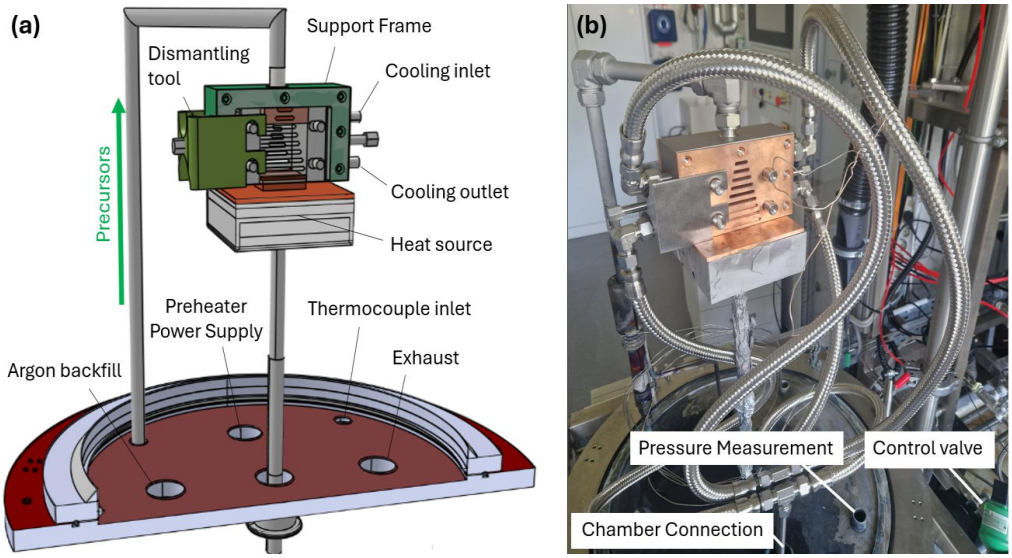


*Figure 36: (a) Schematic representation of the advanced CVI setup, highlighting the key features, including a specialized dismantling tool. (b) Photograph of the implemented configuration, providing a comprehensive overview of the modified facility.*

**3. Implementation of Safety Enhancements**

In addition to the extensive modifications and testing procedures described earlier, further enhancements were implemented to ensure the system's safe and reliable performance under varying thermal, chemical, and physical stress conditions.

Among these, the installation of a manual coolant outlet was identified as a critical safety feature. This outlet facilitates the controlled drainage of coolant prior to the system's baking process (refer to the protocol in Section 12.5). To prevent backflow during drainage and ensure proper operation, a non-return valve was integrated into the outlet line. Together, these measures effectively eliminate residual coolant during critical operational phases and mitigate the risk of pressure build-up caused by potential phase transitions. To further safeguard the system, an overflow valve was incorporated as a fail-safe mechanism, automatically relieving excess pressure and protecting the system from potential damage in the event of unexpected surges.

Enhancements to process control were also introduced. These modifications include advanced monitoring capabilities to track coolant temperature, circulation rates, and energy input into the system. By providing real-time feedback on critical parameters, these additions enable precise operational adjustments, improving system reliability and ensuring consistent performance under dynamic conditions. Detailed descriptions of these enhancements and their implementation are provided in the Appendix.

With these modifications in place, the upgraded system was subjected to preliminary testing under an inert gas atmosphere to verify its core functionality and operational safety. Maximum operating temperatures and flow rates were applied, with the cooling system operating at full capacity. These tests successfully confirmed the reliable operation of the facility under high-stress conditions and provided a comprehensive dataset for validating the thermal modeling results, which are presented in the following subsection.

### 12.7.3 Thermal Modelling

To establish a foundation for optimizing process parameters and operational protocols in future infiltration trials with activated precursor flow, a detailed thermal model was developed and validated using the experimental data outlined in the previous section. This modeling approach builds directly on the ANSYS methodology described in Chapter 12.4, leveraging its robust framework to simulate temperature distributions within the modified setup. The complete dataset of boundary conditions and material parameters used in the model is documented in the Appendix.

Figure 37 provides a comprehensive overview of the experimentally validated temperature profiles of the advanced setup. Panel (a) illustrates the cross-sectional temperature profile through the center of the sample, clearly demonstrating the significant impact of coolant distance variations on the temperature gradient from the interior to the exterior. Furthermore, the model highlights the interaction between the cooling pockets and the HTB (refer to Figure 35), emphasizing their combined effect on the temperature distribution in the sample body.

Panel (b) presents a three-dimensional visualization of the sample’s temperature distribution, scaled between 300 °C and 800 °C. Blue regions correspond to areas below the reaction threshold, while higher-temperature zones identify regions conducive to significant CVD-W growth.

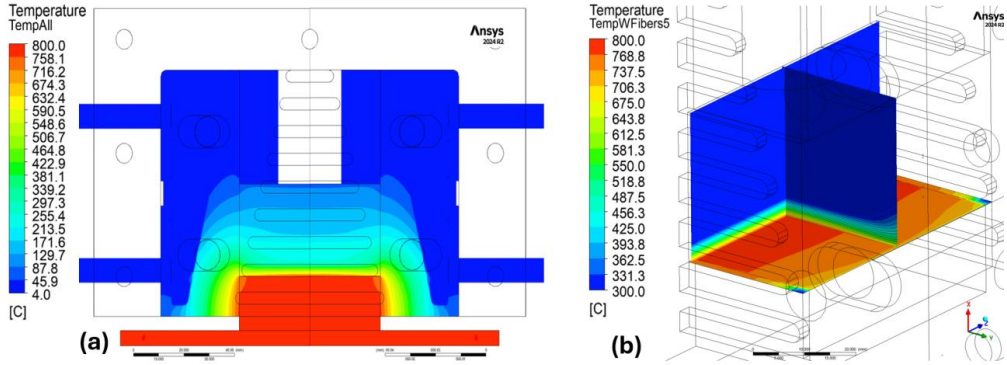


*Figure 37: Experimentally validated ANSYS Temperature profile of the implemented Prototype setup with a heating table temperature of 800 °C prior to infiltration: (a) Cross-sectional temperature profile; (b) three-dimensional temperature profile, highlighting the initial temperature profile at the bottom core and strong temperature gradients.*

This visualization elucidates the thermal environment within the sample and reinforces the utility of the model in predicting growth zones and optimizing precursor distribution.

Despite the substantially elevated heating table temperature of 800 °C, in comparison to the prototype's 420 °C, the system effectively maintained controlled thermal gradients across the sample. These results validate the configuration's potential to support a uniform precursor supply, enabling controlled and predictable matrix growth.

These results validate the system's capacity for precise thermal management, potentially enabling uniform precursor distribution and predictable CVD-W growth behavior.

The thermal model, however, assumes an anisotropic fiber structure with material properties dependent on fiber orientation, making its results intrinsically tied to the textile configuration. Given that fiber arrangements can significantly influence precursor distribution and matrix densification, their impact on the infiltration process warrants detailed examination. The next chapter addresses this by exploring alternative textile configurations aimed at improving performance, reducing process times, and ensuring higher composite densities.

### 12.7.4 Alternative Textile Configurations

Based on findings from previous CVI experiments, the total duration of the infiltration process is predominantly governed by the time required to seal the sample's outer edges. The resulting density of the composite material, on the other hand, is primarily dictated by the intricate interplay between the applied temperature gradient and the fiber arrangement within the composite. This dependency presupposes that the infiltration proceeds uninterrupted until completion.

Although an infinitely large temperature gradient could theoretically eliminate the influence of fiber orientation by promoting quasi-punctual CVD-W matrix growth, such an approach is not practical or industrially scalable due to prohibitively long processing times. Consequently, optimizing the CVI process necessitates a comprehensive evaluation of fiber arrangements to attain higher composite densities while achieving higher production throughput. The established textile manufacturing techniques outlined in Section 3.2 hold considerable promise for tailoring the fiber layout.

A promising avenue for further process optimization involves increasing the spacing between weft fibers (Δx), as illustrated in the previously employed configuration depicted in Figure 30. Provided that both the temperature gradient and sample dimensions remain consistent, this modification is expected to prevent premature clogging of precursor pathways and thereby enable the formation of a fully dense $W_f/W$ composite. Alternatively, instead of adjusting the base textiles themselves, the orientation of these textiles could be tailored within the advanced CVI setup.

The introduction of fibers or planes arranged transversely to the precursor inlet does not inherently create problems; issues arise only when pores in regions near the precursor inlet seal prematurely, restricting precursor access to areas further downstream. To mitigate this risk, the existing base textiles, which possess a large weft-to-warp spacing ratio (see Section 12.6.3), may be used to accelerate CVD-W growth from the heat source toward the precursor inlet.

Since the sealing duration under equivalent processing conditions is precisely ten times longer, it is plausible that, with meticulous process control and sufficiently strong temperature gradients, high material densities could be achieved within significantly shorter processing intervals. However, this hypothesis necessitates experimental validation. In light of these considerations, Figure 36 proposes two textile configurations that illustrate this approach. These alignments aim to balance process duration with achieving the desired material properties, ultimately contributing to the industrial applicability of the CVI method.

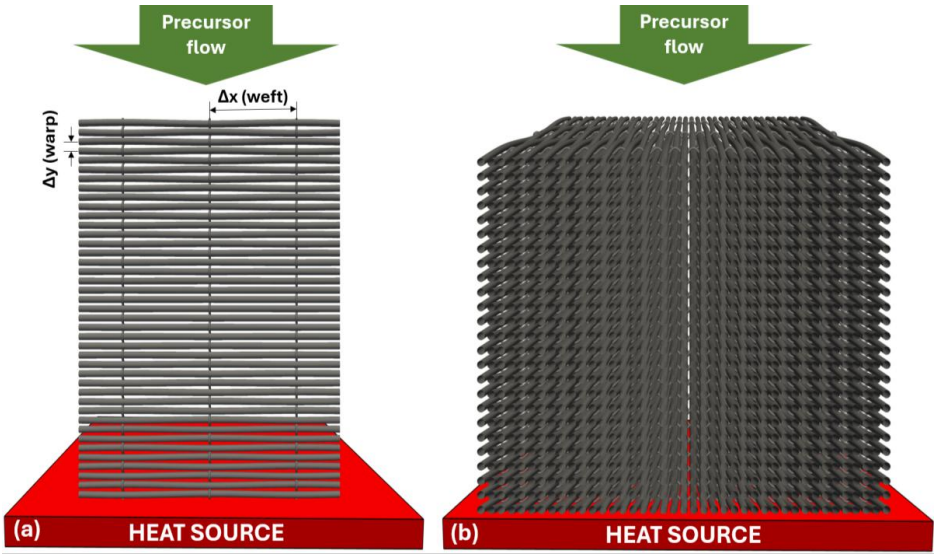


*Figure 38: Proposed alternative textile alignments to leverage transverse planes as additional reaction surfaces for process optimization: (a) vertically aligned weft fibers; (b) flat configuration with horizontal alignment of warp and weft fibers.*

These developments, encompassing both the enhancements made to the existing setup and the exploration of alternative textile configurations, lay a strong foundation for further optimizing the CVI process. By integrating the lessons learned from practical implementation with novel fiber arrangements, the findings of this study contribute to advancing scalable and efficient production strategies for $W_f/W$ composites. The subsequent chapter provides a conclusive assessment of these efforts, outlining their implications for future research and industrial application.

# 13 Conclusive Assessment and Future Directions

The findings of this dissertation underscore the significant potential of W-fibers as reinforcing elements in high-performance composite materials, particularly for advanced nuclear fusion reactors. A comprehensive evaluation of various production methodologies has demonstrated the feasibility of scaling up these materials via CVD-based techniques while addressing critical challenges related to process efficiency, mechanical performance, and economic viability. The in-depth analysis conducted in this study provides valuable insights into the fundamental process dynamics, establishing a robust foundation for transitioning from laboratory-scale developments to commercial production.

This chapter presents a conclusive assessment of the investigated production strategies, outlining their strengths and limitations, and proposes key strategic directions for future research. These recommendations aim to further enhance the scalability, performance and cost-effectiveness of WFRCs in specific applications.

## 13.1 Final Evaluation of the Production Concepts

This section provides a comprehensive assessment of the four primary production concepts explored in this dissertation – Batch-LPCVD, the hybrid method, Continuous CVD (FRED), and CVI. Each method offers distinct advantages and faces specific challenges, which are summarized below.

### 13.1.1 Batch-LPCVD

The Batch-LPCVD process has played a pivotal role in advancing $W_f$/W composite production by providing precise control over the deposition characteristics of CVD-W. This level of control has enabled the fabrication of composites exhibiting pseudo-ductile fracture behavior and predictable fatigue performance, as demonstrated in Publications [1]. However, despite its significance in proof-of-concept studies, the scalability of this method is severely limited by inherent inefficiencies, including prolonged production times and high maintenance demands. As a result, its feasibility for large-scale composite production remains impractical. Nonetheless, the insights gained from this process have contributed to the establishment of a robust coating methodology, capable of accommodating a variety of substrates with differing layer thicknesses, provided they can withstand the required processing temperatures.

### 13.1.2 Hybrid Method

The hybrid approach, presented in Publication [2], which combines Batch-LPCVD with Spark Plasma Sintering (SPS), represents the most versatile of the investigated production approaches. It offers significant application potential by enhancing the structural integrity of W-fibers and the ceramic interface during the sintering process across a wide range of matrix materials. Its high adaptability makes it particularly attractive for use in advanced ceramics and metallic alloys, thereby expanding the scope of W-fiber reinforcement to materials with diverse chemical and thermal properties. However, further research is required to optimize process parameters for specific matrix characteristics and to facilitate industrial implementation.

For the production of $W_f$/W composites, however, the hybrid method presents considerable challenges. In particular, its incompatibility with W-yarns limits design flexibility and reduces the range of possible composite architectures. Additionally, composites produced using this method tend to exhibit lower relative densities and reduced mechanical properties compared to those manufactured exclusively through CVD-based techniques, which continue to set the benchmark for reliability.

### 13.1.3 Continuous CVD (FRED System)

The continuous CVD method, discussed in Chapter 11, was proposed as a potential solution to the limitations of the Batch-LPCVD process by enabling continuous production and improving coating uniformity across the W-textile feed. The FRED (For Rotary Enhanced Deposition) system, integrated into the existing WILMA facility, was specifically designed to enhance deposition homogeneity through the combination of a rotating, heatable composite tube and a gas shield that prevents premature precursor deposition. However, despite initial indications of feasibility, further investigations revealed significant technical challenges, such as non-uniform coating distribution, increased maintenance complexity, and constraints related to material selection. The method's reliance on highly flexible base materials further limits its adaptability and introduces additional residual stresses. Consequently, the continuous CVD approach does not fulfill the essential requirements for scalability and performance, making its industrial implementation unsuitable at this stage.

### 13.1.4 Chemical Vapor Infiltration (CVI)

Chemical Vapor Infiltration (CVI), examined in detail in Chapter 12, has emerged as the most promising approach for scaling $W_f$/W composite production to industrial levels. The modified TG-CVI process developed in this work successfully addresses key infiltration challenges, achieving relative densities exceeding 97% in critical regions and fracture energies surpassing current industrial standards by two orders of magnitude.

These findings highlight the potential of CVI technology for the fabrication of high-performance composites with exceptional mechanical properties and structural integrity. Beyond demonstrating feasibility and establishing new performance benchmarks, the composite structure achieved in the prototype (Figure 31) provides a promising foundation for further exploration of advanced component designs, as outlined in references [5, 106-108]. As discussed in Chapter 2.1.4, current monoblock designs represent a compromise solution to address the challenges associated with joining W to other materials, ensuring safe operation in both Tokamaks and Stellarators (Figure 1).

The partially porous, partially dense composite structure observed in this work offers a potential pathway to addressing these challenges. With further refinement and validation, this approach could contribute to the evolution of novel design strategies that may reduce the manufacturing complexity of plasma-facing components (PFCs) while maintaining or potentially enhancing their mechanical performance. However, factors such as hydrogen retention or thermal conductivity of the materials must be critically evaluated to ensure reliable performance under fusion-relevant conditions. As outlined in Chapter 2.2 of this work, the properties of W must be enhanced in all aspects to guarantee long-term operation.

## 13.2 Future Directions

The continued advancement of WFRCs demands a focused effort to address several key challenges and capitalize on emerging opportunities. While substantial progress has been achieved in their production and scalability, a thorough understanding of their long-term performance under fusion-relevant conditions remains crucial. Further characterization is essential to evaluate their mechanical stability and thermal resilience over extended operational periods, ensuring their reliability in practical applications.

A key priority moving forward is the refinement of the CVI process, as outlined in Chapter 12.7. Although recent modifications have enhanced deposition efficiency and material properties, extensive testing is still required to verify its reliability. Additional improvements in process control and scalability will be critical to achieving consistent quality and ensuring economic feasibility for large-scale applications.

Furthermore, the hybrid approach offers a compelling opportunity to broaden the potential applications of WFRCs. Investigating the integration of alternative matrix materials could improve their adaptability to a wider range of industrial requirements, thereby streamlining commercialization and facilitating their adoption across various sectors.

Simultaneously, with current production capacity nearing its operational limits, the development of an upgraded CVD / CVI system – *WILMA 2.0* – has become increasingly imperative. Expanding the processing infrastructure will not only mitigate existing constraints but also support the transition from laboratory-scale production to full industrial implementation, resulting in higher throughput and enhanced process efficiency.

Effectively addressing these challenges will require sustained collaboration between research institutions and industry stakeholders. Efforts should prioritize the optimization of processing technologies, the establishment of standardized qualification protocols, and the promotion of innovation to drive further advancements in WFRC production.

# 14 Final Remarks

The findings of this thesis establish a robust foundation for bridging the gap between laboratory research and industrial demands in the large-scale production of WFRCs. The methodologies and strategies outlined emphasize the considerable potential of these composites, with $W_f$/W emerging as a particularly promising candidate for deployment in extreme environments, such as those encountered in nuclear fusion rectors.

The successful industrial implementation of WFRCs requires a comprehensive approach that meticulously balances technical and economic considerations. Strategic investments in production infrastructure and process optimization will be pivotal in overcoming existing challenges and enabling large-scale adoption. Moreover, sustained collaboration across disciplines and industries will be crucial in fostering innovation and accelerating commercialization efforts.

By harnessing interdisciplinary expertise and embracing a forward-looking approach, WFRCs hold the potential to drive transformative advancements in future technologies, contributing significantly to progress in energy systems, aerospace, and other high-performance applications.

# Table of Figures

# Table of Tables

# List of Symbols and Abbreviations

| Symbol | Explanation |
|---|---|
| ${}^{1}n$ | Neutron |
| ${}^{4}_{2}He$ | Helium |
| $\mathrm{D} \triangleq {}^{2}_{1}H$ | Deuterium |
| $\mathrm{T} \triangleq {}^{3}_{1}H$ | Tritium |
| c | Speed of light |
| CTE | Coefficient of Thermal Expansion |
| CVD | **C**hemical **V**apor **D**eposition |
| CVI | **C**hemical **V**apor **I**nfiltration |
| DBTT | **D**uctile to **B**rittle **T**ransition **T**emperature |
| dpa | **D**isplacement **p**er **a**tom |
| E | Energy |
| EDM | **E**lectrical **D**ischarge **M**achining |
| $H_2$ | Hydrogen |
| $k_0$, $k_1$, $k_2$ | Constants for deposition rate equations $[\mathrm{ms}^{-1}\mathrm{Pa}^{-(\mathrm{n}_{\mathrm{H}_2}+\mathrm{n}_{\mathrm{WF}_6})}]$ |
| m | Mass in kg |
| n | Reaction order [-] |
| PFC | **P**lasma **f**acing **c**omponent |
| PM | **P**owder **m**etallurgical **m**anufacturing |
| $\dot{V}_{H_2O}$ | Volume flow of cooling water |
| $WF_6$ | Tungsten hexafluoride |
| WFRCs | Tungsten fiber-reinforced composites |
| $W_fW$ | Tungsten fiber-reinforced Tungsten |
| WILMA | Tungsten (**W**) **I**nfil**l**tration **Ma**chine |
| W | Tungsten |
| $WO_3$ | Tungsten oxide |

# Literature

[1] A. Lau, J.W. Coenen, D. Schwalenberg, Y.R. Mao, T. Höschen, J. Riesch, L. Raumann, M. Treitz, H. Gietl, A. Terra, B. Göhts, C. Linsmeier, K. Theis-Bröhl, J. Gonzalez-Julian, Bulk Tungsten Fiber-Reinforced Tungsten (Wf/W) Composites Using Yarn-Based Textile Preforms, Journal of Nuclear Engineering 4(2) (2023) 375-390.

[2] A. Lau, Y.R. Mao, R. Shu, J.W. Coenen, M. Poll, C. Linsmeier, J. Gonzalez-Julian, Combining Chemical Vapor Deposition and Spark Plasma Sintering for the Production of Tungsten Fiber-Reinforced Tungsten (Hybrid - Wf/W), Adv Eng Mater (2024).

[3] J.W. Coenen, P. Huber, A. Lau, L. Raumann, D. Schwalenberg, Y. Mao, J. Riesch, A. Terra, C. Linsmeier, R. Neu, Tungsten fiber reinforced tungsten (Wf/W) using yarn-based textile preforms, Phys Scripta 96(12) (2021).

[4] D. Schwalenberg, J.W. Coenen, J. Riesch, T. Hoeschen, Y. Mao, A. Lau, H. Gietl, L. Raumann, P. Huber, C. Linsmeier, R. Neu, Large-Scale Tungsten Fibre-Reinforced Tungsten and Its Mechanical Properties, Journal of Nuclear Engineering 3(4) (2022) 306-320.

[5] J. Riesch, A. von Müller, Y. Mao, J.W. Coenen, B. Böswirth, S. Elgeti, M. Fuhr, H. Greuner, T. Höschen, K. Hunger, P. Junghanns, A. Lau, S. Roccella, L. Vanlitsenburgh, J.H. You, C. Linsmeier, R. Neu, Progress in the development of industrial scale tungsten fibre-reinforced composite materials, Nucl Mater Energy 38 (2024).

[6] R. Shu, Y.R. Mao, A. Lau, J.W. Coenen, A. Terra, C. Liu, J. Riesch, C. Linsmeier, C. Broeckmann, Effect of the heating rate and Y2O3 coating on the microstructure of Wf/ Y2O3/W composites via field assisted sintering technology, Nucl Mater Energy 38 (2024).

[7] J.W.C. A. Lau, P. Huber, J. Riesch, Y. Mao, S. Schönen, D. Hintzen, , A.K. T. Höschen, A. Terra, Ch. Linsmeier, J. Gonzalez-Julian, Exceptionally pseudo-ductile tungsten-fiber-reinforced tungsten manufactured via chemical vapor infiltration, (2025).

[8] R.E. Hummel, Understanding Materials Science, 1998.

[9] T.A. Wertime, The Beginnings of Metallurgy: A New Look, Science 182(4115) (1973) 875-887.

[10] D. Constantinescu, B.A. Cârlan, A Short History of the Iron and Steel Industry in Central Europe during the Roman Iron Age, Metal 2016: 25th Anniversary International Conference on Metallurgy and Materials (2016) 72-77.

[11] F. Uekoetter, Enriching the Earth. Fritz Haber, Carl Bosch, and the Transformation of World Food Production. By Vaclav Smil. Cambridge, Massachusetts, London, England: The MIT Press, 2001. xvii + 338 pp. Illustrations, appendixes, notes, index. $34.95, Environmental History 7(3) (2002) 532-533.

[12] J.C. Ince, M. Peerzada, L.D. Mathews, A.R. Pai, A. Al-qatatsheh, S. Abbasi, Y. Yin, N. Hameed, A.R. Duffy, A.K. Lau, N.V. Salim, Overview of emerging hybrid and composite materials for space applications, Adv Compos Hybrid Ma 6(4) (2023).

[13] J. Wu, W. Pisula, K. Müllen, Graphenes as Potential Material for Electronics, Chemical Reviews 107(3) (2007) 718-747.

[14] F.F. Wang, Y.Z. Cao, C. Chen, Q. Chen, X. Wu, X.G. Li, T.S. Qin, W. Huang, Materials toward the Upscaling of Perovskite Solar Cells: Progress, Challenges, and Strategies, Adv Funct Mater 28(52) (2018).

[15] M. Sarvghad, S.D. Maher, D. Collard, M. Tassan, G. Will, T.A. Steinberg, Materials compatibility for the next generation of Concentrated Solar Power plants, Energy Storage Mater 14 (2018) 179-198.

[16] M.S. Baltatu, P. Vizureanu, A.V. Sandu, N. Florido-Suarez, M.V. Saceleanu, J.C. Mirza-Rosca, New Titanium Alloys, Promising Materials for Medical Devices, Materials 14(20) (2021) 5934.

[17] I. Tirotta, V. Dichiarante, C. Pigliacelli, G. Cavallo, G. Terraneo, F.B. Bombelli, P. Metrangolo, G. Resnati, F Magnetic Resonance Imaging (MRI): From Design of Materials to Clinical Applications, Chemical Reviews 115(2) (2015) 1106-1129.

[18] J. Linke, J. Du, T. Loewenhoff, G. Pintsuk, B. Spilker, I. Steudel, M. Wirtz, Challenges for plasma-facing components in nuclear fusion, Matter Radiat Extrem 4(5) (2019).

[19] D. Uglietti, N. Bykovsky, R. Wesche, P. Bruzzone, Development of HTS Conductors for Fusion Magnets, Ieee T Appl Supercon 25(3) (2015).

[20] I. Charit, K.L. Murty, Structural Materials Issues for the Next Generation Fission Reactors, Jom-Us 62(9) (2010) 67-74.

[21] S.J. Zinkle, J.T. Busby, Structural materials for fission & fusion energy, Materials Today 12(11) (2009) 12-19.

[22] e.b.G.V.O. IAEA, Fundamentals of Magnetic Fusion Technology, INTERNATIONAL ATOMIC ENERGY AGENCY, Vienna, 2023.

[23] P.O. A. Aasen, Nuclear Reactors, Nuclear Fusion and Fusion Engineering, Nuclear Reactors, Nuclear Fusion and Fusion Engineering (2009) 1-484.

[24] R.W. Conn, J.P. Holdren, S. Sharafat, D. Steiner, D.A. Ehst, W.J. Hogan, R.A. Krakowski, R.L. Miller, F. Najmabadi, K.R. Schultz, Economic, safety and environmental prospects of fusion reactors, Nucl Fusion 30(9) (1990) 1919.

[25] S. Matsuda, K. Tobita, Evolution of the ITER program and prospect for the next-step fusion DEMO reactors: status of the fusion energy R&D as ultimate source of energy, J Nucl Sci Technol 50(4) (2013) 321-345.

[26] D. Stork, P. Agostini, J.L. Boutard, D. Buckthorpe, E. Diegele, S.L. Dudarev, C. English, G. Federici, M.R. Gilbert, S. Gonzalez, A. Ibarra, C. Linsmeier, A.L. Puma, G. Marbach, L.W. Packer, B. Raj, M. Rieth, M.Q. Tran, D.J. Ward, S.J. Zinkle, Materials R&D for a timely DEMO: Key findings and recommendations of the EU Roadmap Materials Assessment Group, Fusion Engineering and Design 89(7-8) (2014) 1586-1594.

[27] H. Bolt, V. Barabash, W. Krauss, J. Linke, R. Neu, S. Suzuki, N. Yoshida, A.U. Team, Materials for the plasma-facing components of fusion reactors, J Nucl Mater 329 (2004) 66-73.

[28] S.A. J.W. Coenen, M. Aumann, W. Biel, J. Du, J. Engels,, A.H. S. Heuer, T. Hoeschen, B. Jasper, F. Koch, J. Linke,, Y.M. A. Litnovsky, R. Neu, G. Pintsuk, J. Riesch, M. Rasinski,, M.R. J. Reiser, A. Terra, B. Unterberg, Th. Weber, T. Wegener,, J.-H.Y.a.C. Linsmeier, Materials for DEMO and reactor applications

- boundary conditions and new concepts, (2015).

[29] R. Wenninger, R. Albanese, R. Ambrosino, F. Arbeiter, J. Aubert, C. Bachmann, L. Barbato, T. Barrett, M. Beckers, W. Biel, L. Boccaccini, D. Carralero, D. Coster, T. Eich, A. Fasoli, G. Federici, M. Firdaouss, J. Graves, J. Horacek, M. Kovari, S. Lanthaler, V. Loschiavo, C. Lowry, H. Lux, G. Maddaluno, F. Maviglia, R. Mitteau, R. Neu, D. Pfefferle, K. Schmid, M. Siccinio, B. Sieglin, C. Silva, A. Snicker, F. Subba, J. Varje, H. Zohm, The DEMO wall load challenge, Nucl Fusion 57(4) (2017).

[30] I. Burgués-Ceballos, M. Stella, P. Lacharmoise, E. Martínez-Ferrero, Towards industrialization of polymer solar cells: material processing for upscaling, J Mater Chem A 2(42) (2014) 17711-17722.

[31] S.T. Williams, A. Rajagopal, C.C. Chueh, A.K.Y. Jen, Current Challenges and Prospective Research for Upscaling Hybrid Perovskite Photovoltaics, J Phys Chem Lett 7(5) (2016) 811-819.

[32] A. Sharma, D. Ramacharyulu, S. Lakhanpal, H. Ghafel, U. Reddy, V. Kumari, Exploring the Future of Advanced Materials Processing: Innovations and Challenges Ahead: A Review, E3S Web of Conferences 505 (2024) 01021.

[33] J. Riesch, M. Fuhr, J. Almanstoetter, Tungsten Wire-From Lamp Filaments to Reinforcement Fibers for Composites in Fusion Reactors, Adv Eng Mater (2024).

[34] C. Linsmeier, M. Rieth, J. Aktaa, T. Chikada, A. Hoffmann, J. Hoffmann, A. Houben, H. Kurishita, X. Jin, M. Li, A. Litnovsky, S. Matsuo, A. von Muller, V. Nikolic, T. Palacios, R. Pippan, D. Qu, J. Reiser, J. Riesch, T. Shikama, R. Stieglitz, T. Weber, S. Wurster, J.H. You, Z. Zhou, Development of advanced high heat flux and plasma-facing materials, Nucl Fusion 57(9) (2017).

[35] J.W. Coenen, Y. Mao, J. Almanstotter, A. Calvo, S. Sistla, H. Gietl, B. Jasper, J. Riesch, M. Rieth, G. Pintsuk, F. Klein, A. Litnovsky, A.V. Mueller, T. Wegener, J.H. You, C. Broeckmann, C. Garcia-Rosales, R. Neu, C. Linsmeier, Advanced materials for a damage resilient divertor concept for DEMO: Powder-metallurgical tungsten-fibre reinforced tungsten, Fusion Engineering and Design 124 (2017) 964-968.

[36] J. Riesch, Y. Han, J. Almanstötter, J.W. Coenen, T. Höschen, B. Jasper, P. Zhao, C. Linsmeier, R. Neu, Development of tungsten fibre-reinforced tungsten composites towards their use in DEMO—potassium doped tungsten wire, Phys Scripta T167 (2016).

[37] D.L. McDanels, Tungsten fiber reinforced copper matrix composites: a review, National Aeronautics and Space Administration, Office of Management, Scientific and Technical Information Division, Washington, D.C., 1989.

[38] Y. Jiang, L.H. Zhang, Q.F. Fang, T. Zhang, X.P. Wang, T. Hao, C.S. Liu, Toughness enhancement of tungsten reinforced with short tungsten fibres, Materials Science and Engineering: A 690 (2017) 208-213.

[39] J.W. Coenen, Y. Mao, S. Sistla, J. Riesch, T. Hoeschen, C. Broeckmann, R. Neu, C. Linsmeier, Improved pseudo-ductile behavior of powder metallurgical tungsten short fiber-reinforced tungsten (W/W), Nucl Mater Energy 15 (2018) 214-219.

[40] J. Riesch, M. Aumann, J.W. Coenen, H. Gietl, G. Holzner, T. Hoschen, P. Huber, M. Li, C. Linsmeier, R. Neu, Chemically deposited tungsten fibre-reinforced tungsten - The way to a mock-up for divertor applications, Nucl Mater Energy 9 (2016) 75-83.

[41] A. Einstein, Ist die Trägheit eines Körpers von seinem Energieinhalt abhängig?, Annalen der Physik 18 (1905) 639-641.

[42] J.R.e. al., Kontrollierte Kernfusion: Grundlagen ihrer Nutzung zur Energieversorgung, Vieweg+Teubner Verlag1981.

[43] K.L.a.M.Q.T. Mitsuru Kikuchi, Fusion Physics, International

Atomic Energy Agency2012.

[44] R.S. Pease, Fusion: the Next Steps, Physics Bulletin 35(11) (1984) 471.

[45] M.N. Rosenbluth, F.L. Hinton, Generic issues for direct conversion of fusion energy from alternative fuels, Plasma Phys Contr F 36(8) (1994) 1255.

[46] D.M. Meade, Tokamak Fusion Test Reactor D-T results, Fusion Engineering and Design 30(1) (1995) 13-23.

[47] J. Sültenfuß, Radionuklid Tritium im Ozean: Meßverfahren und Verteilung von Tritium im Südatlantik und im Weddellmeer, (1998).

[48] T.J. Dolan, Magnetic Fusion Technology, Springer London, London, 2014.

[49] B.M. Frederick, Systems Approaches to Nuclear Fusion Reactors, Springer, Cham, Switzerland, 2019.

[50] J. Bodil, Gamma-ray Lines from (n,2n) and (n,n') Reactions in Radiogenic and Natural Lead, Phys Scripta 2(6) (1970) 277.

[51] O.P. Joneja, V.R. Nargundkar, T.K. Basu, 14-MeV Neutron Multiplication Measurement in Lead, Fusion Technology 12(1) (1987) 114-118.

[52] D.H. Berwald, S. Zenczak, Assessment of Beryllium Resources for Fusion Applications, Fusion Technology 8(1P2B) (1985) 1143-1151.

[53] K. Maki, Energy Multiplication in High Tritium Breeding Ratio Blanket with Front Breeder Zone for Fusion Reactors, J Nucl Sci Technol 25(1) (1988) 72-80.

[54] B. Nevins, Magnetic turnaround for fusion plasmas, Physics World 9(3) (1996) 23.

[55] Y.H. Xu, A general comparison between tokamak and stellarator plasmas, Matter Radiat Extrem 1(4) (2016) 192-200.

[56] P. Helander, C.D. Beidler, T.M. Bird, M. Drevlak, Y. Feng, R. Hatzky, F. Jenko, R. Kleiber, J.H.E. Proll, Y. Turkin, P. Xanthopoulos, Stellarator and tokamak plasmas: a comparison, Plasma Phys Contr F 54(12) (2012) 124009.

[57] F. Giorgetti, An Integrated Multi-Physics Tool for the Mechanical Analysis of Fusion Reactors Superconducting Magnets, University of Rome "TOR VERGATA", Rome, 2018.

[58] J.D. Callen, B.A. Carreras, R.D. Stambaugh, Stability and Transport Processes in Tokamak Plasmas, Physics Today 45(1) (1992) 34-42.

[59] C. Bachmann, G. Aiello, R. Albanese, R. Ambrosino, F. Arbeiter, J. Aubert, L. Boccaccini, D. Carloni, G. Federici, U. Fischer, M. Kovari, A. Li Puma, A. Loving, I. Maione, M. Mattei, G. Mazzone, B. Meszaros, I. Palermo, P. Pereslavtsev, V. Riccardo, P. Sardain, N. Taylor, S. Villari, Z. Vizvary, A. Vaccaro, E. Visca, R. Wenninger, Initial DEMO tokamak design configuration studies, Fusion Engineering and Design 98-99 (2015) 1423-1426.

[60] J.H. You, G. Mazzone, E. Visca, C. Bachmann, E. Autissier, T. Barrett, V. Cocilovo, F. Crescenzi, P.K. Domalapally, D. Dongiovanni, S. Entler, G. Federici, P. Frosi, M. Fursdon, H. Greuner, D. Hancock, D. Marzullo, S. McIntosh, A.V. Muller, M.T. Porfiri, G. Ramogida, J. Reiser, M. Richou, M. Rieth, A. Rydzy, R. Villari, V. Widak, Conceptual design studies for the European DEMO divertor: Rationale and first results, Fusion Engineering and Design 109 (2016) 1598-1603.

[61] C. Angioni, Impurity transport in tokamak plasmas, theory, modelling and comparison with experiments, Plasma Phys Contr F 63(7) (2021).

[62] G. Grieger, W. Lotz, P. Merkel, J. Nührenberg, J. Sapper, E. Strumberger, H. Wobig, R. Burhenn, V. Erckmann, U. Gasparino, L. Giannone, H.J. Hartfuss, R. Jaenicke, G. Kühner, H. Ringler, A. Weller, F. Wagner, t.W.X. Team, t.W.A. Team, Physics optimization of stellarators, Physics of Fluids B: Plasma Physics 4(7) (1992) 2081-2091.

[63] T. Klinger, T. Andreeva, S. Bozhenkov, C. Brandt, R. Burhenn, B. Buttenschön, G. Fuchert, B. Geiger, O. Grulke, H.P. Laqua, N. Pablant, K. Rahbarnia, T. Stange, A. von Stechow, N. Tamura, H. Thomsen, Y. Turkin, T. Wegner, I. Abramovic, S. Äkäslompolo, J. Alcuson, P. Aleynikov, K. Aleynikova, A. Ali, A. Alonso, G. Anda, E. Ascasibar, J.P. Bähner, S.G. Baek, M. Balden, J. Baldzuhn, M. Banduch, T. Barbui, W. Behr, C. Beidler, A. Benndorf, C. Biedermann, W. Biel, B. Blackwell, E. Blanco, M. Blatzheim, S. Ballinger, T. Bluhm, D. Böckenhoff, B. Böswirth, L.G. Böttger, M. Borchardt, V. Borsuk, J. Boscary, H.S. Bosch, M. Beurskens, R. Brakel, H. Brand, T. Bräuer, H. Braune, S. Brezinsek, K.J. Brunner, R. Bussiahn, V. Bykov, J. Cai, I. Calvo, B. Cannas, A. Cappa, A. Carls, D. Carralero, L. Carraro, B. Carvalho, F. Castejon, A. Charl, N. Chaudhary, D. Chauvin, F. Chernyshev, M. Cianciosa, R. Citarella, G. Claps, J. Coenen, M. Cole, M.J. Cole, F. Cordella, G. Cseh, A. Czarnecka, K. Czerski, M. Czerwinski, G. Czymek, A. da Molin, A. da Silva, H. Damm, A. de la Pena, S. Degenkolbe, C.P. Dhard, M. Dibon, A. Dinklage, T. Dittmar, M. Drevlak, P. Drewelow, P. Drews, F. Durodie, E. Edlund, P. van Eeten, F. Effenberg, G. Ehrke, S. Elgeti, M. Endler, D. Ennis, H. Esteban, T. Estrada, J. Fellinger, Y. Feng, E. Flom, H. Fernandes, W.H. Fietz, W. Figacz, J. Fontdecaba, O. Ford, T. Fornal, H. Frerichs, A. Freund, T. Funaba, A. Galkowski, G. Gantenbein, Y. Gao, J. García Regaña, D. Gates, J. Geiger, V.

Giannella, A. Gogoleva, B. Goncalves, A. Goriaev, D. Gradic, M. Grahl, J. Green, H. Greuner, A. Grosman, H. Grote, M. Gruca, C. Guerard, P. Hacker, X. Han, J.H. Harris, D. Hartmann, D. Hathiramani, B. Hein, B. Heinemann, P. Helander, S. Henneberg, M. Henkel, J. Hernandez Sanchez, C. Hidalgo, M. Hirsch, K.P. Hollfeld, U. Höfel, A. Hölting, D. Höschen, M. Houry, J. Howard, X. Huang, Z. Huang, M. Hubeny, M. Huber, H. Hunger, K. Ida, T. Ilkei, S. Illy, B. Israeli, S. Jablonski, M. Jakubowski, J. Jelonnek, H. Jenzsch, T. Jesche, M. Jia, P. Junghanns, J. Kacmarczyk, J.P. Kallmeyer, U. Kamionka, H. Kasahara, W. Kasparek, Y.O. Kazakov, N. Kenmochi, C. Killer, A. Kirschner, R. Kleiber, J. Knauer, M. Knaup, A. Knieps, T. Kobarg, G. Kocsis, F. Köchl, Y. Kolesnichenko, A. Könies, R. König, P. Kornejew, J.P. Koschinsky, F. Köster, M. Krämer, R. Krampitz, A. Krämer-Flecken, N. Krawczyk, T. Kremeyer, J. Krom, M. Krychowiak, I. Ksiazek, M. Kubkowska, G. Kühner, T. Kurki-Suonio, P.A. Kurz, S. Kwak, M. Landreman, P. Lang, R. Lang, A. Langenberg, S. Langish, H. Laqua, R. Laube, S. Lazerson, C. Lechte, M. Lennartz, W. Leonhardt, C. Li, C. Li, Y. Li, Y. Liang, C. Linsmeier, S. Liu, J.F. Lobsien, D. Loesser, J. Loizu Cisquella, J. Lore, A. Lorenz, M. Losert, A. Lücke, A. Lumsdaine, V. Lutsenko, H. Maaßberg, O. Marchuk, J.H. Matthew, S. Marsen, M. Marushchenko, S. Masuzaki, D. Maurer, M. Mayer, K. McCarthy, P. McNeely, A. Meier, D. Mellein, B. Mendelevitch, P. Mertens, D. Mikkelsen, A. Mishchenko, B. Missal, J. Mittelstaedt, T. Mizuuchi, A. Mollen, V. Moncada, T. Mönnich, T. Morisaki, D. Moseev, S. Murakami, G. Náfrádi, M. Nagel, D. Naujoks, H. Neilson, R. Neu, O. Neubauer, U. Neuner, T. Ngo, D. Nicolai, S.K. Nielsen, H. Niemann, T. Nishizawa, R. Nocentini, C. Nührenberg, J. Nührenberg, S. Obermayer, G. Offermanns, K. Ogawa, J. Ölmanns, J. Ongena, J.W. Oosterbeek, G. Orozco, M. Otte, L. Pacios Rodriguez, N. Panadero, N. Panadero Alvarez, D. Papenfuß, S. Paqay, E. Pasch, A. Pavone, E. Pawelec, T.S. Pedersen, G. Pelka, V. Perseo, B. Peterson, D. Pilopp, S. Pingel, F. Pisano, B. Plaum, G. Plunk, P. Pölöskei, M. Porkolab, J. Proll, M.E. Puiatti, A. Puig Sitjes, F. Purps, M. Rack, S. Récsei, A. Reiman, F. Reimold, D. Reiter, F. Remppel, S. Renard, R. Riedl, J. Riemann, K. Risse, V. Rohde, H. Röhlinger, M. Romé, D. Rondeshagen, P. Rong, B. Roth, L. Rudischhauser, K. Rummel, T. Rummel, A. Runov, N. Rust, L. Ryc, S. Ryosuke, R. Sakamoto, M. Salewski, A. Samartsev, E. Sanchez, F. Sano, S. Satake, J. Schacht, G. Satheeswaran, F. Schauer, T. Scherer, J. Schilling, A. Schlaich, G. Schlisio, F. Schluck, K.H. Schlüter, J. Schmitt, H. Schmitz, O. Schmitz, S. Schmuck, M. Schneider, W. Schneider, P. Scholz, R. Schrittwieser, M. Schröder, T. Schröder, R. Schroeder, H. Schumacher, B. Schweer, E. Scott, S. Sereda, B. Shanahan, M. Sibilia, P. Sinha, S. Sipliä, C. Slaby, M. Sleczka, H. Smith, W. Spiess, D.A. Spong, A. Spring, R. Stadler, M. Stejner, L. Stephey, U. Stridde, C. Suzuki, J. Svensson, V. Szabó, T. Szabolics, T. Szepesi, Z. Szökefalvi-Nagy, A. Tancetti, J. Terry, J. Thomas, M. Thumm, J.M. Travere, P. Traverso, J. Tretter, H. Trimino Mora, H. Tsuchiya, T. Tsujimura, S. Tulipán, B. Unterberg, I. Vakulchyk, S. Valet, L. Vano, B. van Milligen, A.J. van Vuuren, L. Vela, J.L. Velasco, M. Vergote, M. Vervier, N. Vianello, H. Viebke, R. Vilbrandt, A. Vorköper, S. Wadle, F. Wagner, E. Wang, N. Wang, Z. Wang, F. Warmer, T. Wauters, L. Wegener, J. Weggen, Y. Wei, G. Weir, J. Wendorf, U. Wenzel, A. Werner, A. White, B. Wiegel, F. Wilde, T. Windisch, M. Winkler, A. Winter, V. Winters, S. Wolf, R.C. Wolf, A. Wright, G. Wurden, P. Xanthopoulos, H. Yamada, I. Yamada, R. Yasuhara, M. Yokoyama, M. Zanini, M. Zarnstorff, A. Zeitler, D. Zhang, H. Zhang, J. Zhu, M. Zilker, A. Zocco, S. Zoletnik, M. Zuin, Overview of first Wendelstein 7-X high-performance operation, Nucl Fusion 59(11) (2019) 112004.

[64] P. Costello, J.H.E. Proll, G.G. Plunk, M.J. Pueschel, J.A. Alcusón, The universal instability in optimised stellarators, J Plasma Phys 89(4) (2023) 905890402.

[65] G.G. Plunk, J.W. Connor, P. Helander, Collisionless microinstabilities in stellarators. Part 4. The ion-driven trapped-electron mode, J Plasma Phys 83(4) (2017).

[66] H. Zohm, Edge localized modes (ELMs), Plasma Phys Contr F 38(2) (1996) 105.

[67] J.A. Lei, N.X. Zheng, J.F. Bi, F.J. Zhao, Y.Y. Wang, J.H. Yang, Research on the evolution law of aggregate micro-texture during long-term wearing of asphalt pavement, Constr Build Mater 444 (2024).

[68] G. Stankunas, S. Breidokaite, Neutron irradiation-induced shutdown dose rate estimation in EU DEMO divertor, Appl Radiat Isotopes 210 (2024).

[69] F. Crea, B. Böswirth, E. Cacciotti, A. Galatanu, H. Greuner, C. García-Rosales, P. Lorusso, S. Roccella, E. Sal, L. Verdini, M. Wirtz, Mock-ups fabrication by HRP technology with advanced W-alloy monoblocks for DEMO divertor target, Fusion Engineering and Design 201 (2024).

[70] V. Díaz-Mena, J. de Prado, M. Roldán, I. Izaguirre, M. Sánchez, M. Rieth, A. Ureña, Numerical and experimental development of cupronickel filler brazed joints for divertor and first wall components in DEMO fusion reactor, J Nucl Mater 588 (2024).

[71] Y. Ueda, K. Schmid, M. Balden, J.W. Coenen, T. Loewenhoff, A. Ito, A. Hasegawa, C. Hardie, M. Porton, M. Gilbert, Baseline high heat flux and plasma facing materials for fusion, Nucl Fusion 57(9) (2017).

[72] T. Grammes, T. Emmerich, D.D. Qu, O. Heinze, R. Vassen, J. Aktaa, Functionally graded tungsten/EUROFER coating for DEMO first wall: From laboratory to industrial production, Fusion Engineering and Design 188 (2023).

[73] V. Barabash, G. Federici, M. Rodig, L.L. Snead, C.H. Wu, Neutron irradiation effects on plasma facing materials, J Nucl Mater 283 (2000) 138-146.

[74] H. Bolt, V. Barabash, G. Federici, J. Linke, A. Loarte, J. Roth, K. Sato, Plasma facing and high heat flux materials - needs for ITER and beyond, J Nucl Mater 307 (2002) 43-52.

[75] D. Stork, P. Agostini, J.L. Boutard, D. Buckthorpe, E. Diegele, S.L. Dudarev, C. English, G. Federici, M.R. Gilbert, S. Gonzalez, A. Ibarra, C. Linsmeier, A. Li Puma, G. Marbach, P.F. Morris, L.W. Packer, B. Raj, M. Rieth, M.Q. Tran, D.J. Ward, S.J. Zinkle, Developing structural, high-heat flux and plasma facing materials for a near-term DEMO fusion power plant: The EU assessment, J Nucl Mater 455(1-3) (2014) 277-291.

[76] S. Dwivedi, M. Vishwakarma, Hydrogen embrittlement in different materials: A review, International Journal of Hydrogen Energy 43 (2018).

[77] M.S. Kaminsky, Plasma contamination and wall erosion in controlled thermonuclear fusion devices and reactors, Conference: 5. conference on plasma physics and controlled nuclear fusion research, Tokyo, Japan, 11 Nov 1974; Other Information: See STI/PUB--381(Vol.2); CONF-741105--P2. Orig. Receipt Date: 30-JUN-76; Related Information: Plasma physics and controlled nuclear fusion research, 1974. Vol. II, International Atomic Energy Agency, Vienna, IAEA, 1975, pp. Medium: X; Size: Pages: 287-299 2016-06-27.

[78] R.P. Doerner, S.I. Krasheninnikov, K. Schmid, Particle-induced erosion of materials at elevated temperature, Journal of Applied Physics 95(8) (2004) 4471-4475.

[79] P. Bouin, A. Fissolo, C. Gourdin, Study of the Crack Propagation Behaviour of 304l Austenitic Stainless Steel under Thermal Fatigue., Proceedings of the Asme Pressure Vessels and Piping Conference, Vol 3 (2012) 495-503.

[80] A. Fissolo, B. Marini, G. Nais, P. Wident, Thermal fatigue behaviour for a 316 L type steel, J Nucl Mater 233-237 (1996) 156-161.

[81] Y. Li, T.W. Morgan, T. Vermeij, J.W.M. Vernimmen, T. Loewenhoff, J.P.M. Hoefnagels, J.A.W. van Dommelen, M. Wirtz, G. De Temmerman, K. Verbeken, M.G.D. Geers, Recrystallization-mediated crack initiation in tungsten under simultaneous high-flux hydrogen plasma loads and high-cycle transient heating, Nucl Fusion 61(4) (2021) 046018.

[82] M. Wirtz, J. Linke, T. Loewenhoff, G. Pintsuk, I. Uytdenhouwen, Transient heat load challenges for plasma-facing materials during long-term operation, Nucl Mater Energy 12 (2017) 148-155.

[83] J.W. Coenen, M. Berger, M.J. Demkowicz, D. Matveev, A. Manhard, R. Neu, J. Riesch, B. Unterberg, M. Wirtz, C. Linsmeier, Plasma-wall interaction of advanced materials, Nucl Mater Energy 12 (2017) 307-312.

[84] R.A. Pitts, S. Bardin, B. Bazylev, M.A. van den Berg, P. Bunting, S. Carpentier-Chouchana, J.W. Coenen, Y. Corre, R. Dejarnac, F. Escourbiac, J. Gaspar, J.P. Gunn, T. Hirai, S.H. Hong, J. Horacek, D. Iglesias, M. Komm, K. Krieger, C. Lasnier, G.F. Matthews, T.W. Morgan, S. Panayotis, S. Pestchanyi, A. Podolnik, R.E. Nygren, D.L. Rudakov, G. De Temmerman, P. Vondracek, J.G. Watkins, Physics conclusions in support of ITER W divertor monoblock shaping, Nucl Mater Energy 12 (2017) 60-74.

[85] S.H. Huang, S.M. Liu, Numerical Analysis of Fatigue Behavior of ITER-Like Monoblock Divertor Interlayer Under Coupled Heat Loads, J Fusion Energ 37(4) (2018) 177-186.

[86] D. Terentyev, C. Yin, A. Dubinko, C.C. Chang, J.H. You, Neutron irradiation hardening across ITER diverter tungsten armor, Int J Refract Met H 95 (2021).

[87] ITER, Prototype - The hottest stuff in ITER, 2018. https://www.iter.org/newsline/-/3027. (Accessed 15.09.2024.

[88] Filipp, Thermonuclear reactor ITER. Tokamak. Reproduced with permission from Adobe Stock (File No. 468648884, standard licence), Adobe Stock.

[89] R.A. Pitts, X. Bonnin, F. Escourbiac, H. Frerichs, J.P. Gunn, T. Hirai, A.S. Kukushkin, E. Kaveeva, M.A. Miller, D. Moulton, V. Rozhansky, I. Senichenkov, E. Sytova, O. Schmitz, P.C. Stangeby, G. De Temmerman, I. Veselova, S. Wiesen, Physics basis for the first ITER tungsten divertor, Nucl Mater Energy 20 (2019).

[90] R. Tivey, T. Ando, A. Antipenkov, V. Barabash, S. Chiocchio, G. Federici, C. Ibbott, R. Jakeman, G. Janeschitz, R. Raffray, M. Akiba, I. Mazul, H. Pacher, M. Ulrickson, G. Vieider, ITER divertor, design issues and research and development, Fusion Engineering and Design 46(2) (1999) 207-220.

[91] J. Uchiyama, Y. Seki, T. Kunugi, S.-i. Satake, Turbulent heat transfer for coolant water flow in plasma facing component, Fusion Engineering and Design 159 (2020) 111817.

[92] Y. Seki, K. Ezato, S. Suzuki, K. Yokoyama, H. Yamada, T. Hirayama, T. Hirai, Numerical and experimental study of coolant water flow in ITER divertor outer vertical target, Fusion Engineering and Design 136 (2018) 420-425.

[93] C.B. Baxi, Comparison of swirl tube and hypervapotron for cooling of ITER divertor, Proceedings of 16th International Symposium on Fusion Engineering, 1995, pp. 186-189 vol.1.

[94] G. Federici, C. Bachmann, W. Biel, L. Boccaccini, F. Cismondi, S. Ciattaglia, M. Coleman, C. Day, E. Diegele, T. Franke, M. Grattarola, H. Hurzlmeier, A. Ibarra, A. Loving, F. Maviglia, B. Meszaros, C. Morlock, M. Rieth, M. Shannon, N. Taylor, M.Q. Tran, J.H. You, R. Wenninger, L. Zani, Overview of the design approach and prioritization of R&D activities towards an EU DEMO, Fusion Engineering and Design 109-111 (2016) 1464-1474.

[95] H. Yamada, R. Kasada, A. Ozaki, R. Sakamoto, Y. Sakamoto, H. Takenaga, T. Tanaka, H. Tanigawa, K. Okano, K. Tobita, O. Kaneko, K. Ushigusa, Development of Strategic Establishment of Technology Bases for a Fusion DEMO Reactor in Japan, J Fusion Energ 35(1) (2016) 4-26.

[96] K.M. Feng, G.S. Zhang, G.Y. Zheng, Z. Zhao, T. Yuan, Z.Q. Li, G.Z. Sheng, C.H. Pan, Conceptual design study of fusion DEMO plant at SWIP, Fusion Engineering and Design 84(12) (2009) 2109-2113.

[97] C.H. Pan, Y.C. Wu, K.M. Feng, S.L. Liu, DEMO development strategy based on China FPP program, Fusion Engineering and Design 83(7) (2008) 877-882.

[98] P. Rindt, J.L. van den Eijnden, T.W. Morgan, N.J.L. Cardozo, Conceptual design of a liquid-metal divertor for the European DEMO, Fusion Engineering and Design 173 (2021).

[99] C.B. Baxi, Evaluation of Helium Cooling for Fusion Divertors, Fusion Engineering and Design 25(1-3) (1994) 263-271.

[100] T. Ihli, M. Ilic, Efficient helium cooling methods for nuclear fusion devices: Status and prospects, Fusion Engineering and Design 84(2-6) (2009) 964-968.

[101] Z. Wang, S.C. Zhang, Z.B. Chen, J.T. Jia, C. Chao, A novel liquid lithium jet-cooled finger-type divertor target concept for fusion power plant application, Nucl Fusion 61(4) (2021).

[102] H. Reimerdes, R. Ambrosino, P. Innocente, A. Castaldo, P. Chmielewski, G. Di Gironimo, S. Merriman, V. Pericoli-Ridolfini, L. Aho-Mantilla, R. Albanese, H. Bufferand, G. Calabro, G. Ciraolo, D. Coster, N. Fedorczak, S. Ha, R. Kembleton, K. Lackner, V.P. Loschiavo, T. Lunt, D. Marzullo, R. Maurizio, F. Militello, G. Ramogida, F. Subba, S. Varoutis, R. Zagórski, H. Zohm, Assessment of alternative divertor configurations as an exhaust solution for DEMO, Nucl Fusion 60(6) (2020) 066030.

[103] K. Ezato, S. Suzuki, M. Dairaku, M. Akiba, Critical heat flux experiments using a screw tube under DEMO divertor-relevant cooling conditions, Fusion Engineering and Design 83(7) (2008) 1097-1101.

[104] M. Galatanu, M. Cioca, A. Ighigeanu, G. Ruiu, M. Enculescu, B. Popescu, A. Galatanu, Development of W-monoblock divertor components with embedded thermal barrier interfaces, Fusion Engineering and Design 146 (2019) 1351-1354.

[105] A. Herrmann, H. Greuner, M. Balden, H. Bolt, Design and evaluation of an optimized W/Cu interlayer for W monoblock components, Fusion Engineering and Design 86(1) (2011) 27-32.

[106] A.v. Müller, G. Schlick, R. Neu, C. Anstätt, T. Klimkait, J. Lee, B. Pascher, M. Schmitt, C. Seidel, Additive manufacturing of pure tungsten by means of selective laser beam melting with substrate preheating temperatures up to 1000 ◦C, Nucl Mater Energy 19 (2019) 184-188.

[107] A.v. Muller, D. Ewert, A. Galatanu, M. Milwich, R. Neu, J.Y. Pastor, U. Siefken, E. Tejado, J.H. You, Melt infiltrated tungsten–copper composites as advanced heat sink materials for plasma facing components of future nuclear fusion devices, Fusion Engineering and Design 124 (2017) 455-459.

[108] R. Neu, J. Coenen, B. Curzadd, H. Gietl, H. Greuner, T. Hoeschen, K. Hunger, R. Lürbke, A. v. Müller, J. Riesch, G. Schlick, U. Siefken, E. Visca, J.-H. You, Material and component developments for the DEMO divertor using fibre reinforcement and additive manufacturing, Materials Research Express 10 (2023).

[109] V. Philipps, Tungsten as material for plasma-facing components in fusion devices, J Nucl Mater 415(1) (2011) S2-S9.

[110] J.W. Davis, V.R. Barabash, A. Makhankov, L. Plöchl, K.T. Slattery, Assessment of tungsten for use in the ITER plasma facing components1#AC-3013 with Sandia National Laboratories.1, J Nucl Mater 258-263 (1998) 308-312.

[111] J.W. Coenen, Fusion Materials Development at Forschungszentrum Julich, Adv Eng Mater 22(6) (2020).

[112] J.W. Coenen, V.Y.S. Lee, Y.R. Mao, A. Morrison, D. Dorow-Gerspach, X.Y. Tan, A. Terra, Y.C. Wu, C. Linsmeier, Evolution of Tungsten Fiber-Reinforced Tungsten-Remarks on Production and Joining, Adv Eng Mater 25(19) (2023).

[113] S.J. Zinkle, N.M. Ghoniem, Operating temperature windows for fusion reactor structural materials, Fusion Engineering and Design 51-52 (2000) 55-71.

[114] S. Noce, D. Flammini, P. Gaudio, M. Gelfusa, G. Mazzone, F. Moro, F. Romanelli, R. Villari, J.-H. You, Neutronics Assessment of the Spatial Distributions of the Nuclear Loads on the DEMO Divertor ITER-like Targets: Comparison between the WCLL and HCPB Blanket, Applied Sciences 13(3) (2023) 1715.

[115] E. Lang, H. Schamis, N. Madden, C. Smith, R. Kolasinski, J. Krogstad, J.P. Allain, Recrystallization suppression through dispersion-strengthening of tungsten, J Nucl Mater 545 (2021) 152613.

[116] M.A. Oude Vrielink, J.A.W. van Dommelen, M.G.D. Geers, Multi-scale fracture probability analysis of tungsten monoblocks under fusion conditions, Nucl Mater Energy 28 (2021) 101032.

[117] A. Durif, M. Richou, G. Kermouche, J.M. Bergheau, Numerical study of the influence of tungsten recrystallization on the divertor component lifetime, International Journal of Fracture 230(1) (2021) 83-98.

[118] S.-M. Wang, J.-S. Li, Y.-X. Wang, X.-F. Zhang, Q. Ye, Thermal Shock Behavior Analysis of Tungsten-Armored Plasma-Facing Components for Future Fusion Reactor, Acta Metallurgica Sinica (English Letters) 31(5) (2018) 515-522.

[119] S.C. Cifuentes, M.A. Monge, P. Pérez, On the oxidation mechanism of pure tungsten in the temperature range 600-800 °C, Corros Sci 57 (2012) 114-121.

[120] E. Lassner, W.-D. Schubert, Tungsten : properties, chemistry, technology of the element, alloys, and chemical compounds, Kluwer Academic/Plenum Publishers, New York, 1999.

[121] S.W.H. Yih, C.T. Wang, Tungsten : sources, metallurgy, properties, and applications, Plenum Press, New York, 1979.

[122] A. Litnovsky, F. Klein, X. Tan, J. Schmitz, J. Coenen, C. Linsmeier, J. Gonzalez-Julian, M. Bram, I. Povstugar, T. Morgan, Y. Gasparyan, A. Suchkov, D. Bachurina, N. Manh, M. Gilbert, D. Sobieraj, J. Wróbel, E. Tejado, J. Matějíček, A. Reuban, Advanced Self-Passivating Alloys for an Application under Extreme Conditions, Metal 11 (2021) 1255.

[123] F. Koch, H. Bolt, Self passivating W-based alloys as plasma facing material for nuclear fusion, Phys Scripta 2007(T128) (2007) 100.

[124] A. Calvo, C. García-Rosales, N. Ordás, I. Iturriza, K. Schlueter, F. Koch, G. Pintsuk, E. Tejado, J.Y. Pastor, Self-passivating W-Cr-Y alloys: Characterization and testing, Fusion Engineering and Design 124 (2017) 1118-1121.

[125] A. Litnovsky, T. Wegener, F. Klein, C. Linsmeier, M. Rasinski, A. Kreter, X. Tan, J. Schmitz, Y. Mao, J.W. Coenen, M. Bram, J. Gonzalez-Julian, Advanced smart tungsten alloys for a future fusion power plant, Plasma Phys Contr F 59(6) (2017).

[126] A. Litnovsky, T. Wegener, F. Klein, C. Linsmeier, M. Rasinski, A. Kreter, B. Unterberg, J.W. Coenen, H. Du, J. Mayer, C. Garcia-Rosales, A. Calvo, N. Ordas, Smart tungsten alloys as a material for the first wall of a future fusion power plant, Nucl Fusion 57(6) (2017).

[127] A. Litnovsky, T. Wegener, F. Klein, C. Linsmeier, M. Rasinski, A. Kreter, B. Unterberg, M. Vogel, S. Kraus, U. Breuer, C. Garcia-Rosales, A. Calvo, N. Ordas, Smart alloys for a future fusion power plant: First studies under stationary plasma load and in accidental conditions, Nucl Mater Energy 12 (2017) 1363-1367.

[128] D. Bachurina, X.-Y. Tan, F. Klein, A. Suchkov, A. Litnovsky, J. Schmitz, J. Gonzalez-Julian, M. Bram, J.W. Coenen, Y.-C. Wu, C. Linsmeier, Self-passivating smart tungsten alloys for DEMO: a progress in joining and upscale for a first wall mockup, Tungsten 3(1) (2021) 101-115.

[129] J. Engels, A. Houben, M. Rasinski, C. Linsmeier, Hydrogen saturation and permeation barrier performance of yttrium oxide coatings, Fusion Engineering and Design 124 (2017) 1140-1143.

[130] A. El-Kharbachi, J. Chêne, S. Garcia-Argote, L. Marchetti, F. Martin, F. Miserque, D. Vrel, M. Redolfi, V. Malard, C. Grisolia, B. Rousseau, Tritium absorption/desorption in ITER-like tungsten particles, International Journal of Hydrogen Energy 39(20) (2014) 10525-10536.

[131] C.H. Skinner, Tritium Retention and Removal in Tokamaks, AIP Conference Proceedings 1095(1) (2009) 127-145.

[132] Y. Xu, Z.-S. Wu, L.-M. Luo, X. Zan, X.-Y. Zhu, Q. Xu, Y.-C. Wu, Transport parameters and permeation behavior of hydrogen isotopes in the first wall materials of future fusion reactors, Fusion Engineering and Design 155 (2020) 111563.

[133] L.A. Sedano, R. Conrad, M.A. Fütterer, R. May, R. Viola, X. Dies, LIBRETTO-3: modelling tritium extraction/permeation and evaluation of permeation barriers under irradiation, J Nucl Mater 233-237 (1996) 1411-1415.

[134] F. Yang, X. Xiang, G. Lu, G. Zhang, T. Tang, Y. Shi, X. Wang, Tritium permeation characterization of Al2O3/FeAl coatings as tritium permeation barriers on 321 type stainless steel containers, J Nucl Mater 478 (2016) 144-148.

[135] V. Nemanic, Hydrogen permeation barriers: Basic requirements, materials selection, deposition methods, and quality evaluation, Nucl Mater Energy 19 (2019) 451-457.

[136] L.-M. Luo, Y.-L. Liu, D.-G. Liu, L. Zheng, Y.-C. Wu, Preparation technologies and performance studies of tritium permeation barriers for future nuclear fusion reactors, Surface and Coatings Technology 403 (2020) 126301.

[137] R. Endoh, S. Nogami, Y. Hishinuma, T. Chikada, Submicron-thick yttria-stabilized zirconia coating as an advanced tritium permeation barrier, Nucl Fusion 61(7) (2021) 076015.

[138] A. Houben, M. Rasinski, C. Linsmeier, Hydrogen Permeation in Fusion Materials and the Development of Tritium Permeation Barriers, Plasma Fusion Res 15 (2020).

[139] E. Bernard, R. Sakamoto, E. Hodille, A. Kreter, E. Autissier, M.F. Barthe, P. Desgardin, T. Schwarz-Selinger, V. Burwitz, S. Feuillastre, S. Garcia-Argote, G. Pieters, B. Rousseau, M. Ialovega, R. Bisson, F. Ghiorghiu, C. Corr, M. Thompson, R. Doerner, S. Markelj, H. Yamada, N. Yoshida, C. Grisolia, Tritium retention in w plasma-facing materials: Impact of the material structure and helium irradiation (vol 19, pg 403, 2019), Nucl Mater Energy 22 (2020).

[140] M. Shimada, C.N. Taylor, L. Moore-McAteer, R.J. Pawelko, R.D. Kolasinski, D.A. Buchenauer, L.C. Cadwallader, B.J. Merrill, TPE upgrade for enhancing operational safety and improving in-vessel tritium inventory assessment in fusion nuclear environment, Fusion Engineering and Design 109-111 (2016) 1077-1081.

[141] D. Rupp, S.M. Weygand, Experimental investigation of the fracture toughness of polycrystalline tungsten in the brittle and semi-brittle regime, J Nucl Mater 386-388 (2009) 591-593.

[142] W. Timmis, Material assessment report on the use of copper alloys in DEMO, Culham Centre for Fusion Energy, 2012.

[143] A. Li-Puma, M. Richou, P. Magaud, M. Missirlian, E. Visca, V.P. Ridolfini, Potential and limits of water cooled divertor concepts based on monoblock design as possible candidates for a DEMO reactor, Fusion Engineering and Design 88(9-10) (2013) 1836-1843.

[144] S. Panayotis, T. Hirai, V. Barabash, C. Amzallag, F. Escourbiac, A. Durocher, V. Komarov, J.M. Martinez, M. Merola, Fracture modes of ITER tungsten divertor monoblock under stationary thermal loads, Fusion Engineering and Design 125 (2017) 256-262.

[145] P. Paulraj, D. Senthilkumaran, Reduction of environmental impact by incorporating performance oriented life cycle assessment, Environment Protection Engineering 42 (2016) 113-122.

[146] S.V.d. Kerkhof, M. Blommaert, J.W. Coenen, S. Heuer, M. Baelmans, Investigating the potential of FGMs through numerical minimization of thermal stresses, Phys Scripta 2020(T171) (2020) 014001.

[147] R. Aymar, The ITER reduced cost design, Fusion Engineering and Design 49-50 (2000) 13-25.

[148] R.A. Pitts, S. Carpentier, F. Escourbiac, T. Hirai, V. Komarov, S. Lisgo, A.S. Kukushkin, A. Loarte, M. Merola, A. Sashala Naik, R. Mitteau, M. Sugihara, B. Bazylev, P.C. Stangeby, A full tungsten divertor for ITER: Physics issues and design status, J Nucl Mater 438 (2013) S48-S56.

[149] G. Pintsuk, I. Bobin-Vastra, S. Constans, P. Gavila, M. Rodig, B. Riccardi, Qualification and post-mortem characterization of tungsten mock-ups exposed to cyclic high heat flux loading, Fusion Engineering and Design 88(9-10) (2013) 1858-1861.

[150] T. Hirai, S. Panayotis, V. Barabash, C. Amzallag, F. Escourbiac, A. Durocher, M. Merola, J. Linke, T. Loewenhoff, G. Pintsuk, M. Wirtz, I. Uytdenhouwen, Use of tungsten material for the ITER divertor, Nucl Mater Energy 9 (2016) 616-622.

[151] J. You, G. Mazzone, E. Visca, H. Greuner, M. Fursdon, Y. Addab, C. Bachmann, T. Barrett, U. Bonavolonta, B. Boswirth, F.M. Castrovinci, C. Carelli, D. Coccorese, R. Coppola, F. Crescenzi, G. Di Gironimo, P.A. Di Maio, G. Di Mambro, F. Domptail, D. Dongiovanni, G. Dose, D. Flammini, L. Forest, P. Frosi, F. Gallay, B.E. Ghidersa, C. Harrington, K. Hunger, V. Imbriani, M. Li, A. Lukenskas, A. Maffucci, N. Mantel, D. Marzullo, T. Minniti, A.V. Muller, S. Noce, M.T. Porfiri, A. Quartararo, M. Richou, S. Roccella, D. Terentyev, A. Tincani, E. Vallone, S. Ventre, R. Villari, F. Villone, C. Vorpahl, K. Zhang, Divertor of the European DEMO: Engineering and technologies for power exhaust, Fusion Engineering and Design 175 (2022).

[152] J.H. You, E. Visca, C. Bachmann, T. Barrett, F. Crescenzi, M. Fursdon, H. Greuner, D. Guilhem, P. Languille, M. Li, S. McIntosh, A.V. Muller, J. Reiser, M. Richou, M. Rieth, European DEMO divertor target: Operational requirements and material-design interface, Nucl Mater Energy 9 (2016) 171-176.

[153] J.H. You, E. Visca, T. Barrett, B. Boswirth, F. Crescenzi, F. Domptail, M. Fursdon, F. Gallay, B.E. Ghidersae, H. Greunera, M. Li, A.V. Muller, J. Reiser, M. Richou, S. Roccella, C. Vorpahl, European divertor target concepts for DEMO: Design rationales and high heat flux performance, Nucl Mater Energy 16 (2018) 1-11.

[154] C. Ren, Z.Z. Fang, M. Koopman, B. Butler, J. Paramore, S. Middlemas, Methods for improving ductility of tungsten-a review, International Journal of Refractory Metals and Hard Materials 75 (2018) 170-183.

[155] R. Alba, R. Iglesias, M.A. Cerdeira, Materials to Be Used in Future Magnetic Confinement Fusion Reactors: A Review, Materials 15(19) (2022).

[156] S. Wurster, B. Gludovatz, R. Pippan, High temperature fracture experiments on tungsten-rhenium alloys, Int J Refract Met H 28(6) (2010) 692-697.

[157] M. Fujitsuka, B. Tsuchiya, I. Mutoh, T. Tanabe, T. Shikama, Effect of neutron irradiation on thermal diffusivity of tungsten-rhenium alloys, J Nucl Mater 283 (2000) 1148-1151.

[158] S. Wurster, N. Baluc, M. Battabyal, T. Crosby, J. Du, C. Garcia-Rosales, A. Hasegawa, A. Hoffmann, A. Kimura, H. Kurishita, R.J. Kurtz, H. Li, S. Noh, J. Reiser, J. Riesch, M. Rieth, W. Setyawan, M. Walter, J.H. You, R. Pippan, Recent progress in R&D on tungsten alloys for divertor structural and plasma facing materials, J Nucl Mater 442(1-3) (2013) S181-S189.

[159] N.N. Qiu, Y. Zhang, C. Zhang, H. Tong, X.P. Song, Tensile properties of tungsten-rhenium wires with nanofibrous structure, Int J Min Met Mater 25(9) (2018) 1055-1059.

[160] S. Nogami, A. Hasegawa, M. Fukuda, S. Watanabe, J. Reiser, M. Rieth, Tungsten modified by potassium doping and rhenium addition for fusion reactor applications, Fusion Engineering and Design 152 (2020).

[161] S.L.K. Konuru, U. V, B. Sarkar, A. Sarma, Effect of tantalum addition on the mechanical properties of tungsten/tantalum composite thin films, Proceedings of the Institution of Mechanical Engineers, Part E: Journal of Process Mechanical Engineering 0(0) (2023) 09544089231151572.

[162] S. Wurster, B. Gludovatz, A. Hoffmann, R. Pippan, Fracture behaviour of tungsten-vanadium and tungsten-tantalum alloys and composites, J Nucl Mater 413(3) (2011) 166-176.

[163] M.V. Aguirre, A. Martín, J.Y. Pastor, J. Llorca, M.A. Monge, R. Pareja, Mechanical Behavior of W-Y2O3 and W-Ti Alloys from 25 °C to 1000 °C, Metall Mater Trans A 40a(10) (2009) 2283-2290.

[164] M. Rieth, J. Reiser, B. Dafferner, S. Baumgärtner, The Impact of Refractory Material Properties on the Helium Cooled Divertor Design, Fusion Sci Technol 61(1t) (2012) 381-384.

[165] D. Terentyev, X.Z. Xiao, A. Dubinko, A. Bakaeva, H.L. Duan, Dislocation-mediated strain hardening in tungsten: Thermo-mechanical plasticity theory and experimental validation, J Mech Phys Solids 85 (2015) 1-15.

[166] J. Reiser, J. Hoffmann, U. Jäntsch, M. Klimenkov, S. Bonk, C. Bonnekoh, M. Rieth, A. Hoffmann, T. Mrotzek, Ductilisation of tungsten (W): On the shift of the brittle-to-ductile transition (BDT) to lower temperatures through cold rolling, Int J Refract Met H 54 (2016) 351-369.

[167] A. Patra, R. Saxena, S.K. Karak, Combined effect of Ni and nano-Y

O

addition on microstructure, mechanical and high temperature behavior of mechanically alloyed W-Mo (Nov, 10.1016/j.ijrmhm.2016.07.017., 2016), Int J Refract Met H 96 (2021).

[168] Y. Zhang, A.V. Ganeev, J.T. Wang, J.Q. Liu, I.V. Alexandrov, Observations on the ductile-to-brittle transition in ultrafine-grained tungsten of commercial purity, Mat Sci Eng a-Struct 503(1-2) (2009) 37-40.

[169] Q. Wei, H.T. Zhang, B.E. Schuster, K.T. Ramesh, R.Z. Valiev, L.J. Kecskes, R.J. Dowding, L. Magness, K. Cho, Microstructure and mechanical properties of super-strong nanocrystalline tungsten processed by high-pressure torsion, Acta Materialia 54(15) (2006) 4079-4089.

[170] Z.Z. Yan, G.Y. Xu, J.P. Suo, Effect of Transition Layer on Properties of Tungsten-Tantalum (W-Ta) Laminated Composite, Metals 10(5) (2020).

[171] T.L. Shen, Y. Dai, Y. Lee, Microstructure and tensile properties of tungsten at elevated temperatures, J Nucl Mater 468 (2016) 348-354.

[172] K.H. Lee, S.I. Cha, H.J. Ryu, S.H. Hong, Effect of two-stage sintering process on microstructure and mechanical properties of ODS tungsten heavy alloy, Mat Sci Eng a-Struct 458(1-2) (2007) 323-329.

[173] I. Wesemann, W. Spielmann, P. Heel, A. Hoffmann, Fracture strength and microstructure of ODS tungsten alloys, Int J Refract Met H 28(6) (2010) 687-691.

[174] M. Wang, Z.J. Wang, J.H. Qiu, X.L. Xi, Z.R. Nie, Improvement in thermal stability of ODS-W alloy through formation of complex oxide dispersoids, J Alloy Compd 1002 (2024).

[175] G.Q. Wei, Q. Zhang, X.P. Liu, Y.F. Zhang, X. Meng, H.X. Li, Z.P. Li, L.M. Luo, Y.C. Wu, Study and theoretical explanation on high-temperature strength of ODS-W alloy, Mater Charact 214 (2024).

[176] J. Reiser, M. Rieth, A. Möslang, B. Dafferner, J. Hoffmann, T. Mrotzek, A. Hoffmann, D.E.J. Armstrong, X.O. Yi, Tungsten foil laminate for structural divertor applications - Joining of tungsten foils, J Nucl Mater 436(1-3) (2013) 47-55.

[177] J. Reiser, M. Rieth, A. Möslang, B. Dafferner, A. Hoffmann, X.O. Yi, D.E.J. Armstrong, Tungsten foil laminate for structural divertor applications - Tensile test properties of tungsten foil, J Nucl Mater 434(1-3) (2013) 357-366.

[178] J. Reiser, M. Rieth, B. Dafferner, A. Hoffmann, X.O. Yi, D.E.J. Armstrong, Tungsten foil laminate for structural divertor applications - Analyses and characterisation of tungsten foil, J Nucl Mater 424(1-3) (2012) 197-203.

[179] J. Reiser, M. Rieth, B. Dafferner, A. Hoffmann, Tungsten foil laminate for structural divertor applications - Basics and outlook, J Nucl Mater 423(1-3) (2012) 1-8.

[180] J. Reiser, M. Rieth, A. Moslang, H. Greuner, D.E.J. Armstrong, T. Denk, T. Graning, W. Hering, A. Hoffmann, J. Hoffmann, H. Leiste, T. Mrotzek, R. Pippan, W. Schulmeyer, T. Weingartner, A. Zabernig, Tungsten (W) Laminate Pipes for Innovative High Temperature Energy Conversion Systems, Adv Eng Mater 17(4) (2015) 491-501.

[181] J.L. Walter, C.L. Briant, Tungsten wire for incandescent lamps, Journal of Materials Research 5(9) (2011) 2004-2022.

[182] D.T. H. Gietl, J. Riesch, S. Lebediev, T.Khvan, A. Dubinko, A. Bakaeva, Strength and deformation mechanism of tungsten wires exposed to high temperature

annealing: impact of potassium doping, (2016).

[183] P. Zhao, J. Riesch, T. Hoschen, J. Almanstotter, M. Balden, J.W. Coenen, R. Himml, W. Pantleon, U. von Toussaint, R. Neu, Microstructure, mechanical behaviour and fracture of pure tungsten wire after different heat treatments, Int J Refract Met H 68 (2017) 29-40.

[184] D. Terentyev, M. Rieth, G. Pintsuk, J. Riesch, A. von Müller, S. Antusch, K. Mergia, E. Gaganidze, H.C. Schneider, M. Wirtz, S. Nogami, J. Coenen, J.H. You, A. Zinovev, W. Van Renterghem, Recent progress in the assessment of irradiation effects for in-vessel fusion materials: tungsten and copper alloys, Nucl Fusion 62(2) (2022).

[185] M.A. Meyers, K.K. Chawla, Mechanical behavior of materials, 2nd ed., Cambridge University Press, Cambridge, UK ; New York, 2009.

[186] N. Li, Y. Zou, S. Zhang, X. Ma, X. Zhu, S. Li, T. Cao, Rock brittleness evaluation based on energy dissipation under triaxial compression, Journal of Petroleum Science and Engineering 183 (2019) 106349.

[187] L.M. Garrison, Y. Katoh, L.L. Snead, T.S. Byun, J. Reiser, M. Rieth, Irradiation effects in tungsten-copper laminate composite, J Nucl Mater 481 (2016) 134-146.

[188] I. Donald, Preparation, Properties and Applications of Glass and Glass-Ceramic Matrix Composites, Key Engineering Materials - KEY ENG MAT 108-110 (1995) 123-144.

[189] N.P. Bansal, A.R. Boccaccini, Ceramics and composites processing methods, Wiley,, Hoboken, N.J., 2012.

[190] T. Höschen, Zinovev, A., Chang, C. C., Terentyev, D. A., Gietl, H., Mao, Y., et al. , Results of the EUROfusion irradiation campaign for Wf/W material., Talk presented at 20th International Conference on Fusion Reactor Materials (ICFRM-20), 2021.

[191] E. Gaganidze, A. Chauhan, H.C. Schneider, D. Terentyev, G. Borghmans, J. Aktaa, Fracture-mechanical properties of neutron irradiated ITER specification tungsten, J Nucl Mater 547 (2021) 152761.

[192] D. Terentyev, C.-C. Chang, C. Yin, A. Zinovev, X.-F. He, Neutron irradiation effects on mechanical properties of ITER specification tungsten, Tungsten 3(4) (2021) 415-433.

[193] C. Yin, D. Terentyev, T. Zhang, R.H. Petrov, T. Pardoen, Impact of neutron irradiation on the strength and ductility of pure and ZrC reinforced tungsten grades, J Nucl Mater 537 (2020) 152226.

[194] T. Koyanagi, N.A.P.K. Kumar, T. Hwang, L.M. Garrison, X. Hu, L.L. Snead, Y. Katoh, Microstructural evolution of pure tungsten neutron irradiated with a mixed energy spectrum, J Nucl Mater 490 (2017) 66-74.

[195] A. Hasegawa, M. Fukuda, T. Tanno, S. Nogami, Neutron Irradiation Behavior of Tungsten, MATERIALS TRANSACTIONS 54(4) (2013) 466-471.

[196] H. Gietl, S. Olbrich, J. Riesch, G. Holzner, T. Höschen, J.W. Coenen, R. Neu, Estimation of the fracture toughness of tungsten fibre-reinforced tungsten composites, Engineering Fracture Mechanics 232 (2020).

[197] H. Gietl, J. Riesch, J.W. Coenen, T. Höschen, C. Linsmeier, R. Neu, Tensile deformation behavior of tungsten fibre-reinforced tungsten composite specimens in as-fabricated state, Fusion Engineering and Design 124 (2017) 396-400.

[198] J. Riesch, J.Y. Buffiere, T. Höschen, M. di Michiel, M. Scheel, C. Linsmeier, J.H. You, In situ synchrotron tomography estimation of toughening effect by semi-ductile fibre reinforcement in a tungsten-fibre-reinforced tungsten composite system, Acta Materialia 61(19) (2013) 7060-7071.

[199] F.L. S. X. Zhao, S. G. Qin, J. P. Song, G. -N. Luoa, PRELIMINARY RESULTS OF W FIBER REINFORCED W (Wf/W) COMPOSITES FABRICATED WITH

POWDER METALLURGY, (2013).

[200] J.W.C. Y. Mao, J. Riesch, S. Sistla, C. Chen, Y. Wu, L. Raumann,, C.L. R. Neu, and C. Broeckmann, Spark Plasma Sintering Produced W-Fiber-Reinforced Tungsten Composites, Springer Nature Switzerland AG (2019) 23.

[201] R.H.J. Hannink, TOUGHENING MECHANISMS FOR CERAMICS, in: H. Sakaki, H. Ohno, S. Kawai, H. Matsunami, M. Aono, H. Koinuma, B. Raveau, M.K. Wu, D.K. Finnemore, K. Togano, S. Sōmiya, M. Doyama, R. Roy (Eds.), Superconductors, Surfaces and Superlattices, Elsevier1994, pp. 925-941.

[202] R.H. Jones, C.H. Henager, Subcritical crack growth processes in SiC/SiC ceramic matrix composites, J Eur Ceram Soc 25(10) (2005) 1717-1722.

[203] H.-P. Baldus, M. Jansen, Novel High-Performance Ceramics—Amorphous Inorganic Networks from Molecular Precursors, Angewandte Chemie International Edition in English 36(4) (1997) 328-343.

[204] C. Gandhi, M.F. Ashby, Fracture-Mechanism Maps for Materials Which Cleave - Fcc, Bcc and Hcp Metals and Ceramics, Acta Metall Mater 27(10) (1979) 1565-1602.

[205] Y. Li, C. Xiang, X. Su, S. Li, H. Gu, J. Luo, X. Yin, Z. Yu, Grain growth and interfacial structures in SiC fibers, Ceram Int 46(8, Part A) (2020) 10279-10283.

[206] L. Longbiao, A hysteresis energy dissipation based model for multiple loading damage in continuous fiber-reinforced ceramic-matrix composites, Composites Part B: Engineering 162 (2019) 259-273.

[207] B. Mainzer, C.R. Lin, M. Friess, R. Riedel, J. Riesch, A. Feichtmayer, M. Fuhr, J. Almanstötter, D. Koch, Novel ceramic matrix composites with tungsten and molybdenum fiber reinforcement, J Eur Ceram Soc 41(5) (2021) 3030-3036.

[208] B. Jasper, S. Schoenen, J. Du, T. Hoeschen, F. Koch, C. Linsmeier, R. Neu, J. Riesch, A. Terra, J.W. Coenen, Behavior of tungsten fiber-reinforced tungsten based on single fiber push-out study, Nucl Mater Energy 9 (2016) 416-421.

[209] R.C. Wetherhold, J. Bös, Ductile reinforcements for enhancing fracture resistance in composite materials, Theoretical and Applied Fracture Mechanics 33(2) (2000) 83-91.

[210] R.D. Noebe, F.J. Ritzert, A. Misra, R. Gibala, Prospects for Ductility and Toughness Enhancement of NiAl by Ductile Phase Reinforcement, NASA Technical Memorandum 103796, NASA, Cleveland, Ohio; Ann Arbor, Michigan, 1991.

[211] Y. Mao, J.W. Coenen, J. Riesch, S. Sistla, J. Almanstotter, J. Reiser, A. Terra, C. Chen, Y. Wu, L. Raumann, T. Hoschen, H. Gietl, R. Neu, C. Linsmeier, C. Broeckmann, Fracture behavior of random distributed short tungsten fiber-reinforced tungsten composites, Nucl Fusion 59(8) (2019).

[212] D. Terentyev, W. Van Renterghem, L. Tanure, A. Dubinko, J. Riesch, S. Lebediev, T. Khvan, K. Verbeken, J.W. Coenen, E.E. Zhurkin, Correlation of microstructural and mechanical properties of K-doped tungsten fibers used as reinforcement of tungsten matrix for high temperature applications, International Journal of Refractory Metals and Hard Materials 79 (2019) 204-216.

[213] U.M. Ciucani, L. Haus, H. Gietl, J. Riesch, W. Pantleon, Microstructural evolution in single tungsten fiber-reinforced tungsten composites during annealing: recrystallization and abnormal grain growth, J Nucl Mater 543 (2021) 152579.

[214] D.A.H. Wartacz, J. Riesch, K. Pantleon, W. Pantleon, Recrystallization and grain growth in single tungsten fiber-reinforced tungsten composites, Journal of Physics: Conference Series 2635(1) (2023) 012034.

[215] Y. Mao, A. Duggal, A. Dittes, T. Lampke, J.W. Coenen, C. Linsmeier, Electrophoretic deposition prepared yttria as interface of tungsten fiber reinforced tungsten composites, Nucl Mater Energy 36 (2023).

[216] S. Palaniyappan, M. Trautmann, Y.R. Mao, J. Riesch, P. Gowda, N. Rudolph, J.W. Coenen, R. Neu, G. Wagner, Yttria-Coated Tungsten Fibers for Use in Tungsten Fiber-Reinforced Composites: A Comparative Study on PVD vs. CVD Routes, Coatings 11(9) (2021).

[217] J.W. Coenen, Y. Mao, S. Sistla, A.v. Müller, G. Pintsuk, M. Wirtz, J. Riesch, T. Hoeschen, A. Terra, J.H. You, H. Greuner, A. Kreter, C. Broeckmann, R. Neu, C. Linsmeier, Materials development for new high heat-flux component mock-ups for DEMO, Fusion Engineering and Design 146 (2019) 1431-1436.

[218] Y.M. Rui Shu, Jan W. Coenen, Alexis Terra, Chao Liu, Stephan Schönen, Johann Riesch, Christian Linsmeier, Christoph Broeckmann, Interface and mechanical properties of the single-layer long fiber reinforced Wf/W composites fabricated via field assisted sintering technology, Materials Science and Engineering: A 857 (2022).

[219] Y. Wang, H. Liu, H. Cheng, J. Wang, Interface engineering of fiber-reinforced all-oxide composites fabricated by the sol–gel method with fugitive pyrolytic carbon coatings, Composites Part B: Engineering 75 (2015) 86-94.

[220] K. Shimoda, J.S. Park, T. Hinoki, A. Kohyama, Influence of pyrolytic carbon interface thickness on microstructure and mechanical properties of SiC/SiC composites by NITE process, Compos Sci Technol 68(1) (2008) 98-105.

[221] G. Czél, M.R. Wisnom, Demonstration of pseudo-ductility in high performance glass/epoxy composites by hybridisation with thin-ply carbon prepreg, Compos Part a-Appl S 52 (2013) 23-30.

[222] M.E. Launey, R.O. Ritchie, On the Fracture Toughness of Advanced Materials, Adv Mater 21(20) (2009) 2103-2110.

[223] H. Ming-Yuan, J.W. Hutchinson, Crack deflection at an interface between dissimilar elastic materials, International Journal of Solids and Structures 25(9) (1989) 1053-1067.

[224] A.G. Evans, M.Y. He, J.W. Hutchinson, Interface Debonding and Fiber Cracking in Brittle Matrix Composites, J Am Ceram Soc 72(12) (1989) 2300-2303.

[225] S. Nogami, S. Watanabe, J. Reiser, M. Rieth, S. Sickinger, A. Hasegawa, Improvement of impact properties of tungsten by potassium doping, Fusion Engineering and Design 140 (2019) 48-61.

[226] B. Huang, Y. Xiao, B. He, J. Yang, J. Liao, Y. Yang, N. Liu, Y. Lian, X. Liu, J. Tang, Effect of potassium doping on the thermal shock behavior of tungsten, International Journal of Refractory Metals and Hard Materials 51 (2015) 19-24.

[227] J. Riesch, A. Feichtmayer, J.W. Coenen, B. Curzadd, H. Gietl, T. Hoschen, A. Manhard, T. Schwarz-Selinger, R. Neu, Irradiation effects in tungsten-From surface effects to bulk mechanical properties, Nucl Mater Energy 30 (2022).

[228] R. Lürbke, J. Riesch, A. Feichtmayer, B. Curzadd, T. Höschen, R. Neu, Experimental investigation of the impact of irradiation damages on the mechanical properties of tungsten, Nucl Mater Energy 42 (2025).

[229] V. Nikolic, J. Riesch, R. Pippan, The effect of heat treatments on pure and potassium doped drawn tungsten wires: Part I - Microstructural characterization, Mat Sci Eng a-Struct 737 (2018) 422-433.

[230] B. Jasper, J.W. Coenen, J. Riesch, T. Höschen, M. Bram, C. Linsmeier, Powder Metallurgical Tungsten Fiber-Reinforced Tungsten, Materials Science Forum 825-826 (2015) 125-133.

[231] L.P. Dorfman, D.L. Houck, M.J. Scheithauer, Consolidation of tungsten-coated copper composite powder, Journal of Materials Research 17(8) (2002) 2075-2084.

[232] J. Riesch, A. Feichtmayer, M. Fuhr, J. Almanstötter, J.W. Coenen, H. Gietl, T. Höschen, C. Linsmeier, R. Neu, Tensile behaviour of drawn tungsten wire used in tungsten fibre-reinforced tungsten composites, Phys Scripta T170 (2017).

[233] M. Treitz, Development of production routines for fibre reinforced metal matrix composites, University of Applied Sciences Munich, Munich, 2019.

[234] H. Gietl, A. von Müller, J.W. Coenen, M. Decius, D. Ewert, T. Höschen, P. Huber, M. Milwich, J. Riesch, R. Neu, Textile preforms for tungsten fibre-reinforced composites, J Compos Mater 52(28) (2018) 3875-3884.

[235] B.W. T. Gries. D. Veit, Textile Fertigungsverfahren - Eine Einführung, Carl - Hanser Verlag München, Aachen, 2019.

[236] E.N.a.W. Abrahart, Charles S., textile., Encyclopedia Britannica, Britannia, 2024.

[237] A.E. Markaki, T.W. Clyne, Mechanics of thin ultra-light stainless steel sandwich sheet material: Part I. Stiffness, Acta Materialia 51(5) (2003) 1341-1350.

[238] A. Mortensen, J.A. Cornie, M.C. Flemings, Solidification Processing of Metal-Matrix Composites, Jom-Us 40(2) (1988) 12-19.

[239] A. Seyam, A. El-Shiekh, Mechanics of Woven Fabrics:Part I: Theoretical Investigation of Weavability Limit of Yarns with Thickness Variation, Textile Research Journal 60(7) (1990) 389-404.

[240] W.M. Cranton, D.M. Spink, R. Stevens, C.B. Thomas, Growth and dielectric characterization of yttrium oxide thin films deposited on Si by r.f.-magnetron sputtering, Thin Solid Films 226(1) (1993) 156-160.

[241] Y. Mao, J. Engels, A. Houben, M. Rasinski, J. Steffens, A. Terra, C. Linsmeier, J.W. Coenen, The influence of annealing on yttrium oxide thin film deposited by reactive magnetron sputtering: Process and microstructure, Nucl Mater Energy 10 (2017) 1-8.

[242] S.-I. Park, Y.-J. Quan, S.-H. Kim, H. Kim, S. Kim, D.-M. Chun, C.S. Lee, M. Taya, W.-S. Chu, S.-H. Ahn, A review on fabrication processes for electrochromic devices, International Journal of Precision Engineering and Manufacturing-Green Technology 3(4) (2016) 397-421.

[243] H.T. Lee, S. Ando, J.W. Coenen, Y. Mao, J. Riesch, H. Gietl, R. Kasada, Y. Hamaji, K. Ibano, Y. Ueda, Longitudinal and shear wave velocities in pure tungsten and tungsten fiber-reinforced tungsten composites, Phys Scripta T170 (2017).

[244] A. Bendjerad, S. Boukhtache, A. Benhaya, D. Luneau, S.E.h. Abaidia, K. Benyahia, Modeling of magnetic properties of iron thin films deposited by RF magnetron sputtering using Preisach model, Serbian Journal of Electrical Engineering 13 (2016) 229-238.

[245] X. Ma, Z. Huang, L. Feng, Effects of the Deposition Mode and Heat Treatment on the Microstructure and Wettability of Y2O3 Coatings Prepared by Reactive Magnetron Sputtering, Coatings, 2022.

[246] J. Zhu, Y. Zhu, W. Shen, Y. Wang, J. Han, G. Tian, P. Lei, B. Dai, Growth and characterization of yttrium oxide films by reactive magnetron sputtering, Thin Solid Films 519(15) (2011) 4894-4898.

[247] P.H. Li, Y. Zhang, X.H. Qu, Effect of Y2O3 Coating on the Interface and Mechanical Properties of SiC Fiber Reinforced GH4738 Composites, Materials Science Forum 898 (2017) 604-608.

[248] H.J. Quah, K.Y. Cheong, Effects of post-deposition annealing ambient on Y2O3 gate deposited on silicon by RF magnetron sputtering, J Alloy Compd 529 (2012) 73-83.

[249] M. Podob, Chemical Vapor Deposition (CVD) Coatings for Protection of Jet Engine Components, ASME 1993 International Gas Turbine and Aeroengine Congress and Exposition, 1993.

[250] M.A. Ehsan, S.S. Shah, S.I. Basha, A.S. Hakeem, M.A. Aziz, Recent Advances in Processing and Applications of Heterobimetallic Oxide Thin Films by Aerosol-Assisted Chemical Vapor Deposition, The Chemical Record 22(7) (2022) e202100278.

[251] J.R. Creighton, J.E. Parmeter, Metal CVD for microelectronic applications: An examination of surface chemistry and kinetics, Critical Reviews in Solid State and Materials Sciences 18(2) (1993) 175-237.

[252] M.J. Hampden-Smith, T.T. Kodas, Chemical vapor deposition of metals: Part 1. An overview of CVD processes, Chemical Vapor Deposition 1(1) (1995) 8-23.

[253] M.J. Hampden-Smith, T.T. Kodas, Chemical vapor deposition of metals: Part 2. Overview of selective CVD of Metals, Chemical Vapor Deposition 1(2) (1995) 39-48.

[254] C.R. Kleijn, R. Dorsman, K.J. Kuijlaars, M. Okkerse, H. van Santen, Multi-scale modeling of chemical vapor deposition processes for thin film technology, Journal of Crystal Growth 303(1) (2007) 362-380.

[255] T.T. Kodas, M.J. Hampden-Smith, The Chemistry of Metal CVD, Wiley-VCH, 1st Edition, 2008.

[256] X.-N. Ren, H. Zhou, C.-C. Ge, X.-Q. Liu, Y. Li, W.-P. Zhou, W.-L. Liu, Z.-j. Zhou, X.-G. Zhang, M. Xia, Proposal and research on using tungsten carbonyl-CVD process for making W-coating PFMs and W-tubes, J Nucl Mater 455(1) (2014) 582-585.

[257] D.A. Bell, C.M. McConica, K.L. Baker, E. Kuchta, Batch Reactor Kinetic Studies of Tungsten LPCVD from Silane and Tungsten Hexafluoride, Journal of The Electrochemical Society 143(1) (1996) 296.

[258] S.G. Rosenberg, M. Barclay, D.H. Fairbrother, Electron induced reactions of surface adsorbed tungsten hexacarbonyl (W(CO)6), Physical Chemistry Chemical Physics 15(11) (2013) 4002-4015.

[259] T. Ohba, Y. Furumura, Chemical Vapour Deposition of Tungsten by the Reduction of WF6 using Si, SiH4, Si2H6, Si3H8, B2H6, PH3, and H2, IETE Journal of Research 37(2) (1991) 212-219.

[260] L. Sun, G. Yuan, L. Gao, J. Yang, M. Chhowalla, M.H. Gharahcheshmeh, K.K. Gleason, Y.S. Choi, B.H. Hong, Z. Liu, Chemical vapour deposition, Nature Reviews Methods Primers 1(1) (2021) 5.

[261] Y. Mori, K. Yoshii, H. Kakiuchi, K. Yasutake, Atmospheric pressure plasma chemical vapor deposition system for high-rate deposition of functional materials, Review of Scientific Instruments 71(8) (2000) 3173-3177.

[262] Y. Xie, C. Tan, X. Yu, Z. Nie, Z. Liu, Cell and dendrite growth of tungsten by atmospheric pressure chemical vapor deposition, J Alloy Compd 922 (2022) 166161.

[263] H. Zhang, X. Yu, Z. Nie, C. Tan, F. Wang, H. Cai, Y. Li, F. Wang, H. Cai, Microstructure and growth mechanism of tungsten carbide coatings by atmospheric CVD, Surface and Coatings Technology 344 (2018) 85-92.

[264] K.J. Kuijlaars, C.R. Kleijn, H.E.A. van den Akker, Modeling of selective tungsten low-pressure chemical vapor deposition, Thin Solid Films 290-291 (1996) 406-410.

[265] A. Iatsenko, Development of improved technology for producing graphene-like coating by LPCVD method, Technology audit and production reserves 4(3(72)) (2023) 6-9.

[266] Y. Li, W. Liang, Y. Shi, W. Zhou, LPCVD-based SiO2/SiC multi-layers coating on graphite for improved anti-oxidation at wide-ranged temperatures, Composites Part B: Engineering 146 (2018) 155-164.

[267] G. Franz, Plasma Enhanced Chemical Vapor Deposition of Organic Polymers, Processes 9(6) (2021) 980.

[268] P. Horňák, D. Kottfer, K. Kyzioł, M. Trebuňová, J. Majerníková, Ł. Kaczmarek, J. Trebuňa, J. Hašuť, M. Paľo, Microstructure and Mechanical Properties of Annealed WC/C PECVD Coatings Deposited Using Hexacarbonyl of W with Different Gases, Materials 13(16) (2020) 3576.

[269] C.-H. Lu, D. Hao, N.-C. Yeh, A perspective of recent advances in PECVD-grown graphene thin films for scientific research and technological applications, Materials Chemistry and Physics 319 (2024) 129318.

[270] V.A.C. Haanappel, H.D. van Corbach, T. Fransen, P.J. Gellings, The Preparation of Thin Alumina Films by Metal-Organic Chemical Vapour Deposition: A Short Review, High Temperature Materials and Processes 13(2) (1994) 149-158.

[271] J.E. Kelsey, C. Goldberg, G. Nuesca, G. Peterson, A.E. Kaloyeros, B. Arkles, Low temperature metal-organic chemical vapor deposition of tungsten nitride as diffusion barrier for copper metallization, Journal of Vacuum Science & Technology B: Microelectronics and Nanometer Structures Processing, Measurement, and Phenomena 17(3) (1999) 1101-1104.

[272] N.C. Ou, X. Su, D.C. Bock, L. McElwee-White, Precursors for chemical vapor deposition of tungsten oxide and molybdenum oxide, Coordination Chemistry Reviews 421 (2020) 213459.

[273] C.A. Wilson, J.A. McCormick, A.S. Cavanagh, D.N. Goldstein, A.W. Weimer, S.M. George, Tungsten atomic layer deposition on polymers, Thin Solid Films 516(18) (2008) 6175-6185.

[274] D.K. Nandi, U.K. Sen, S. Sinha, A. Dhara, S. Mitra, S.K. Sarkar, Atomic layer deposited tungsten nitride thin films as a new lithium-ion battery anode, Physical Chemistry Chemical Physics 17(26) (2015) 17445-17453.

[275] J.S. Becker, R.G. Gordon, Diffusion barrier properties of tungsten nitride films grown by atomic layer deposition from bis(tert-butylimido)bis(dimethylamido)tungsten and ammonia, Applied Physics Letters 82(14) (2003) 2239-2241.

[276] Z. Weng, R. Wallis, B. Wingfield, P. Evans, P. Baginski, J. Kainth, A.E. Nikolaenko, L.Y. Lee, J. Baginska, W.P. Gillin, I. Guiney, C.J. Humphreys, O. Fenwick, Memristors with Monolayer Graphene Electrodes Grown Directly on Sapphire Wafers, ACS Applied Electronic Materials 6(10) (2024) 7276-7285.

[277] J.E. Crowell, Chemical methods of thin film deposition: Chemical vapor deposition, atomic layer deposition, and related technologies, Journal of Vacuum Science & Technology A 21(5) (2003) S88-S95.

[278] F.X. Li, B.M. Armstrong, H.S. Gamble, LPCVD of tungsten by selective deposition on silicon, Journal of Materials Science: Materials in Electronics 12(4) (2001) 303-306.

[279] K.J. Kuijlaars, C.R. Kleijn, H.E.A. van Den Akker, A detailed model for low-pressure CVD of tungsten, Thin Solid Films 270(1) (1995) 456-461.

[280] A. Katz, A. Feingold, A. El-Roy, S.J. Pearton, E. Lane, S. Nakahara, M. Geva, Tungsten metallization onto InP prepared by rapid thermal low-pressure chemical vapor deposition of WF6 and H2, Applied Physics Letters 61(13) (1992) 1522-1524.

[281] G. Auvert, Y. Pauleau, D. Tonneau, Kinetics of Laser-Assisted Chemical Vapor Deposition of Tungsten Microstructures, Japanese Journal of Applied Physics 31(1R) (1992) 100.

[282] C. Lu, L. Cheng, C. Zhao, L. Zhang, Y. Xu, Kinetics of chemical vapor deposition of SiC from methyltrichlorosilane and hydrogen, Applied Surface Science 255(17) (2009) 7495-7499.

[283] F. Wang, N. Zhu, T. Li, H.-C. Zhang, Material and Energy Efficiency Analysis of Low Pressure Chemical Vapor Deposition of TiO2 Film, Procedia CIRP 15 (2014) 32-37.

[284] L. Raumann, J.W. Coenen, J. Riesch, Y. Mao, H. Gietl, T. Hoschen, C. Linsmeier, O. Guillon, Modeling and validation of chemical vapor deposition of tungsten for tungsten fiber reinforced tungsten composites, Surf Coat Tech 381 (2020).

[285] L. Raumann, J.W. Coenen, J. Riesch, Y. Mao, D. Schwalenberg, T. Wegener, H. Gietl, T. Höschen, C. Linsmeier, O. Guillon, Modeling and experimental validation of a Wf/W-fabrication by chemical vapor deposition and infiltration, Nucl Mater Energy 28 (2021) 101048.

[286] C.M. McConica, K. Krishnamani, The Kinetics of LPCVD Tungsten Deposition in a Single Wafer Reactor, Journal of The Electrochemical Society 133(12) (1986) 2542.

[287] Y. Lakhotkin, V., Chemical mechanisms of tungsten CVD, J. Phys. IV France 09(PR8) (1999) Pr8-245-Pr8-250.

[288] E.K. Broadbent, C.L. Ramiller, Selective Low Pressure Chemical Vapor Deposition of Tungsten, Journal of The Electrochemical Society 131(6) (1984) 1427.

[289] A.A. Zinn, Chemical Vapor Deposition of Tungsten, The Chemistry of Metal CVD1994, pp. 105-174.

[290] H. Körner, Selective low pressure chemical vapour deposition of tungsten: Deposition kinetics, selectivity and film properties, Thin Solid Films 175 (1989) 55-60.

[291] W.A. Bryant, Kinetics of Tungsten Deposition by the Reaction of WF6 and Hydrogen, Journal of The Electrochemical Society 125(9) (1978) 1534.

[292] W.A. Bryant, G.H. Meier, Kinetics of the Chemical Vapor Deposition of Tungsten, Journal of The Electrochemical Society 120(4) (1973) 559.

[293] E.J. McInerney, E. Srinivasan, D.C. Smith, G. Ramanath, Kinetic Rate Expression for längsten Chemical Vapor Deposition in Different WF6 Flow Regimes from Step Coverage Measurements, 91(7) (2000) 573-580.

[294] H. Gietl, Weiterentwicklung von wolframfaserverstärktem

Wolframverbundwerkstoff für den Einsatz in der Fusion, 2018, p. 163.

[295] A.S. Altinok, R.T. Ogulata, Production in Twisting Machine and Examining Physical and Thermal Properties of Tungsten Wire Reinforced Composite Yarn, Tekst Konfeksiyon 26(2) (2016) 141-146.

[296] J.W. Coenen, M. Treitz, H. Gietl, P. Huber, T. Hoeschen, L. Raumann, D. Schwalenberg, Y. Mao, J. Riesch, A. Terra, C. Broeckmann, O. Guillon, C. Linsmeier, R. Neu, The use of tungsten yarns in the production for W-f/W, Phys Scripta T171(1) (2020).

[297] H.O. Pierson, Handbook of chemical vapor deposition (CVD) principles, technology, and applications, (1999).

[298] Y. Mao, C. Chen, J.W. Coenen, J. Riesch, S. Sistla, J. Almanstötter, A. Terra, Y. Wu, L. Raumann, T. Höschen, H. Gietl, R. Neu, C. Linsmeier, C. Broeckmann, On the nature of carbon embrittlement of tungsten fibers during powder metallurgical processes, Fusion Engineering and Design 145 (2019) 18-22.

[299] H.Z. Zhang, P.Z. Feng, F. Akhtar, Aluminium matrix tungsten aluminide and tungsten reinforced composites by solid-state diffusion mechanism, Sci Rep-Uk 7 (2017).

[300] J. Gonzalez-Julian, Processing of MAX phases: From synthesis to applications, J Am Ceram Soc 104(2) (2021) 659-690.

[301] J. Gonzalez-Julian, S. Onrubia, M. Bram, O. Guillon, Effect of sintering method on the microstructure of pure Cr2AlC MAX phase ceramics, Journal of the Ceramic Society of Japan 124 (2016) 415-420.

[302] H. Gietl, J. Riesch, J.W. Coenen, T. Höschen, R. Neu, Production of tungsten-fibre reinforced tungsten composites by a novel continuous chemical vapour deposition process, Fusion Engineering and Design 146 (2019) 1426-1430.

[303] M.K. Sharma, I.M. Rao, J. Bijwe, Influence of orientation of long fibers in carbon fiber-polyetherimide composites on mechanical and tribological properties, Wear 267 (2009) 839-845.

[304] Y. Tomita, T. Tamaki, K. Morioka, Effect of Fiber Strength on Notch Bending Fracture of Unidirectional Long Carbon Fiber–Reinforced Epoxy Composites, Mater Charact 41(4) (1998) 123-135.

[305] L. Zhu, S. Cao, X. Zhang, W. Shen, C. Zhu, Comparison of the Bending Resistance Properties of Carbon Fiber/Foam Sandwich Structural Composites with Different Laying Angles, Fibres Text East Eur 30 (2022) 75 - 81.

[306] T.M. Besmann, W.M. Matlin, D.P. Stinton, Chemical Vapor Infiltration Process Modeling and Optimization, MRS Online Proceedings Library 410(1) (1995) 441-451.

[307] J. Du, A feasibility study of tungsten-fiber-reinforced tungsten composites with engineered interfaces, (2011).

[308] D. Ni, Y. Cheng, J. Zhang, J.-X. Liu, J. Zou, B. Chen, H. Wu, H. Li, S. Dong, J. Han, X. Zhang, Q. Fu, G.-J. Zhang, Advances in ultra-high temperature ceramics, composites, and coatings, Journal of Advanced Ceramics 11(1) (2022) 1-56.

[309] R. Naslain, Two-dimensional SiC/SiC composites processed according to the isobaric-isothermal chemical vapor infiltration gas phase route, J Alloy Compd 188 (1992) 42-48.

[310] S. Schönen, B. Jasper, J.W. Coenen, J. Du, T. Höschen, J. Riesch, G. Natour, R. Neu, C. Linsmeier, Insight into single-fiber push-out test of tungsten fiber-reinforced tungsten, Composite Interfaces 26(2) (2019) 107-126.

[311] J. Riesch, T. Höschen, C. Linsmeier, S. Wurster, J.H. You, Enhanced toughness and stable crack propagation in a novel tungsten fibre-reinforced tungsten composite produced by chemical vapour infiltration, Phys Scripta T159 (2014).

[312] J. Riesch, T. Höschen, A. Galatanu, J. You, Tungsten-fibre reinforced tungsten composites: A novel concept for improving the toughness of tungsten, Proceedings of the eighteenth international conference on composite materials, Jeju, South Korea, 2011.

[313] J. Riesch, Entwicklung und Charakterisierung eines wolframfaserverstärkten Wolfram-Verbundwerkstoffs, Technische Universität München, 2012, p. 180.

[314] C.Z. Leng, M. Losego, Vapor phase infiltration (VPI) for transforming polymers into organic–inorganic hybrid materials: a critical review of current progress and future challenges, Materials Horizons 4 (2017) 747-771.

[315] C. Camilloni, F. Pietrucci, Advanced simulation techniques for the thermodynamic and kinetic characterization of biological systems, Advances in Physics: X 3 (2018).

[316] M.F. Reyniers, G.B. Marin, Experimental and theoretical methods in kinetic studies of heterogeneously catalyzed reactions, Annual review of chemical and biomolecular engineering 5 (2014) 563-94.

[317] G.L. Vignoles, 17 - Modeling of chemical vapor infiltration processes, in: P. Boisse (Ed.), Advances in Composites Manufacturing and Process Design, Woodhead Publishing2015, pp. 415-458.

[318] A. Moussa, M. Boulekra, B. Abdeldjalil, N. Sassane, A. Grid, Elaboration of Thermostructural Composites by Chemical Vapor Infiltration (CVI), 3 (2015) 38-42.

[319] Z. Ramadan, Y. Choi, J. Lee, D. Im, I.-T. Im, Three-Dimensional Heat Transfer Analysis of a TG-CVI Reactor, MATEC Web of Conferences 30 (2015) 03008.

[320] J. Chen, X. Xiong, Distribution of Deposited Carbon in Carbon Brake Disc Made by Pressure-Gradient Chemical Vapor Infiltration, Carbon letters 8(1) (2007) 25-29.

[321] H.J. Jeong, H.D. Park, J.D. Lee, J.O. Park, Densification of carbon/carbon composites by pulse chemical vapor infiltration, Carbon 34(3) (1996) 417-421.

[322] G.L. Vignoles, C. Descamps, C. Charles, C. Klein, How is it possible to get optimal infiltration fronts during chemical vapor infiltration with thermal gradients ?, Open Ceramics 15 (2023) 100375.

[323] K.K. Chawla, Composite Materials: Science and Engineering, Springer New York, NY1998.

[324] A.v. Müller, D. Dorow-Gerspach, M. Balden, M. Binder, B. Buschmann, B. Curzadd, T. Loewenhoff, R. Neu, G. Schlick, J.H. You, Progress in additive manufacturing of pure tungsten for plasma-facing component applications, J Nucl Mater 566 (2022) 153760.

[325] R. Neu, J.W. Coenen, B. Curzadd, H. Gietl, H. Greuner, T. Höschen, K. Hunger, R. Lürbke, A. Müller, J. Riesch, G. Schlick, U. Siefken, E. Visca, J. You, Material and component developments for the DEMO divertor using fibre reinforcement and additive manufacturing, Materials Research Express 11(1) (2023).

# Acknowledgments

The history of nuclear fusion is marked by pioneers who dedicated their careers to a technology they might never see come to fruition. Their unwavering commitment was driven by the conviction that they were pursuing a greater good. These visionaries deserve our utmost respect and gratitude for their tireless efforts, whether as scientists or as those who provided the necessary infrastructure. I am extremely grateful to have had the opportunity to pursue my ideas in such a forward-looking field.

Therefore, I would first like to express my deepest gratitude to my doctoral supervisors, **Prof. Jesus Gonzalez-Julian** and **Prof. Christian Linsmeier**, as well as my daily supervisor, **Dr. Jan Willem Coenen**, whose guidance and support made it possible for me to work in this innovative field. Their consistent feedback, encouragement, and exemplary mentorship were invaluable throughout this journey. I also extend my heartfelt thanks **to Dr. Yiran Mao** from IFN-1 and **Dr. Johann Riesch** from the Institute of Plasma Physics in Garching, whose expertise and support were instrumental in my progress. I consider them my unofficial fourth and fifth supervisors, without whom this work would not have been possible.

I am also profoundly grateful to the following individuals for their support and guidance:

- **Stephan Schönen** for his extensive support with all modelling projects. An absolute professional who knows his trade and without whom I would not have been able to complete the project on time.

- **Dr. Alexander Knieps** for numerous discussions and extensive support with programming challenges, especially my monitoring project. His excellent coffee also kept me energized throughout. It is a privilege to count him among my circle of friends as one of the smartest people I have ever met.

- **Alexis Terra** for his support in constructing the first CVI setup and conducting the first copper infiltration tests. An all-rounder who can do almost everything.

- **Dirk Nicolai** for his expertise and support with any laboratory challenges. As one of the few colleagues who set up the plant, he is an irreplaceable member of IFN-1. He supported me in countless tasks such as reprogramming the PID controller for the preheater and new cooling system and simultaneously took on organizational tasks such as ordering and maintaining system documentation.

- **Roland Bär** for his detailed knowledge of all our machines, whose expertise, advice and assistance in modifying the WILMA were crucial in achieving the results presented in this thesis. I cannot thank him enough.

- **Till Höschen** from the Institute of Plasma Physics in Garching. A man who even takes time out of his vacation to test my samples with me.

- **Dr. Philipp Huber**, **Erika Barcan** and **Violetta Adiuszyn** from the Institute of Textile Technology in Aachen for producing our essential base-textiles.

- Our mechanical workshop, especially to **Tim Rüttgers**, **Noah Richter** and **Rene Dohmen**, for their support with countless inquiries regarding various individual parts for the system. I was able to learn a lot from them. I also extend my gratitude to **all apprentices** who helped me to e.g. install a new circulation pump.

- **Thomas Krings** and **Kalle von Bovert** for their constant assistance with recurring turbopump jams, ordering and installing the new pump connection, relocating the suction system, and always being available to help me out with spare parts. This also includes Guruparan Satheeswaran. You guys are amazing.

- **Norbert Sandri** for installing the new monitoring system of the power input with breathtaking speed. I wish him all the best for his well-deserved retirement. His kind of knowledge and experience will certainly be needed again one day.

**Franz Josef Kemp** and **Michael Lowis** for checking my electrical components, helping with the new turbopump bypass valve connections, and organizing my gas cylinder systems. Thank you also for teaching me how to add hazardous materials to our system.

- **Beatrix Göths** for her support in the metallography lab and help with several challenges at the EDX or SEM. In this context, I would also like to thank **Dr. Marcin Rasinski**, who was also always helpful to me.

- **Daniel Hintzen** from ZEA-1 for his outstanding support and patience during the development of the final CVI setup, which we optimized together over countless versions.

- **Dr. Philipp Drews**, for sharing my interest in this topic from day one and accompanying me through hours of discussions that helped me to better understand my topic.

- **Fabienne Weitz, Ulf Knoche** and **Michael Vogel** for their help with various practical challenges such as changing the WF6 bottles or preparing samples.

- **Stefan Kirtz** and **Thomas Gürth** for their help with all IT-related issues.

- **Martina Mangels** and **Ruth Hanke** for handling several organizational matters in connection with orders, purchase orders, organization of lab keys and much more.

- **Angelika Hallmanns** and **Judith Schönbrenner,** who both took care of many bureaucratic challenges.

- **Sarah Kuhn-Stassar** and **Alexandra de Schepper** for reshaping the institutes structure.

- To my predecessors **Dr. Hanns Gietl, Dr. Leonard Raumann**, **Michael Treitz,** and **Daniel Schwalenberg**, whose invaluable contributions laid the foundation for this work.

- My **fellow doctoral researchers** at IFN-1, who created a supportive and pleasant working environment. Special thanks goes to Christoph Kawan, a professional photographer and friend, who assisted me with various images and supported me in many other ways.

Finally, I would like to thank my **friends,** my partner **Laura Krasniqi** and my **family**, especially my brother **Benjamin Lau** and my parents **Anke Lau** and **Andreas Lau**. Without their unwavering support, I would not have been able to pursue this project.

I thank you all from the bottom of my heart for your tireless encouragement over all the years.

# Appendix Reference

For supplementary materials and additional data, please refer to the digital appendix available at the following link:

https://fz-juelich.sciebo.de/s/k6VrEDLO7xuv7RX.

If the link is unavailable, please contact the corresponding author of this work at AlexLau1604@gmail.com or A.Lau@fz-juelich.de for assistance. As an alternative option, please contact Dr. Jan Willem Coenen via email at j.w.coenen@fz-juelich.de.

Band / Volume 663
**Advances in Understanding Nitrate Aerosol Formation and the Implications for Atmospheric Radiative Balance**
A. Milousis (2025), 195 pp
ISBN: 978-3-95806-823-0

Band / Volume 664
**Optimization of NaSICON-type lithium-ion conductors for solid-state batteries**
A. Loutati (2025), viii, 104 pp
ISBN: 978-3-95806-824-7

Band / Volume 665
**Innovative Plasma Sprayed Thermal Barrier Coatings for Enhanced Flexibility in Gas Turbine Operation**
J. Igel (2025), V, 153, XXXVI pp
ISBN: 978-3-95806-827-8

Band / Volume 666
**Techno- ökonomisches Potenzial dezentraler und autarker Energiesysteme**
S. K. A. Risch (2025), xxiii, 210 pp
ISBN: 978-3-95806-829-2

Band / Volume 667
**Reactive Field Assisted Sintering of Novel Rare Earth Garnets for Plasma Etching Applications**
C. Stern (2025), VII, 101, XXVIII pp
ISBN: 978-3-95806-833-9

Band / Volume 668
**Effects of mucilage and extracellular polymeric substances on soil gas diffusion**
A. Haupenthal (2025), v, 99 pp
ISBN: 978-3-95806-834-6

Band / Volume 669
**Quantifying Recombination Losses and Charge Extraction in Halide Perovskite Solar Cells**
L. Krückemeier (2025), vi, 286 pp
ISBN: 978-3-95806-835-3

Band / Volume 670
**Investigation of Dynamic Material Changes During the Preparation of ZnPd Nanoparticles Supported on ZnO and their Catalytic Application in Methanol Steam Reforming on the Atomic Level**
A. Meise (2025), xviii, 175 pp
ISBN: 978-3-95806-838-4

Band / Volume 671
**Improving Energy Efficiency of Public Buildings by Influencing Occupant Behaviour using Dashboards and Gamification**
E. Ubachukwu (2025), xxi, 191 pp
ISBN: 978-3-95806-840-7

Band / Volume 672
**Exploring Plant Responses to Changing Environments: Integrating Phenotyping and Modeling Across Scales**
F. M. Bauer (2025), xxix, 188 pp
ISBN: 978-3-95806-845-2

Band / Volume 673
**A constitutive theory to represent non-idealities in contacting of SOC interconnect contacts**
R. M. Pinto (2025), xii, 139 pp
ISBN: 978-3-95806-846-9

Band / Volume 674
**Strontium titanate based materials for use as oxygen transport membranes in membrane reactors**
Y. Tang (2025), XIV, 132 pp
ISBN: 978-3-95806-849-0

Band / Volume 675
**Scaling Methods for the Production of Tungsten Fiber-Reinforced Composites via Chemical Vapor Deposition**
A. Lau (2025), untersch. Pag.
ISBN: 978-3-95806-851-3

Energie & Umwelt / Energy & Environment
Band / Volume 675
ISBN 978-3-95806-851-3

Mitglied der Helmholtz-Gemeinschaft

JÜLICH
Forschungszentrum